Growth mechanics of a bacterial microcolony

Marie-Cécilia Duvernoy

UNIVERSITÉ DE GRENOBLE

THÈSE

Pour obtenir le grade de

DOCTEUR DE L'UNIVERSITÉ DE GRENOBLE

Spécialité : **Physique pour les sciences du vivant**

Arrêté ministériel : 7 Août 2006

Présentée par

Marie-Cécilia Duvernoy

Thèse dirigée par **Catherine Quilliet**
et codirigée par **Nicolas Desprat et Sigolène Lecuyer**

préparée au sein **du Laboratoire Interdisciplinaire de Physique (UJF), du Laboratoire de Physique Statistique (ENS)**
et de **Ecole Doctorale de Physique**

Mécanique de croissance d'une micro-colonnie bactérienne

Growth mechanics of a bacterial microcolony

Thèse soutenue publiquement le **4 Novembre 2015**,
devant le jury composé de :

Hans Geiselmann
Professeur, Université Joseph Fourier, Président
Nelly Henry
Directrice de recherche, CNRS, Rapporteur
Axel Buguin
Professeur, Université Pierre et Marie Curie, Examinateur
Zemer Gitai
Professor, Princeton University, Examinateur
Jean-Paul Rieu
Professeur, Université Claude Bernard, Examinateur
Nicolas Desprat
Maître de conférence, Université Paris Diderot, Co-Directeur de thèse
Sigolène Lecuyer
Chargée de recherche, CNRS, Co-Directeur de thèse
Catherine Quilliet
Maître de conférence, Université Joseph Fourier, Directeur de thèse
Gurol Suel (Rapporteur extérieur au jury)
Assistant professor, University of California San Diego, Rapporteur

À mon grand-père, Jean Duvernoy,
docteur de l'Université de Grenoble,

Acknowledgements

Tout d'abord, je souhaite remercier mes encadrants pour leur confiance, leur considération, leur soutien et leur temps qu'ils n'ont pas compté pendant ces 3 années. Ces remerciements sur papier feront immanquablement pâle figure face à la reconnaissance qui m'anime réellement. Devant un énième problème technique, je choisis cette fois-ci de me limiter en longueur, mais sachez que j'aurais pu m'épancher sur plusieurs paragraphes. Merci Nicolas pour ton engagement (du sens sportif au sens presque militant), pour ta franchise et pour ta passion contagieuse de l'exploration expérimentale et du "geste de l'artisan". Merci Sigolène pour ta bonne humeur, ta sagesse et ton bon sens aussi bien scientifique qu'humain. Merci Catherine pour ton regard critique de physicienne et pour l'ambiance joyeuse que tu sais instaurer dans un univers de travail. Vous m'avez permis de trouver un équilibre pour mener ce projet et j'ai bien conscience que je vous dois énormément. Je pense même que vous allez me manquer par la suite ! Merci à Martial de m'avoir épaulé pour les mesures de force avec optimisme et exigence. Dans cette tache, merci aussi à Irène et Richard pour leur disponibilité et leur aide. Merci à Delphine de m'avoir permis de faire des expériences de RICM. Et merci à Thierry Mora de nous avoir construit des simulations dernièrement. Merci enfin à nos collaborateurs biologistes de l'Institut Pasteur, Christophe Beloin et Jean-Marc Ghigo ; les discussions entre nos communautés ne sont pas toujours simples, merci d'avoir pris le temps nécessaire à ce que nos interactions soient bénéfiques. Enfin, merci aux membres du jury et aux rapporteurs pour le temps que vous avez consacré à évaluer mon travail.

Au cours de cette thèse j'ai partagé mon temps entre deux laboratoires, mes remerciements sont donc, eux-aussi, en deux temps.

Coté LPS, merci à toute l'équipe du ABCD lab, ainsi qu'aux membres de PicoSeq. J'ai adoré l'ambiance de ce labo. Quelques mercis tout particuliers : merci à Vincent de m'avoir donné une perspective sur le monde de la recherche, et même parfois sur le monde en général, toujours avec une grande simplicité ; merci à Bertrand pour ses conseils de biologiste, distillés avec bonne humeur, qui ont souvent été salvateurs et merci à David pour ses discussions florissantes d'idées grâce auxquelles il partage facilement sa vaste culture scientifique. Merci aussi aux plus jeunes qui sont arrivés au fur et à mesure et ont contribué à la bonne ambiance du groupe, en particulier François-Xavier, Tal, Maxime, Saurabh, Fatima et Samar. Merci à Jean-François pour ses conseils autant physiques que gastronomiques, à Gordon pour les barres chocolatées dans le tiroir et les discussions du goûter et merci à Claire pour les pauses remotivantes. Enfin, merci à ces gens dont beaucoup de choses dépendent : Annie qui fait pâlir les clichés sur l'administration française, Marie, Nora, Zaire, Benoît et les membres de l'atelier de mécanique. Pour finir, et bien qu'il ne soit pas du LPS, c'est ici que je remercierai Simon pour nos repas du midi au Petit Chinois qui ont été une occasion de plus d'échanger sur nos vies de thésards.

Coté LIPhy, merci à tous les doctorants et tout particulièrement à mes co-bureaux, Vassanti et Matthieu, et anciennement Vincent et Xavier, pour toutes ces discussions et ces rigolades. Mercis particuliers aussi à Ianis, Yara, Flore, Richard et Joe dont l'anglais a été mis à contribution pour des relectures de dernière minute. Merci aussi à la grande équipe DyFCoM, et en particulier Delphine, Lionel, Salima, ainsi qu'à Olivier Rivoire qui a été mon tuteur. Merci enfin à Jessie, Chantal et Nadine pour le volet administratif.

Sur le plan matériel, un bon nombre d'amis, de Paris et de Grenoble, m'ont facilité la vie en m'hébergeant dans l'une ou l'autre de ces deux villes. Par ordre chronologique, merci pour votre accueil à Lucas et aux Giérois, merci à Yacine, merci à Geneviève de m'avoir hébergée à Grenoble puis à Paris avec Clément, merci aux colocs de Bourg-La-Reine, merci à Sophie, merci à Clément et ses colocs, merci à Robin et Julien, merci à Mélanie et V-swag, merci à François-Xavier sur ce tableau-là aussi. Merci enfin à Anna qui m'a accueillie à Londres pour que j'aille donner un séminaire à Cambridge. Au-delà de ces considérations matérielles, je vous remercie pour les bons moments passés au cours de ces trois années que vous soyez dans cette liste ou non.

Enfin, merci à Yoann, mon coéquipier dans la vie, qui m'a aussi bien aidé sur le plan du logement en supportant une copine à moitié absente pendant 3 ans ; merci aussi de m'avoir écouté raconter les hauts et les bas de cette thèse au jour le jour et merci pour ton soutien pendant la rédaction malgré les circonstances. Merci aussi à Cécile et Jeanine pour leur aide pendant les transitions entre Grenoble et Paris. Pour finir, je remercie ma famille qui m'a amenée jusqu'à cette thèse à force de soutien et d'amour du savoir. Je dédie ce manuscrit à mon grand-père, docteur de l'Université de Grenoble : j'aurais aimé que tu puisses mettre ce manuscrit dans ta bibliothèque et te sentir fier le jour de ma soutenance. Merci aussi à ma grand-mère, à ma maman pour son soutien inconditionnel, à mon papa qui a éveillé ma curiosité scientifique dès le plus jeune âge et à sa compagne, Marie-Isabelle, qui m'a initiée à diverses activités pratiques.

Abstract

In this work, we propose a framework to understand the morphogenesis of two-dimensional microcolonies. In particular, we have explored how growth and adhesion of individual cells compete during microcolony extension. We have shown (i) that isolated cells display an asymmetry in their adhesion, which is higher at the old pole, (ii) that bacterial elongation can result in pushing forces inside the colony. Since the combination of these two effects is expected to produce mechanical stress at the scale of the microcolony, we have developed a method to measure the resulting adhesion forces using deformable substrates. We have demonstrated that focal adhesions are dynamically established and ruptured, with a bias towards the old poles. We have also probed the role of adhesion in the shape of the colony. We have shown that polar adhesion drives the transition from a linear to a two-dimensional growth after the first division. At larger colony sizes, the level of adhesion continues to correlate with the global shape of the colony. Finally, adhesion is involved in the transition from a two-dimensional to a three-dimensional colony. Taken together, our results suggest that the expression of adhesins and their location at the surface of the cells could be levers by which bacteria actively modulate the shape of the group in which they reside.

Contents

Foreword

A lot of living species tend to organize in communities. From wildebeest herds to bird flocks or wolf packs, from human cities to insect nests, congregating requires a certain level of organization, especially regarding the access to external resources. Indeed, living in a group, individuals can benefit from interactions with the other members. On the other hand, having many individuals in the same place, or even in proximity, changes the way a given individual interacts with the environment. From this perspective, the geometry of the group seems to be determining for the survival of its individuals.

Bacteria are no exception to this trend and develop macroscopic sessile colonies called biofilms. These communities can display different shapes depending on various environmental and internal factors. Some morphological characteristics are associated with a particular function in term of accessibility to the external resources. A question one can then ask is how these particular shapes are being generated. Although biologists have tackled this question from a biochemical perspective, there is still no clear mechanical framework to understand the formation and development of such colonies.

In the present work, we focus on the formation of monoclonal microcolonies growing from a single rod-shaped bacterium, confined in two dimensions. Although it is mechanically simplified, non trivial phenomena seemed to happen in this configuration. In particular, the final shape of the colony does not reflect the symmetry of its elementary components. This project emerged from discussions about the origin of the transition from a linearly growing bacterium to a compact two-dimensional microcolony. Three years of work have turned these discussions into this manuscript. The first chapter describes the biofilm way of life and details bacterial features that are likely to influence the colony morphology. The second chapter presents the experimental techniques that we developed to probe the mechanical interactions at play in the colony morphogenesis. The third chapter gathers our measurements and our current understanding of the growth mechanics of bacterial

microcolonies. Finally, appendices provide the description of the strains we used, detailed experimental protocols, growth characteristics measured in our conditions and preliminary experiments that still nourish our discussions.

Chapter 1

Introduction

Bacteria are one of the three first branches of the phylogenetic tree together with archaea and eukaryotes. They are unicellular microorganisms which size is generally on the order of a few micrometers. Unlike eukaryotes, they have no nucleus and their genome is usually displayed as a circular chromosome. The genome size is generally smaller than 10 millions base-pairs [1]. Bacteria proliferate by division with very short generation times (typically less than an hour in rich environments). Well adapted over a wide range of environmental conditions [2], they are considered to be the most abundant form of life on Earth [3].

For a long time, bacteria have only been considered as deleterious organisms [4], certainly because of the large number of deaths they have been causing in pandemic infections such as plague (200 millions deaths through time [5]), cholera (hundreds of thousands [6, 7]), tuberculosis [8]... However, this perspective has recently been changing. Studies about obesity [9], immunity [10] or anxiety [11] have shown that a proper microbiota [1] is required for good health. Moreover, bacteria start to be seen as promising actors in a variety of industrial processes such as power [12] and biochemicals [13, 14, 15] production, agriculture [16, 17]...

1.1 The biofilm, a sessile bacterial colony

1.1.1 Context

Most bacteria are able to swim individually. Sampling their surroundings, they maximize their interactions with the environment. Alternatively, they

1. The microbiota is the ensemble of microorganisms that live in the human body.

can form sessile colonies, biofilms, at interfaces: liquid/solid, liquid/air or solid/air [18]. Biofilms can reach millimetric sizes and high cell densities within hours. In such configurations, bacteria maximize their interactions with their neighbors, either from similar or other species.

The formation of such structures is a common feature to most bacterial species and some archaea [19]. Some fossile biofilms have been identified in 3.2 billions-year-old formations in South Africa [20] and Australia [21]. In the early 1940's, it has been quantified that aquatic bacteria are more numerous on solid surfaces than as single suspended cells [22]. Since then, it has been commonly admitted than most of the bacterial biomass should be found in biofilm structures. Their predominance is ubiquitous since bacterial biofilms are found in various contexts going from hydrothermal hot springs [19] to glacier streams [23], from soil and plants [24], gums and teeth of many animals [25] to inorganic surfaces.

Since bacteria can colonize biotic and abiotic surfaces to form biofilms, they represent a real medical challenge. Serious and potentially lethal infections, like cystic fibrosis pneumonia [26] or infectious endocarditis [27], are caused by biofilm development in respectively the lungs or the heart of a human host. The ability of bacteria to colonize catheters and medical implants make them a major cause of nosocomial infections [28]. From this perspective, understanding the bacterial behaviors inside a biofilm and the characteristics of a biofilm as a whole become crucial scientific issues.

Bacterial biofilms also have an influence in the industrial world. Their presence can be detrimental when they colonize heating or cooling systems, any kind of pipeline networks and even boat hulls increasing significantly the drag force and thus limiting the speed of ships [29]. On the other hand, some industrial processes take advantage of these hardly avoidable colonizations. Biofilm are for instance used as corrosion inhibitors or biocontrol agents [30].

1.1.2 Biofilm physiology

Rheological studies on a variety of biofilms have shown a viscoelastic response –elastic at short times and viscous at long times– with similar timescales of few tens of minutes for a large variety of biofilms [31]. Biofilms are mechanically cohesive due to a secreted extracellular matrix that glues bacteria together. This matrix is composed of entangled polymers such as polysaccharides, DNA, proteins and sometimes lipids. Compared to planktonic life, the biofilm offers a protective shell against environmental stresses [32]. For instance, biofilms have been reported to be up to 1000-fold more tolerant to specific antibiotics than their planktonic counterpart [33, 34, 35].

They are also less vulnerable to the immune response of an infected host [36, 37]. More generally, biofilms increase bacterial resistance to UV damage [38, 39], desiccation [40], acidification [41], heavy-metal exposure [42, 43] and even predation [44].

The morphology of the biofilm

The morphology of biofilms has been reported to strongly depend on environmental factors. In fast-moving water, biofilms tend to form filamentous structures like streamers whereas in quiescent water, it is more likely to observe mushroom or mound-like structures [19]. More generally the symmetry of the biofilm reflects the geometry of the environment. Nutrient composition also influences the morphology [45]. For instance, *Pseudomonas aeruginosa* forms flat biofilms in citrate minimal medium whereas it gives rise to mushroom-like structures in glucose minimal medium [46]. Similarly, iron availability was shown to influence the morphology of biofilms [47]. The geometry of a biofilm governs its surface of interaction with the environment. Biofilm geometries have been adapted to maximize bacterial growth. For instance, at a solid/air interface, *P. aeruginosa* forms wrinkly structures that enhance its access to oxygen [48].

The level of matrix production can vary depending on the environment, and especially with the growth medium [49]. Part of the relation between shape and environment may be due to the modulation in matrix production.

Phenotypic and genetic variability inside the biofilm

Zooming in a biofilm reveals heterogeneities at different levels.

First, chemical concentrations are not homogeneous. Oxygen-profiles have been measured with microelectrodes [50, 51, 52, 53] inside macrocolonies. In most cases, the concentration appeared to decrease when progressing deeper inside the biofilm far from the oxygen source, to end up with totally anaerobic regions. Such gradients have also been reported for nutrient distribution and pH [54] caused by acid wastes due to fermentation regimes. These gradients have been well described by reaction-diffusion models that take into account both the diffusion of chemicals through the matrix environment and the local consumption or production by bacteria [55]. The location of external sources is another determining factor in the gradient establishment. These locations are determined by the biofilm geometry itself. Depending on the situation, some nutrients are coming from the top or the

bottom [18].

Second, these chemical gradients lead to phenotypic heterogeneities inside biofilms. For instance, cells could either be in a vegetative state in which the population grew, or in a stationary phase in which cells only maintained essential processes [56]. For most of the studied species, two spatially distinct regions seemed to emerge, delimited by intermediate zones where both states were represented [18]. The location of each phenotypic state depended on the nature of the limiting nutrient and on the geometry of the experiment. For instance, macrocolonies growing on agar plates have been studied for *P. aeruginosa* and *E. coli*. This configuration implied that oxygen was brought from the top and nutrients from the bottom. For *P. aeruginosa*, oxygen was the limiting chemical since it is essential to keep the cell metabolism active. In this case, a top layer (with a maximal thickness of about 60 μm) of cells exhibiting active protein synthesis was depleting the oxygen in the lower parts of the biofilm where, as a consequence, cells were metabolically inactive [57, 58]. Being inactive, the lower layers allowed nutrients to diffuse to the top layer. On the other hand, *E. coli* can obtain energy in anaerobic environments through fermentation. Therefore, in the case of *E. coli* macrocolonies, the diffusion of nutrients from the bottom layer was the limiting factor for growth. Vegetative cells were found in a bottom layer whereas upper parts of the biofilm were composed of inactive cells [59]. More complex cases have also been studied. In hostile conditions, *Bacillus subtilis* can enter a sporulation state that was found in biofilms together with vegetative swimming bacteria and matrix-producing cells. The location of these three different states was correlated with the nutrients concentration. In nutrient-rich zones (bottom and edges), flagellated cells were dominant. Matrix-producers and sporulating cells were respectively found inside the biofilm and in the top part, where nutrient concentration was limited [60]. If these three locations seem reasonable in terms of strategies for expansion, cohesion and dispersal, the mechanism responsible for this spatial differentiation was not initially clear, especially for explaining the location of matrix-producers and spores. Indeed, nutrient-depleted conditions inside the biofilm were expected to trigger the sporulation process. Cannibal behaviors through toxin secretion have been reported [61] for matrix-producers. Nutrient supply from surrounded cannibalized cells has been proposed as a mechanism postponing the sporulation process in the inner part of the biofilm. A schematic view of these three examples is displayed in figure 1.1.

The previous observations rely on the ability to identify different physiological states. A parallel has been made between scanning electron mi-

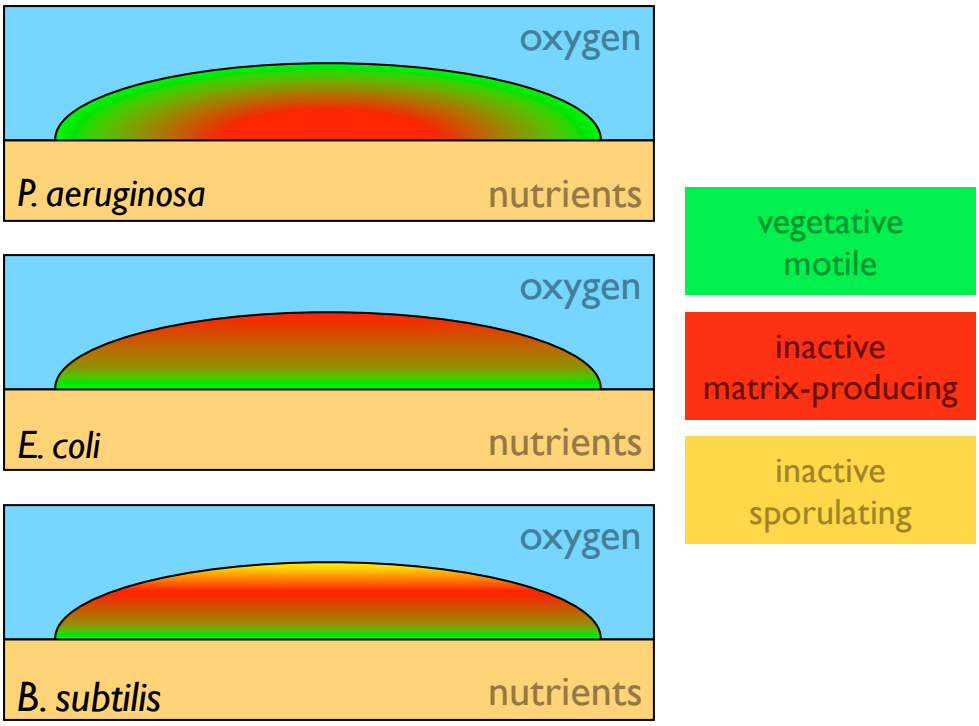

Figure 1.1 – Spatial distribution of different metabolic states and phenotypes for different strains biofilms grown on nutritive agar plates.

croscopy of biofilm slices and light microscopy of nutrient-limited planktonic cultures [2] [66] since late phases of planktonic cultures resemble the biofilm situation. In addition, phenotyping could be achieved by looking at the set of σ factors expressed in the biofilm that have their counterpart in different stages of the planktonic culture. For *E. coli*, the couple σ^{70} and σ^{FliA} is responsible for the flagellar expression whereas the general stress response factor σ^{S} triggers, for instance, polymer secretion [67]. Homologous σ factors have been reported in other strains [68]. Based on these statements, an approach using engineered strains with fluorescent fusion reporters on the genes

2. A bacterial population grows exponentially as long as nutrients are not limited; when nutrients become limited, bacteria divide less frequently and become highly flagellated to be able to sample more space in order to search for nutrients [62, 63, 64]; when foraging become inefficient, they finally enter into a stationary phase where bacteria become smaller, ovoid rather than rod-shaped [65], unflagellated and, in some case, spend their last resources in producing extracellular matrix-component.

of interest, or under the same promoters, enables to quantify the expression of these genes and to assess their spatial distribution inside the biofilm.

Beside this phenotypic variability, genetic diversity has also been reported in biofilms [24]. Mutations are expected to occur due to the large number of bacteria present in biofilm structures. Yet, the number of genetically different cells is too high (10% or more of the overall population within a few days [69, 70]) to be explained by random mutations only. With such environmental heterogeneities in the biofilm, it has been considered that random mutations could be enriched by selection processes due to heterogeneities. Indeed, a fitter mutant could appear in a particular zone of the biofilm and colonize this particular microniche [71]. Horizontal gene transfer has also been reported in both mono-species and multi-species biofilms [72, 73, 74]. This phenomenon probably accounts for a part of the genetic diversity in biofilms grown from clonal individuals.

Biofilms are complex bacterial assemblies that are spatially structured. The biofilm organization is beneficial to the group. Biofilm morphogenesis dynamically adapts in order to regulate the position of the cells with respect to nutrient sources, which in turn modifies the chemical gradients established in the biofilm.

1.1.3 Biofilm formation

Microscopic and macroscopic observations support the idea that the transition from a free-swimming state to a sessile state proceeds in successive, distinct steps (see figure 1.2) [19, 75, 76, 77, 78]. First, a planktonic bacterium attaches to a surface in a reversible manner. This weak attachment can be unbound, by shear forces for instance, or mature into an irreversible attachment. From there, the bacterium divides to give rise to a small cluster of bacteria called microcolony. This stage can also be achieved by recruitment of other attached bacteria moving on the surface or in the flow. Later on, the microcolony grows into a complex 3D structure, as described in paragraphs 1.1.1 and 1.1.2. From these mature biofilms, some cells can escape. This dispersion process can take various forms. Some isolated cells can detach and recover a planktonic lifestyle. Some aggregates can be torn apart. For biofilms developing at the interface with air, spores (in the case of *B. subtilis*) can be dispersed in the environment before switching back to a vegetative life when conditions become favorable again.

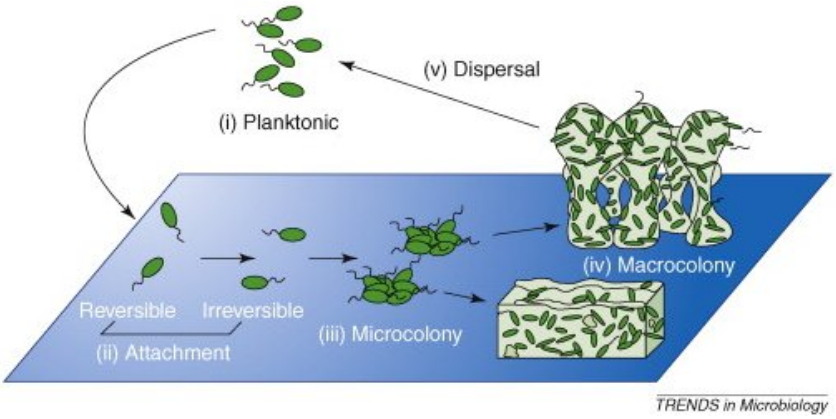

Figure 1.2 – The different steps of biofilm formation.
This figure was initially displayed in [78].

1.2 The bacterial cell cycle

Bacteria can be classified into two categories depending on the nature of their envelop (see figure 1.3a). *Gram-positive* bacteria have their cytoplasmic membrane covered with a thick layer of entangled peptidoglycan polymers. *Gram-negative* bacteria have a thinner layer of peptidoglycans that are themselves enclosed in a second membrane. The space between the inner and the outer membrane is defined as the periplasm. In this thesis, I will focus on the study of the rod-shaped Gram-negative bacteria *E. coli* and *P. aeruginosa*.

The cell cycle unfolds in two steps: (i) first, the cell elongates longitudinally, (ii) then a septum constricts the bacteria in its middle in order to complete cell division. During the elongation phase, new peptidoglycan insertion is homogeneously distributed as patches along the cylindric part of the *E. coli* rod [80, 81]. Poles are excluded from this process and considered as inert parts, since the two caps remain constituted of the same peptidoglycan molecules [82]. However, for certain bacteria like *Corynebacterium glutamicum*, the trend is reversed and new peptidoglycans are inserted at the poles [83, 84, 85]. These two alternative growth patterns have been associated with the presence in the genome of the actin-like cytoskeletal protein MreB since all the observed polar growing bacilli are lacking this protein.

Both the peptidoglycan and the MreB protein are known to play a role in the maintenance of a rod shape. Indeed, the deletion of one or more peptidoglycan insertion catalyzers in *E. coli* leads to bacteria showing abnormal

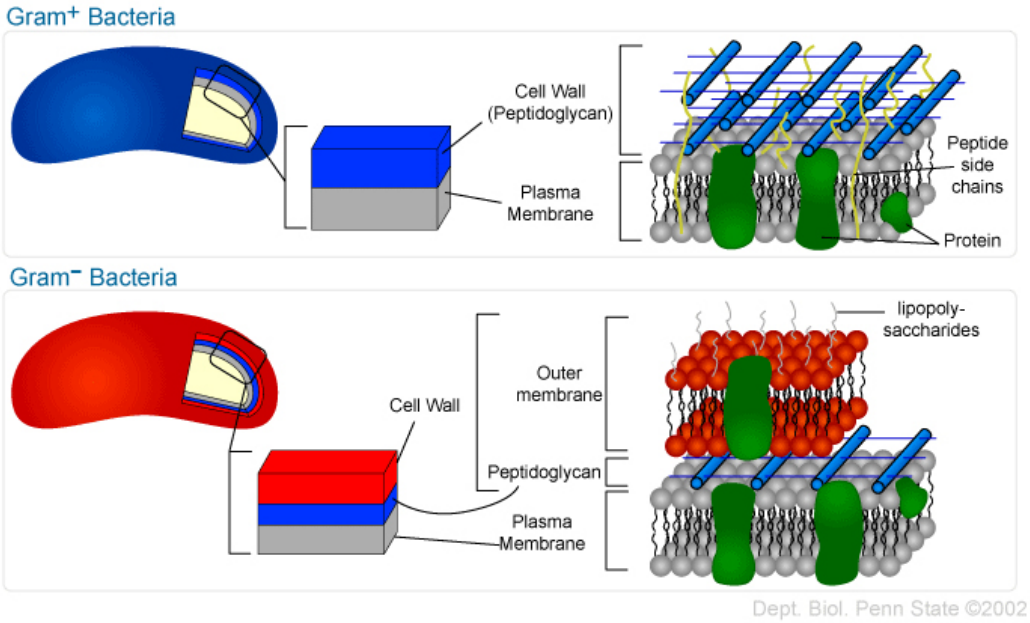

(a) Envelop structure for Gram-positive and Gram-negative bacteria.

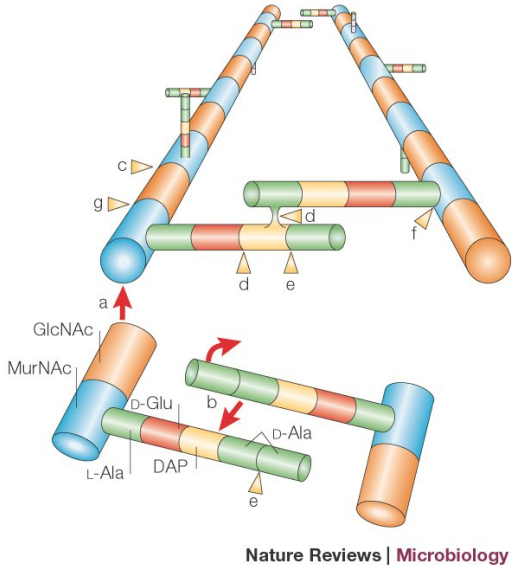

(b) Peptidoglycan structure.

Figure 1.3 – Location and structure of the bacterial peptidoglycan.
The structure of the blue peptidoglycan bars shown in scheme (a) is explained in (b). Red arrows indicate insertion reactions (a: transglycosylation and b: transpeptidation) and yellow arrowheads indicate cleavage activities. (a) and (b) were respectively adapted from the Penn State University's education website and from [79].

irregular morphologies [86]. Similarly, MreB deletion mutant strains display a spherical regular shape [87, 88, 89]. Moreover, an antibiotic induced depolymerization of the MreB filaments resulted in a decrease in bending stiffness of the bacterium [90]. If it is easily understandable that maintaining the cell integrity is crucial for the cell survival, particular shapes also involve specific functions and advantages [91]. For instance, a rod-shaped bacterium will expose more surface to its environment than a coccus of the same volume, which may help to get a larger access to diffusive nutrients for equivalent metabolic needs. In the case of adhesion, an elongated bacterium has a larger part of its envelop in contact with the surface, which promotes adhesion processes.

1.2.1 Elongation

The peptidoglycan layer confers the cell its mechanical integrity. Its elastic and robust structure resists the high internal turgor pressure [92]. Its importance is emphasized by the high efficiency of antibiotics targeting its synthesis: for instance, most of β-lactams antibiotics bind to a class of proteins, the penicillin-binding proteins (PBPs), that catalyze the cell wall insertion process [93]. For most bacteria, the peptidoglycan is composed of long glycan chains that are crosslinked by flexible peptide bonds (see figure 1.3b). The thickness difference observed between Gram-positive and Gram-negative cell walls is due to the number of peptidoglycan layers. *E. coli* peptidoglycan is composed of a single layer on 80% of the surface but can count up to three layers [94]. Since this number is quite low, the insertion of new material is a delicate process that has to be made without damaging the mechanical integrity of the whole structure.

For the Gram-negative bacteria *E. coli* and *Caulobacter crescentus*, the peptidoglycan strands have been observed to be mainly circumferential and oriented perpendicular to the long axis of the cell [95]. The two main precursors molecules that will compose the peptidoglycan chain, are synthesized inside the cytoplasm. They assemble into two successive lipid complexes. The second one binds a lipophilic membrane acceptor, called bactoprenol, that enables the lipid translocation through the inner membrane. Before any insertion of new material inside the peptidoglycan mesh occurs, some covalent bonds have to be broken (see yellow arrowheads in figure 1.3b). This role is fulfilled by periplasmic peptidoglycan hydrolases, called autolysins. Next, two reactions are necessary to insert the new peptidoglycan strand: (a) during the transglycosylation, it is inserted in the circumferential glycan chain, then (b) during the transpeptidation, neighboring glycan chains

are cross-linked via peptide-peptide bridging (see red arrows in figure 1.3b). These reactions are catalyzed by the PBPs and the lytic transglycosylases [96, 97, 98].

Although crucial to avoid cell autolysis, the way glycan chain cleavage and new material insertion are coordinated remains unclear. Yet models have been proposed [97]. A three-for-one model suggests that three new glycan strands could be inserted in the inner part of the mesh to eventually replace a now obsolete single strand. Such a model is consistent with the observation that a large part of the total peptidoglycan material is removed from the cell wall –40 to 50% per generation [98]– and recycled for new glycan synthesis [99].

MreB polymerizes in short filaments oriented perpendicular to the cell axis [3]. These filaments colocalize with enzymes and molecules involved in the peptidoglycan synthesis [103], for instance MurG that catalyses the transglycosylation [104]. Moreover, the movement of these filaments is strongly linked to the cell wall insertion machinery since they stop when the cell is exposed to antibiotics targeting cell wall assembly [105, 106]. Thus, MreB is suspected to play a role in the peptidoglycan recruitment [107].

1.2.2 Septation

During the septation phase, cell wall is preferentially added in the septum region [81] and colocalizes with both MreB and FtsZ. FtsZ is another cytoskeletal protein which is a tubulin-homologue [108]. Like tubulin, it can assemble in protofilaments [109]. During septation, it forms a dynamic polymer structure [110], the Z-ring, that is tethered to the cytoplasmic membrane by the FtsA [111] and ZipA [112] membrane proteins. The location of the Z-ring is ensured by the ensemble of MinC-D-E proteins. Their pole-to-pole oscillation creates gradients of division inhibitor with a minimal concentration at mid-cell. Thus, septum formation is prevented anywhere but in this particular position [113, 114]. In timelapse fluorescence light microscopy, this structure looked like a shrinking ring. However, more resolved electron cryotomographic reconstructions of *Caulobacter crescentus* septum suggested that the "ring" may instead be composed of multiple short filaments of various lengths (around 100 nm) and curvatures [115]. Change in curvature has been proposed as a way for FtsZ to transmit a mechanical work to the membrane. A GTP-bound polymer is straight while a GDP-bound polymer

3. MreB was first thought to form an helical cable, but these observations are now known to be the result of an artifact due to the protein fluorescent tag [100, 101, 102].

is curved [116]. Thus, the transition from one conformation to the other may result in a transmitted bending force as suggested by *in vitro* experiments [117]. Beside constriction, FtsZ is responsible for the recruitment of other proteins: after the Z-ring is formed, it serves a scaffold for proteins implied in the division process [118]; before the septum appears, it enhances the synthesis of peptidoglycans at mid-cell by interacting with the cell wall precursor molecule, MurG [119].

1.3 Bacterial adhesion

The bacterial cell wall is covered by a large variety of macromolecules. Some of them –adhesins– are involved in adhesion processes, either on abiotic surfaces, or on biological surfaces, including the cell wall of other bacteria. Adhesion is a crucial step in biofilm formation (see paragraph 1.1.3). Thus, the propensity of a strain to form biofilm gives an insight on the adhesive feature of this particular strain. Moreover, morphological observations of mature colonies can sometimes be linked to bacteria-surface and/or bacteria-bacteria interactions [120]. Genetic screenings can be conducted using evolved or engineered strains. Adhesion features of mutants of particular surface molecules (variant, deletion, under-expressing or over-expressing mutant) are compared with the features of a reference strain [121, 122, 123]. When the adhesion phenotype is modified, the surface molecule is considered to be implied in the adhesion process.

1.3.1 Usual adhesion assays

Experimental assays

The propensity of bacteria to adhere to a particular surface can be probed by incubating a bacterial suspension in contact with a surface, removing the liquid phase after a given time and, finally, estimating the number of adhered bacteria. An estimation of the number of bacteria which remained attached to the surface can be achieved in various ways: by staining of culture tubes residue with crystal violet [124], by re-suspending adhered bacteria in order to measure the optical density (OD) of this solution [125], by measuring the radioactive signal of labelled bacteria with a scintillator [126], or by directly counting the number of adhered bacteria using videomicrocopy [127, 128, 129, 130]. An alternative to rinsing is obtained by flipping the surface upside down to allow unbound cells to sediment to the bottom of the sample [131].

Since surface colonization has been shown to proceed in two distinct steps –a transient reversible attachment followed by a permanent attachment–, adapting the time during which bacteria are allowed to adhere, rinsing or inverting the samples can be strategies to probe preferentially one phase or the other. Microfluidic assays offer a way to look into the dynamics of adhesion by measuring time-dependent surface coverages as well as residency times [132, 133], allowing a direct distinction between transient and permanent adhesion. Moreover, microfluidic assays provide an opportunity to estimate the strength of adhesion by imposing a known shear stress (typically on the order of 1-10 Pa). Indeed, the flow rate can be converted into a drag force applied to an adhered bacterium given its exposed surface, the channel geometry and the fluid viscosity [134, 135, 136, 133] . Although this method does not measure directly the strength of adhesion, it gives a lower bound of the force necessary to detach bacteria (typically, F>10pN).

During the 80's, more direct measurements of adhesive forces were obtained by measuring the contact angle of a bacterial suspension spread over a surface of known interfacial energy [128, 129, 137]. From these measurements, we estimated the adhesive force per bacteria to be on the order of 600 pN. During the 90's, atomic force microscopy (AFM) has been developed and used to probe bacterial adhesion. Bacteria were coated on a surface, either a substrate [130, 138] or the AFM tip [139, 140], and presented to the surface on which adhesion was probed. Measured forces corresponded to the detachment of a group of adhered bacteria from the latter surface. Forces were on the order of several nN. Similar order of magnitudes were measured while removing a cluster of adhered bacteria by centrifugation [141].

AFM was then used to probe the interaction between a single bacterium and a surface. In this configuration, the AFM tip served to detach laterally a cell, either by pressuring the bacteria between the cantilever tip and the surface [138, 142, 141], or by vertically pulling on it [143]. Measured forces were on the order of several hundreds of pN. Similarly, detachment assays were performed using optical tweezers [144] which yielded lower values (10-100 pN). Alternatively, flow experiments were conducted to measure the forces necessary to detach adherent bacteria in a micro-channel [135] (150 pN).

Finally, forces required to break single bonds were measured either by AFM [145] or by optical tweezers [146, 147]. The two techniques yielded distinct results. AFM measurements were on the order of 100 pN, while optical tweezers measurement were on the order of 20 pN.

Level	Strain	Substrate	Technique	Value	Ref.
Global	*E. faecalis*	Polyurethane	AFM	19 nN	[138]
		Polyamide	AFM	6 nN	
	E. coli	Various	AFM	nN	[140]
	E. coli	PLL glass	Centrifugation	1.12 nN	[141]
	E. coli	Silicon nitride	AFM	1.2 nN	[130]
	E. coli	Hematite	AFM	From 0.8±0.4 nN	[139]
		Corundim		to 6.3±0.7 nN	
	E. coli	Polymers	Contact angle	600 pN	[128]
Single-cell	*P. aeruginosa*	Xerogel	AFM	30 nN	[142]
	S. aureus	Xerogel	AFM	6 nN	[142]
	E. faecalis	Polyfluoretylen	AFM	0.7 nN	
	E. coli	Stainless steel	AFM	763±167 pN	[141]
		PLL glass		639±136 pN	
	X. fastidiosa	Glass	Flow	147±11 pN	[135]
	E. coli	Mannose glass	AFM	100 pN	[143]
	E. coli	Galabiose	Optical tweezers	10-100 pN	[144]
	E. coli	Mannose	Flow	>10 pN	[134]
	P. aeruginosa	Glass	Flow	>10 pN	[133]
	C. crescentus	Glass	Flow	>10 pN	[136]
Bond	*M. tuberculosis*	Heparin	AFM	120 pN	[145]
	S. aureus	Fibronectin	Optical tweezers	25 pN	[147]
	E. coli	Mannose	Optical tweezers	1.7 pN	[146]

Table 1.1 – Summary of the measured adhesion forces with different techniques.

Adhesion specificity

As emphasized by the previous results, bacteria do not adhere with equal strength on every surface. The techniques mentioned above have been used and adapted to probe the interactions with different surfaces. First, different bare materials were tested: glass [127, 131, 135], polystyrene [125, 129], mineral crystal [139], polydimethylsiloxane (PDMS) [133]... To test the influence of physico-chemical parameters (hydrophobicity or charge for instance) on adhesion, more controlled experiments have been carried out to compare adhesion on surfaces differing only by given physico-chemical properties [126, 148].

In order to probe biochemical specificity, adhesion assays have also been performed with substrates coated with biological molecules, like Bovin Serum Albumin (BSA) [137], polylisine [141], mannose [132, 146], galabiose [144]... It turned out that some adhesins are able to specifically recognize some of

these molecules, mannose and galabiose for instance. Structural analyses emphasized the specificity of some proteins with environmental molecules [149, 150].

Recent studies focused on the influence of the substrate stiffness on adhesion, revealing a mechano-sensitive effect. A weaker adhesion with increasing stiffness was observed on PDMS surfaces of rigidities ranging from 0.1 to 2.6 MPa [151]. On the contrary, adhesion was enhanced for increased stiffnesses on surfaces made of polyelectrolyte multilayer (PEM) thin films rigidities ranging from roughly 1 to 100 MPa [152].

1.3.2 Surface proteins implied in adhesion

In Gram-negative bacteria, secretion of surface proteins is challenging because of the two membranes. Thus, secretion is achieved by different pathways.

Type I fimbriae secretion via a chaperone usher pathway Bacterial fimbriae are μm long pili. They are secreted at the surface of the cells (see figure 1.5). They are composed of subunits, called pilins, and terminated by an adhesive protein, the adhesin tip, that can bind specifically to certain types of surfaces. Subunits are transfered to the perisplasm via the Sec secretion pathway [4] where they bind to a chaperone protein that assists the protein folding [155] and prevents the polymerization. The pilin is then translocated through the outer membrane pore formed by the usher protein [156]. The usher protein also serves as an anchorage for the pilus (see figure 1.5). The tip protein is the first one to go out and the pilus grows by addition of new subunits at the usher location [157, 158, 159, 160]. *E. coli* displays many fimbrial structures secreted this way [153]. One of the most commonly studied is the type I pilus, encoded in the *fim* operon. They are not always expressed (phase-variation), bacteria can randomly switch from a state in which they produce type I pili to a state in which they do not. Switching rates are on the order of 10^{-3} per cell per generation [161]. FimC is the chaperone protein, fimD, the usher. Thousands of copies of fimA, the pilin subunit, polymerize into an helical rod structure terminated by a single copy of successively fimF, fimG and fimH, the tip adhesine [162]. Type I pili are involved in the adhesion process and are required for biofilm formation,

4. The Sec secretion pathway is a type II secretion system. It enables the transport of proteins in an unfolded form through the inner membrane [154].

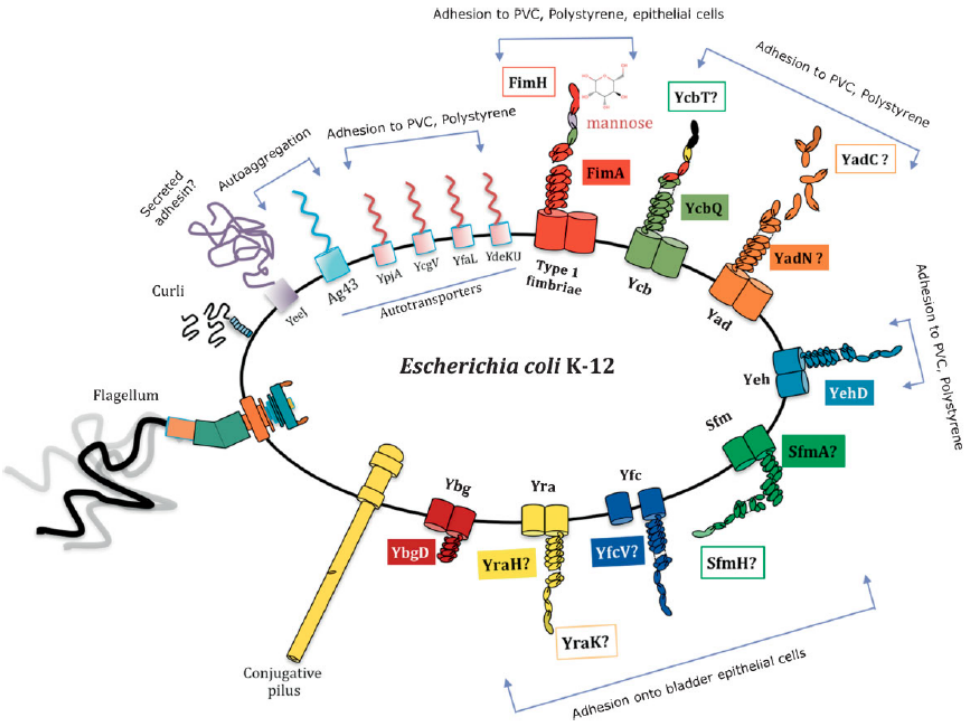

Figure 1.4 – Adhesion protein for *E. coli* K-12 as described in [153].

in particular for the initial attachment [121, 163]. FimH can bind specifically to mannose [164]. In flow conditions, the adhesion strength has been observed to increase with shear [165, 132]. A structural mechanism based on allostery has been proposed for this catch-bond [166, 149]. As many other Gram-negative bacteria [167], *P. aeruginosa* also expresses chaperone-usher secreted fimbriae, encoded in the 5 gene clusters, cupA to cupE [168]. Similarly to *E. coli*, their role is important for biofilm initiation [122].

Autotransporters secretion via the type V secretion sytem The type V secretion system enables proteins to cross the outer membrane. They are usually transported to the periplasm by the Sec secretion system [169]. Once in the periplasm, a part of the protein nucleates a transmembrane β-barrel pore, allowing the other part of the protein to be translocated and anchored to the membrane (see figure 1.5) [170]. Autotransporters are examples of type V secreted proteins [169, 171, 172]. Antigen 43 (Ag43) is an autotransporter adhesin. It is involved in auto-aggregation [123, 173, 174]. There is a phase variation in its expression with switching rates of the order of 10^{-3} per cell per generation [175, 176]. Other autotransporter adhesins have been discovered lately. Their expression is cryptic but when expressed, they are promoting adhesion to abiotic surfaces like PVC [177].

Curli amyloid fibers secretion via the extracellular nucleation/precipitation pathway Curli are highly stable 6-12 nm wide and 0.5 to 1 μm long, non-branching fibers [179] that form extracellular polymer clusters (see figure 1.5). Specific curli genes are located on two divergent operons: csgBAC and csgDEFG. The major curli subunit, csgA, is secreted under a soluble form in the extracellular environment through a 2 nm wide pore composed of csgD subunits. Inside the periplasm, csgE prevents the polymerization of csgA [182]. On the other hand, in the extracellular environment, csgA polymerization is nucleated by the csgB minor subunit [183], which is anchored to the outer membrane by csgF (see figure 1.5). For wild-type *E. coli* strains, curli expression is significant in stationary phase (under regulation of the master stationary phase regulator σ_S), at low temperature (below 30 $^\circ$C), in high osmolarity and low oxygen conditions [184, 185]. The expression of curli is positively regulated by the transcription factor OmpR [186]. A mutant on this protein lead to a strain (OmpR234) displaying increased surface colonization, biofilm and aggregation phenotypes [184, 125, 187, 188]. It thus emphasized the role of curli in adhesion to abiotic surfaces like glass,

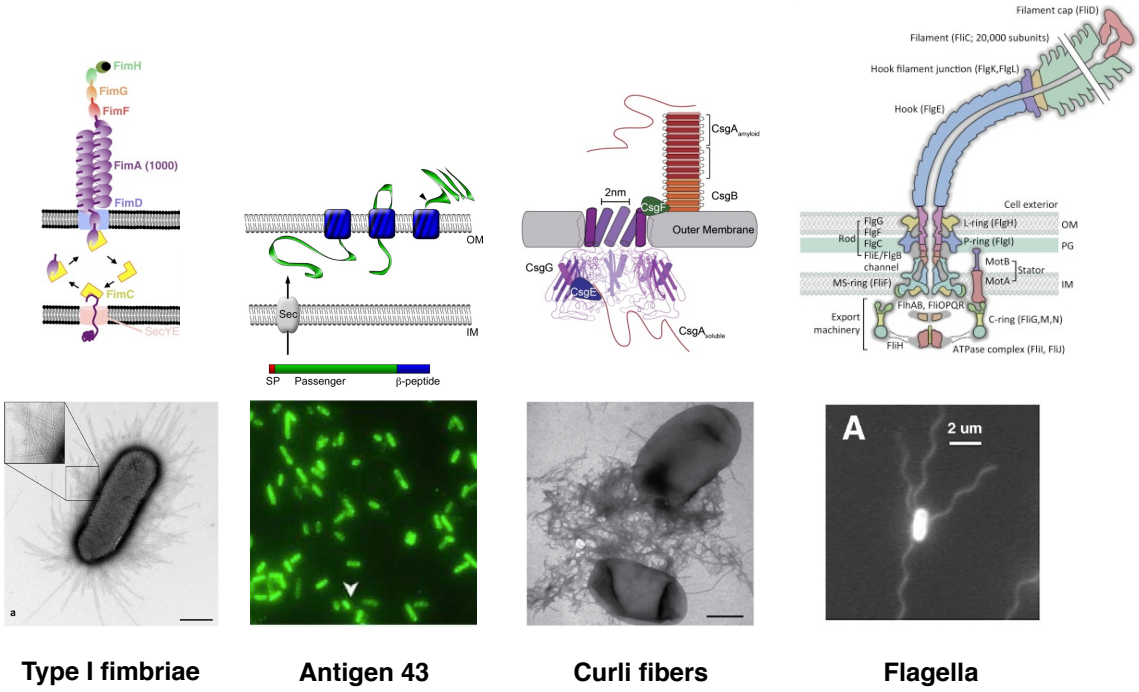

Figure 1.5 – Adhesins secretion and visualization in *E. coli*.
From left to right are displayed type I fimbriae (chaperone-usher secretion system and TEM images, scale bar is 700 nm), antigen 43 (autotransporter type V secretion system and immunofluorescence of Ag43 for a set of *E. coli* cells), curli amyloid fibers (nucleation/precipitation pathway and TEM images, scale bar is 500 nm) and flagella (structure scheme and images of fluorescent-labelled flagella, scale bar is 2 μm). Schemes and images were extracted from [159, 162, 178, 176, 179, 180, 181].

polystyrene or sand, as well as to biotic surfaces, like other bacterial cell walls, or eukaryotic tissues, through a fibronectin specific interaction.

Flagellum secretion Flagella are long –up to 15 μm– filaments rotating at the surface of cells (see figure 1.5). A flagellum is composed of 3 structures that are assembled chronologically: the basal body, the hook and the helical filament. The basal body acts as the engine of the flagellum. The stator part is composed of MotA and MotB proteins. They form transmembrane channels through which ions (H+ or Na+) can flow, providing power. The stator interacts with the rotor via the C ring, a cytoplasmic complex compose of FliG, FliM, and FliN. The rotor part also includes a membrane-supramembrane (MS) ring (FliF), a P ring (FlgI) and a L ring (FlgH), respectively going through the inner membrane, the pepdidoglycan layer and the lipopolysaccharides. These rings serve as a scaffold for the insertion of a rod (FliE, FlgB, FlgC, FlgF, and FlgG) that is linked to the other structures of the flagellum. A flexible highly curved nanometer-long hook (around 120 copies of FlgE) connects the rod to the filament, a tube constituted of up to 20 000 copies of flagellin subunits, FliC and a cap protein FliD. A type III dedicated secretion machinery is housed inside the C and MS rings and initiates the successive transport of constitutives subunits of the rod, the hook and the filament from the cytoplasm through the entire structure (see figure 1.5) [189, 190, 180, 191].

E. coli displays on average 4 flagella on its surface. They are located all over the cell envelop; yet more flagella are found close to the pole that was preexisting before the last cell division [5], probably inherited from the former cell cycle [193]. If their rotation is synchronized, they can form a bundle to propel the cell in a liquid environment. Alternating synchronized and unsynchronized regimes result in a brownian-like bacterial swimming motion [181]. Despite the fact that flagellar expression seems to be shut down during the sessile growth mode [194], flagella are required to initiate biofilm formation [121]. Moreover, the fact that the flagellar rotation is inhibited by this adhesion is seen as a probable way of sensing surfaces, and in consequence, to switch to a biofilm mode [191, 195].

A large quantity of other adhesins (see figure 1.4) can be displayed at the

5. A each division, two new poles are formed, one on each sister cells. The two former poles of the mother cell (preexisting poles) are thus one generation older than the newly formed poles (see figure 2.4). Moreover, through the preexisting pole conservation, proteins can be inherited from one generation to another [192].

surface of a cell, depending on environmental conditions, with specificity to various surfaces [153]. They can promote either cell/abiotic surface adhesion, cell/biotic surface adhesion –ranging from adhesion to neighboring bacterial cells to adhesion to eukaryotic cells which marks host invasion– and even surface motility. For instance, twitching motility is powered by the extension, tethering and retraction of type IV pili in enteropathogenic *E. coli*, *P. aeruginosa*, *Myxococcus xanthus*, *Neisseria gonorrhoeae* and *elongata* [196, 197]... However, the *E. coli* K-12 strain has not been observed to produce these pili under standard laboratory conditions [198]. Non-proteinaceous macromolecules are also secreted at the cell surface. Polysaccharides are examples of such molecules involved in the biofilm formation phenotype, and, thus, in adhesion [131].

1.4 Growth mechanics of a bacterial colony

Bacterial elongation (see paragraph 1.2) and adhesion (see paragraph 1.3) of individual cells can generate mechanical stress. When considered at the scale of a microcolony, the combination of these stresses may result in particular arrangements.

1.4.1 Evidences of mechanical stress generation

At the individual cell level, bacterial elongation can generate forces on the surrounding environment. Indeed, *E. coli* cells embedded in agarose were still able to elongate and deformed the agarose gel up to 1MPa [192], corresponding to forces on the order of 10 nN. Besides, adhesion forces developed by single bacteria on a surface have been measured to be on the order of 100 pN (see paragraph 1.3.1, table 1.1). This implies that bacterial elongation could generate large enough forces to disturb the adhesion of neighboring cells. Finally, bacteria-bacteria interactions –evidenced through bacterial aggregation– also seem to be an important ingredient of the mechanical description of microcolonies. This interaction has a tendency to align neighboring cells [199]. Although no direct measurement has yielded value for this interaction, optical tweezers have enabled to measure a repulsive force on the order of 10 pN between two *B. subtilis* cells [200].

Up to date, little work has focused on how these elements balance at the scale of a microcolony. Monolayers of *E. coli* cells have been studied in 1 μm high channels of finite width (between 30 and 90 μm). Local bacterial elongations, coupled together by lateral contacts, resulted in a long-range orientational ordering of the bacteria inside the colony, with a characteristic correlation length of the order of a dozen of cells [201, 202]. However, buckling instabilities in high pressure zones triggered rearrangements and prevented the perfect nematic order from being achieved [203]. Another study looked at the transition from 2D to 3D growth. Microcolonies were confined between a soft hydrogel and glass. In such a configuration, the colony initially develops in 2D. When the number of bacteria in the monolayer becomes large, a second layer appears on top of the first one. Both the lateral confinement from the gel and the interactions between the bacteria and the confining surfaces –modeled by friction– have been shown to play a role in this transition from 2D to 3D growth [204].

In mature 3D biofilms, buckling has also been reported and was shown to result in the wrinkles observed at the surface of *B. subtilis* biofilms [205]. Yet, in this case, the mechanical configuration is more complex due to heterogeneities (see paragraph 1.1.2) in stiffness (linked to matrix production) [206] and in growth rate (different growth regimes and cell death) [205].

1.4.2 Our approach

Taken together, these studies suggest that the balance between mechanical stresses generated by different processes can control the morphology of bacterial colonies (ordering and rearrangement, 2D or 3D growth, wrinkling...). However, the role of adhesion and its influence in this balance has been poorly studied. In particular, we wondered how colonies manage to grow while maintaining their adhesion to the substrate.

In this work, we have probed mechanical interactions between *E. coli* or *P. aeruginosa* cells and their substrate. Bacteria were observed either isolated or inside growing microcolonies, in order to study respectively adhesion without or with mechanical interactions with neighboring cells.

We restricted our study to two-dimensional growing microcolonies for the following reasons. First, from a mechanical prospective, the geometry is simpler, compared to a 3D structure. Second, biological heterogeneities are less important than in a mature biofilm where differentiation occurs. Finally, two-dimensional studies allow to image microcolonies with single-cell resolution, yielding information at the individual level. To achieve these conditions, we imposed a two-dimensional confinement. Yet, as in the 2D to 3D transition study [204], bacteria eventually overcame their 2D confinement and started growing in 3D. We also provide an analysis of this transition.

Chapter 2

Materials and methods

Most of the experiments described in this chapter use time-lapse microscopy to image clonal microcolonies growing as monolayers. They were confined in two dimensions in order to ease their segmentation by image analysis so as to keep single-cell resolution for a significant time.

2.1 Microscopy

Video microscopy was performed on three different inverted motorized microscopes which allowed multi-positioning.

Leica SP8 Experiments presented in section 2.3.3 for morphological analysis were performed with a Leica SP8 confocal microscope equipped with a 40x/NA 1.30 phase oil-immersion objective (Apo-Ph3, Leica). Images of bacteria were acquired in a non-confocal mode using phase contrast. Transmitted light was detected on a photomultiplier tube (PMT) detector. Settings were adjusted to have a 140 nm pixel size on 1024×1024 images and pinhole size was 1 airy unit. Multi-positioning was allowed by an XY motorized stage (DMI6000). Objective position was locked on the focal plane by a Leica Adaptive Focus Control (AFC). These elements were controlled by the Leica commercial software (Leica Application Suite X). An environmental chamber (Digital Pixel, UK) fitted on the microscope enabled the regulation of the sample temperature.

Olympus IX81 Laser ablation (see section 2.4) and traction force microscopy (see section 2.5) experiments were performed using an Olympus IX81 inverted microscope. Bacteria were imaged through a 100x/NA 1.35 phase oil-immersion objective (Apo-ph1, Olympus) with a Orca-R^2 CCD

camera (Hamamatsu, physical pixel size 6.45 μm). The effective pixel size was 63.9 nm on 1024×1024 pixels images. Multi-positioning was achieved by the use of a Thorlabs XY motorized stage (MLS203-1). Epifluorescence excitation was performed using a mercury vapor light source (EXFO X-Cite 120Q) coupled with different filter sets to select the desired wavelengths. To reduce phototoxicity, GFP was imaged with a YFP 542(24)/500(27) nm filter set using a dichroic beam-splitter at 520 nm (Semrock). RFP was imaged with a 624(40)/562(40) nm filter set using a dichroic beam-splitter at 593 nm (Semrock). The different parts were controlled by a custom LabView (National Instruments) program. Two subroutines were dedicated to the 3D tracking of a region of interest. Lateral drifts were compensated by correlating two successive images. Focusing was achieved by analyzing the contrast variation in a z-stack of images. For phase contrast images, the focus z-position corresponds to a global maximum of contrast, whereas for bright-field images it corresponds to a local minimum. The focal z-position was detected according to the image type and the objective was displaced to record the final image. We used bright field images to reconstruct correlation images (see figure 3.20b). This imaging technique, described in [207], was used to enhance the contrast on the edges of the cells to ease segmentation. It is based on the acquisition of a z-stack of bright field images centered on the focal position –typically an image every 200 nm over a 6 μm range. A z-profile is extracted for each pixel and correlated with a reference profile [1]. The final intensity value of the pixel was calculated as the correlation between the pixel profile and the reference profile (see figure 3.20b). Temperature of the objective and the stage was regulated by a custom controller with a 10 mK accuracy.

Custom microscope Asymmetric adhesion assays (see section 2.3.1), reorganization following the first division assays (see section 2.3.2) and microcolony growth acquisitions (see section 2.3.3) were performed with a custom inverted microscope. Bacteria were imaged through a 100x/NA 1.40 phase oil immersion microscope (Apo-ph3, Olympus) with a ORCA-Flash4.0 V2 CMOS camera (Hamamatsu). The effective pixel size was 63.9 nm on 2048×2048 pixels images. A Thorlabs XY motorized stage (MLS203-1) was used for multi-positioning. Microscope control was performed by an adapted version of the previously described Labview program (see Olympus IX81 microscope description). The temperature control was adapted from a PicoTwist solution for a mK accuracy.

1. The reference profile $Ker(z)$ corresponds to the derivative of a gaussian function centered on the focal plane and with standard deviation $\sigma_z = 700$ nm.

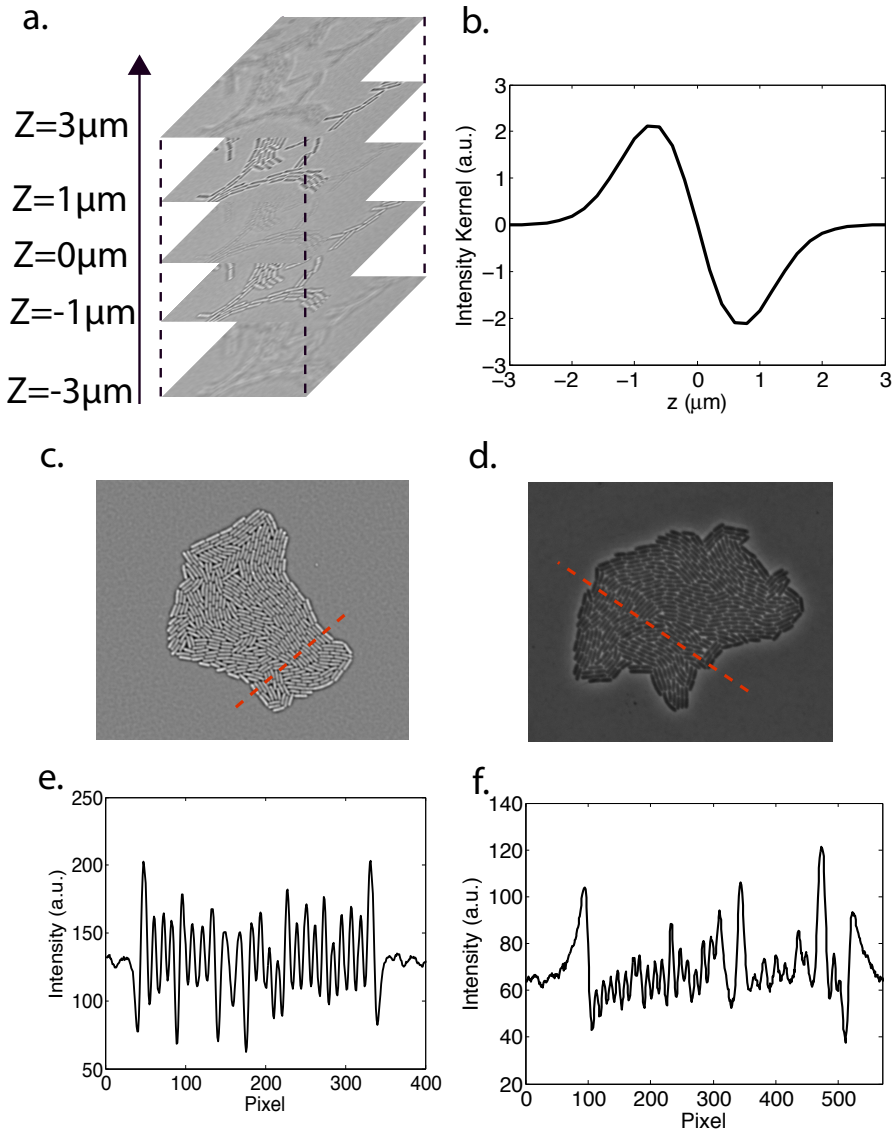

Figure 2.1 – The bright field z-stack profile (a) of each pixel is correlated with a theoretical profile (b) that is characteristic of the interior of a bacteria. By looking at the intensity profile of a correlation image (c) and a phase image (d), it appears that cells are easier to distinguish in the correlation profile (e) than in the phase profile (f) for similar colonies. This figure was extracted from [207].

2.2 Image analysis

2.2.1 Colony segmentation

Morphology and growth dynamics can be computed from the mask of the colony. Masks were obtained by binarization of either pretreated gray level images (morphological gradient) or raw gray level images (direct thresholding).

Automatic morphological gradient For phase and correlation images of bacteria growing between agarose and glass, we computed the difference between a dilated and a eroded version of the gray level image to emphasize the contour of the colony. The contour was identified by thresholding using Otsu's method [2] and filled to obtain the mask of the colony.

Semi-automatic thresholding in presence of tracers During force measurement experiments, bacteria were imaged at the same time as fluorescent beads. On phase images, these beads of diameter 200 nm have an intensity similar to the one of bacteria. To obtain the mask of the bacterial colony alone, we used a method based on direct thresholding. For each image, the threshold was calculated on a region of interest (ROI) closely enclosing the colony. Working with a ROI sized to the colony provides a distribution of pixel intensities in which a significant proportion of pixels corresponds to the colony. ROI dimensions were determined for the first image of the time stack and increased exponentially to enclose properly the colony at all times. The threshold was chosen in a range of $\pm 5\%$ around Otsu's threshold. Its determination was kept constant for the whole time stack but was tuned for each experiment to offer the best discrimination between colonies and beads. The whole image was binarised with this threshold but only the larger detected particle was kept as the colony mask. At an advanced stage of growth, the gray levels in the center of the colony approximated those of the background. Thus, masks were filled to ensure to cover the whole colony surface. When the segregation remained imperfect –bead partially under the colony and/or with exactly the same intensity– masks were corrected manually.

2. Otsu's method for the reduction of a gray level image to a binary image gives the intensity threshold that will separate pixels in two classes with the smallest intra-class variance [208].

2.2.2 Single-cell segmentation

Single-cell resolution was achieved by segmentation of phase or correlation images to get the mask of individual bacteria (see figure 2.3a). For this purpose we developed or adapted routines that were used according to the experiment specificities.

Live segmentation for colonies of a few cells

During laser ablation experiments, we had to precisely detect the number of bacteria in the field of view after the acquisition of each frame. In order to keep a single dividing cell in the field of view, an ablation was automatically triggered as soon as two cells were detected (see paragraph 2.4.2). To monitor the number of cells, we developed a robust segmentation algorithm for the detection of a low number of cells. It was used on correlation images. The image was binarized with a variable threshold. For each value of the threshold, the number of particles was measured. For correlation images, the threshold corresponding to a local minimum in particle number gave a correct segmentation at a few cells stage (see figure 2.2). This segmentation was automatically performed during the ablation at the 2-cells stage experiments.

Post-treatment segmentation

As a first step toward the lineage obtention (see paragraph 2.2.3), a post-treatment segmentation had to be performed on raw images. Routines were developed, or adapted from preexisting codes, to process different types of images.

- **Correlation images** were binarized with Otsu's method to retrieve the contour of the cells.
- **Phase images** were treated with a routine adapted from Philippe Nghe [209]. An approach based on watershedding was used. For force measurement images, tracers were present in the image with an intensity similar to bacteria's. Given the mask of the colony, the use of the routine was restricted to the colony area.

These routines were included in the Schnitzcells suite developed by Michael Elowitz's group at the California Institute of Technology (CalTech) for segmentation and tracking of bacteria [210]. The Schnitzcells suite allows a manual verification step to correct potential mistakes made by the previous algorithms since the lineage reconstruction requires a quasi-perfect segmentation of the images.

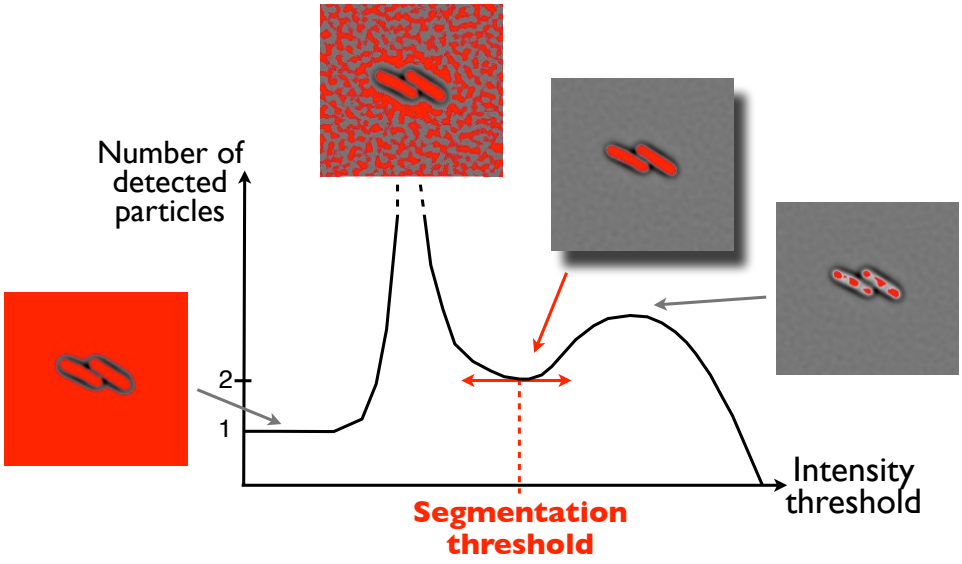

Figure 2.2 – Segmentation on correlation images.
The number of detected particles is computed for a range of binarization thresholds. When threshold is 0, the whole image is detected as 1 particle; when threshold is superior to the maximal pixel intensity, no particles are detected. The best segmentation is achieved for the local minimum in particle number.

2.2.3 Tracking

From the time evolution of a clonal microcolony, one can extract the whole lineage to retrieve individual parameters. To obtain this information, we used a Matlab suite called Schnitzcells that has first been developed by Michael Elowitz's group [210]. The computation of the lineage required an error-free segmentation of the timelapse images. In a second time, a tracking algorithm associated a bacterium in the image n with itself in the image $n+1$. This algorithm with size and position based arguments was able to detect division and death events (see figure 2.3b). The output of the routine was a structure for each cell containing the cell parameters (listed on the following page) and the identitfication of the two daughter bacteria. As for segmentation, a manual verification routine enabled the user to check and correct for potential mistakes.

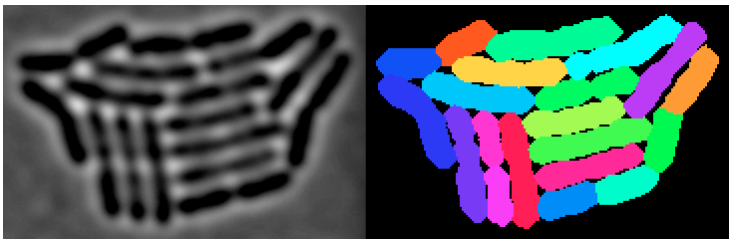

(a) Example of segmentation on an *E. coli* phase image.

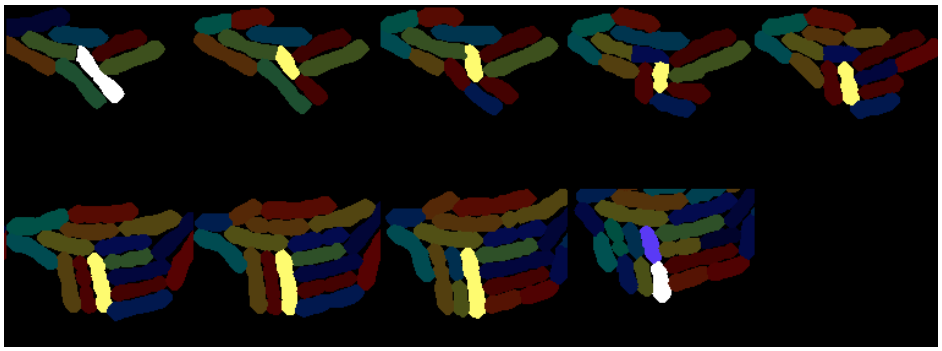

(b) Example of tracking on the same experiment.

Figure 2.3 – The two steps of the Schnitzcells analysis.
(a) Segmentation. (b) Tracking: the cell of interest is displayed in yellow. The mothercell is represented in white on the first image and the two daughters are in white and blue on the last image.

For each bacterium at each time point, we could extract:

1. parameters from the fitted ellipse:
   — the **position of the center of mass** of the cell,
   — the **position of the two poles** of the cell,
   — the **length** of the cell, corresponding to the major axis length,
   — the **angular orientation** of the cell with respect to the image axis;
2. the pole history deduced from the earlier divisions (see figure 2.4). In particular:
   — the **new pole** defined as the one closest to the septum,
   — the other defined as the **preexisting pole**,
   — the **age of the bacterium** defined as the number of generations since the preexisting pole had been formed [3];
3. the relative position of the bacterium inside the colony (see figure 2.5b) given by:
   — the **distance to the border** d, defined as the minimal distance from the center of mass of the cell to the closest border of the colony,
   — the **angular position** of the cell $\theta(t)$ with respect to an horizontal axis centered on the center of mass of the colony.

Other quantities could be calculated for one cell cycle (for each cell, from birth to division):

— the **growth rate** defined as the exponential constant of the fitted temporal evolution of the cell length (see figure 2.5a),
— the **cell displacement** defined via a **travelled distance**, $|| \Delta\vec{r} || = || \overrightarrow{r_{division}} - \overrightarrow{r_{birth}} ||$, and a **displacement orientation** α with respect to an horizontal axis centered on the center of mass of the colony (see figure 2.5b),
— the **angular position** defined as the average of the angular position over the cycle, $< \theta(t) >$.

3. Note that what we estimate as the age of the cell is always a lower estimate of the actual age of the cell. Indeed, we calculate the age of the cell assuming that the initial cell is of age 1. In reality, it could be older although we do not have access to this information.

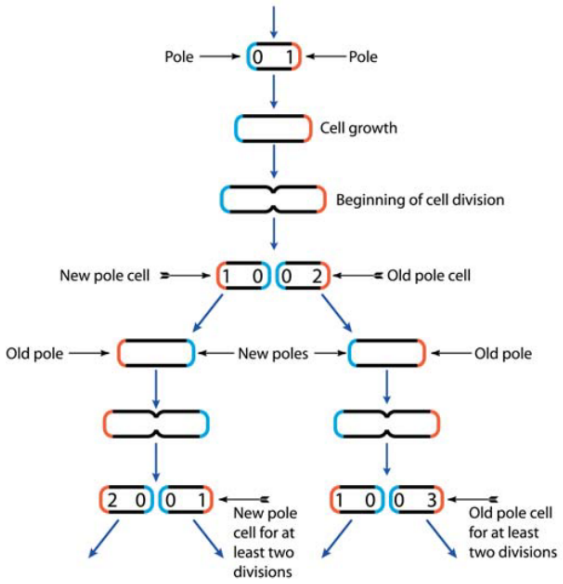

Figure 2.4 – At each division, two new poles are created (in blue, age=0). Recording the number of generations since the preexisting pole has been created, one can define an age for each cell. This figure comes from [211].

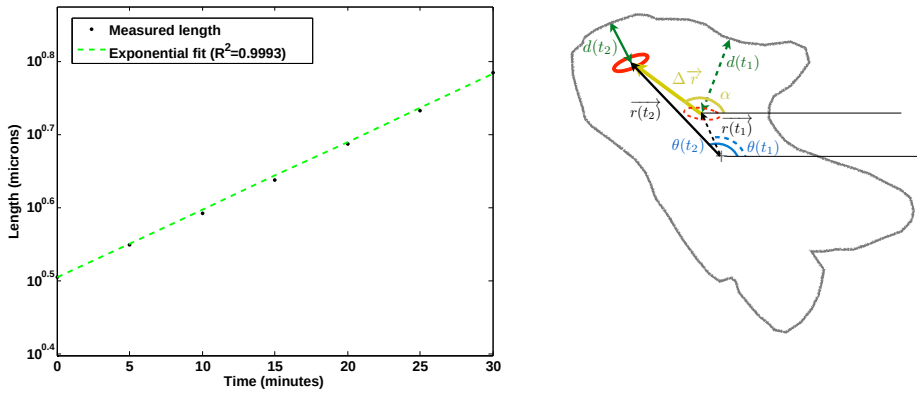

(a) Example of the temporal evolution of an *E. coli* cell length.

(b) Relative position of a cell inside the colony.

Figure 2.5 – Spatial and temporal information over a cell lifetime.
(a) The temporal evolution of the length of an *E. coli* cell is well fitted by an exponential (green dashed line). The length is represented in logscale. The characteristic constant (here 0.0214 min^{-1}) defines the growth rate. (b) The position of a given cell inside the colony can be described by a set of polar coordinates r and θ with respect to the center of mass of the colony. The distance to the border is displayed in green. Their variations over a cell cycle can be described by the travelled distance $|| \Delta\vec{r} ||$ and its orientation α.

2.2.4 Precise length measurement and fine detection of the division

For ablation at the 3-cells stage experiments (see paragraph 2.4.3), we wanted to be able (i) to detect septation with a high temporal resolution and (ii) to measure cell lengths with a high and assessable accuracy. We developed a procedure that allowed us to achieve a better precision than Schnitzcells on phase contrast images. A first segmentation image was computed with the interactive software iLastik. Then for each image, the phase contrast profile along the main axis of the segmented particle was analyzed for each cell with a Matlab routine. On phase contrast images, on the edge of the cells, the level goes from a high value (light background) to a low value (black inside the cell). Calculating the absolute value of the derivative of this profile locally gives a peak that corresponds to the border of the cell. We developed a program to precisely determine the border positions by fitting the profile with gaussian curves. The length of the cell was given by the distance between the two peaks and the error was computed as $\sqrt{\varepsilon_1^2 + \varepsilon_2^2}$, where ε_1 and ε_2 were the fit uncertainties on each peak determination. In order to detect septation, the profile between the cells was either fitted by one or two gaussian curves (see figure 2.6). The correct one was chosen based on fit relevance and variance arguments automatically and/or manually when the situation was atypical. We understood the transition from a single to a double gaussian as the completion of the division event.

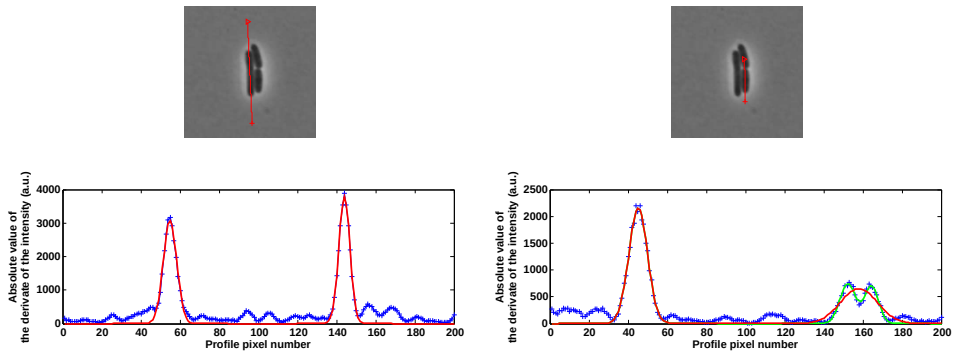

(a) Long cell length measurement. (b) Short cell length measurement.

Figure 2.6 – The edges of the cell are determined by fitting the absolute value of the derivative of the intensity profile along the cell main axis by gaussian curves. The preferred fit between one (red) or two (green) gaussian curves is automatically or manually chosen based on variance and fit relevance arguments.

2.2.5 Morphological parameters

In order to quantify and compare shapes of colonies formed by different strains (see appendix A), the following morphological parameters could be calculated from binarized colony masks (see figure 2.7b).

Circularity We calculated the area of the colony $\mathcal{A}$ as the total sum of the binary image. A smoothed contour (see figure 2.7c) could be extracted to compute the perimeter $\mathcal{P}$ of the colony. The ratio $C = \frac{4\pi\mathcal{A}}{\mathcal{P}^2}$ defines the circularity. This quantity represents the elongation of a regular shape, going from 1 for a perfect disk, to 0 for an infinitely elongated regular shape. However, a dendritic shape with a central symmetry axis will have a decreased circularity value compared to a disk, even if not elongated. This parameter should thus be used carefully.

The inverse of the normalized quadratic moment For each pixel of the surface, we calculated its distance from the center of mass of the colony. The sum of these contributions for every pixel inside the colony defines the quadratic moment. We normalized this quantity by the value of the quadratic moment for a disk, $\frac{R^4}{2}$, where R is the radius of the disk. The thus defined normalized quadratic moment is 1 for a perfect disk, and infinity for a infinitely elongated colony. In order to have a morphological parameter varying between 0 and 1, we considered the inverse of the normalized quadratic moment. This parameter presents the same limitations as the circularity.

Aspect ratio An alternative measure of the elongation of the colony is given by the aspect ratio. This measure requires the determination of two characteristic lengths for the shape. Indeed, the aspect ratio is defined as $\frac{m}{M}$, where m and M are respectively a small and a large characteristic length of the shape. We have identified three ways to define m and M:

1. along a given direction (Δ), the Feret diameter is defined as the minimal distance between two planes normal to (Δ), squeezing the object. The Feret diameter was computed in the plane of the image over a set of directions ranging from 0 to 179°. The minimal and maximal Feret diameters defined m and M (see figure 2.7d),
2. fitting an ellipse with the same normalized second central moments as the object allowed to define the minor axis length and the major axis length of the ellipse as m and M (see figure 2.7e),
3. computing the rectangle with smallest area enclosing the object gave a width and a length defining m and M (see figure 2.7f).

One should note that in case 1, the directions over which the lengths are calculated are not necessarily perpendicular contrary to cases 2 and 3. Moreover, in cases 2 and 3, a parameter quantifying the deviation from the approximating shape can be computed as the ratio between the area of the object and the area of the approximating shape. This could give a hint about the regularity of the object.

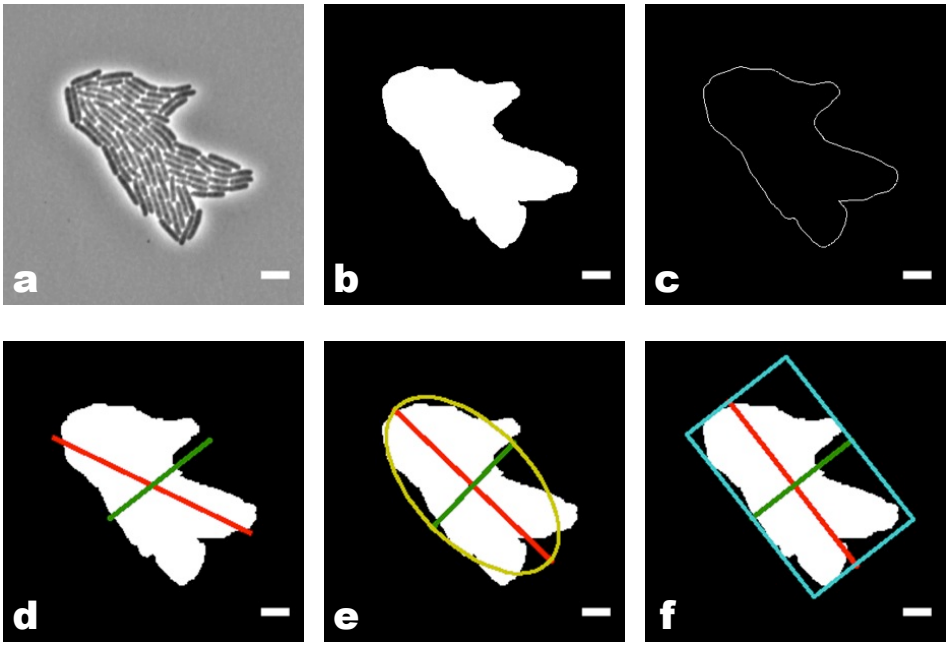

Figure 2.7 – Colony mask and morphological parameters.
From an image of colony (a), the mask (b) and its smoothed contour (c) are computed numerically. m (green) and M (red) define the aspect ratio as $\frac{m}{M}$. These characteristic lengths can be calculated with Feret diameters (case 1, d), by computing an ellipse with the same normalized second central moments as the colony (case 2, e) or by computing the rectangle with smallest area enclosing the colony (case 3, f). For this example, computed aspect ratios are 0.58 (d), 0.54 (e) and 0.61 (f) and the circularity is 0.69. Scale bar length is 5 μm on every image.

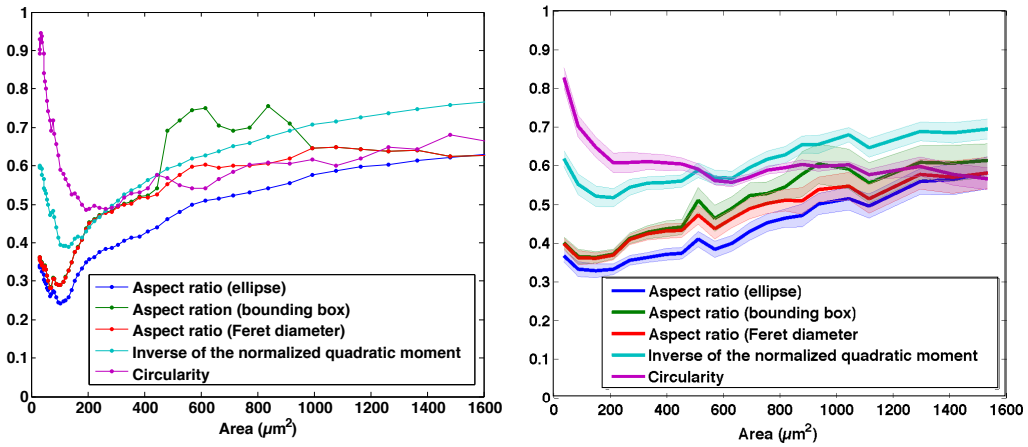

Figure 2.8 – Comparison of the morphological parameters.
The aspect ratio calculated with the ellipse (blue), the bounding box (green), the Feret diameters (red) as well as the inverse normalized quadratic moment (light blue) and the circularity (purple) are represented as a function of the colony area for a single colony growth (left) and averaged over 7 colony growths (right) for the *E. coli* wild-type strain.

We considered the five previously defined morphological parameters for the bacterial microcolonies we studied. Figure 2.8 represents the evolution with the colony area of these parameters for a single colony growth (left) and averaged over 7 colony growths (right) for *E. coli*. It appeared that integral parameters (inverse normalized quadratic moment and ellipse aspect ratio) are less noisy than the others. This can probably be explained by the fact that integral parameters are less subject to contour variations. Moreover, the inverse normalized quadratic moment and the ellipse aspect ratio seemed to follow similar trends, and thus to provide the same information about the colony morphology. Since, additionally, the ellipse aspect ratio is less sensitive to contour irregularities than the inverse normalized quadratic moment, we chose to measure colony elongations using the ellipse aspect ratio. We will referred to it as the aspect ratio in paragraphs 3.2.2 and 3.4.1.

2.3 Growth assays between glass and agarose

In order to understand how adhesion could influence the morphogenesis of microcolonies, we imaged the growth of bacterial monoclonal colonies confined between a glass coverslip and a LB-agarose gel which provides nutrients. In this configuration, we carried out different assays at distinct stages of a microcolony formation: asymmetric adhesion assays on isolated cells (see paragraph 2.3.1); reorganization assays, after the first division (see paragraph 2.3.2); finally, the growth of the microcolony could be recorded to larger stages with single cell resolution (see paragraph 2.3.3).

The strain of interest (see appendix A) was inoculated in LB from glycerol stocks and grown overnight at 37 ° C, 200 rpm. The day after, 2 μL of a diluted solution were seeded on a 1% LB-agrose pad, prepared as described in appendix B.1. The sample was sealed with a glass coverslip through which colonies were imaged. The dilution factor from the saturated culture was chosen according to the experiment requirements: 10^4-fold for a single colony in a field of view, 100 to 1000-fold for several isolated cells in a field of view. Unless mentioned otherwise, all experiments were carried at 34 ° C.

2.3.1 Asymmetric adhesion assays

More than 10 cells per field were tracked over 10 different locations in the sample. Phase contrast images were recorded every 3 minutes with the custom microscope (see section 2.1) until every present cell had undergone at least one division. Every image was then analyzed with Schnitzcells (see paragraphs 2.2.2 and 2.2.3) in order to measure the cell elongation ΔL and the position of the center of mass of the bacteria $\overrightarrow{X_{CDM}}$ with time. For each cell, we fitted the elongation ΔL versus the displacement projected over the axis of the cell $\Delta X^{\parallel}_{CDM}$with a linear law $\Delta X^{\parallel}_{CDM} = A \cdot \Delta L$. The slope A of this fit gave the asymmetry parameter. Typically, the fit was computed over 20 points.

2.3.2 Reorganization following the first division assays

For each experiment, one field of view with 1 to 3 isolated cells was imaged in phase contrast with the custom microscope (see section 2.1). Before any division, the growth of single cells was recorded with a 30 seconds frequency (low frequency). As soon as one cell was close to complete division, subsecond acquisition (high frequency) was switched on manually in order to

image the reorganization [4]. After reorganization, the low frequency acquisition was resumed until a second bacterium in the same field of view started to form a septum or until every bacterium had undergone a second division. The high frequency was limited by the acquisition program and the average frequency over one minute could be calculated afterwards. Typical values ranged from 0.65 to 1 second. For all experiments, each microcolony growth was separately analyzed with Schnitzcells (see paragraphs 2.2.2 and 2.2.3) in order to measure the length, position and displacement of the cells.

2.3.3 Microcolony growth assays

Samples were prepared to have roughly one bacterium in each field of view. Fields were carefully selected to minimize the number of bacteria between the edge of the gel and the field of view, ensuring a proper oxygen supply during the colony growth. On the other hand, bacteria were not chosen directly at the edge of the gel to prevent any mechanical perturbation due to the gel drying. Typically, microcolonies were observed at a distance of 500 μm from the edge.

To analyze cell movements inside the colony, correlation images of the wild-type *E. coli* strain MG1655 growing microcolonies were acquired with the custom microscope (see section 2.1). For each experiment, images were acquired every 3 minutes over 4 fields of view. Acquisition was interrupted when bacteria started to form a second layer on top of the initial monolayer. Afterwards, lineage has been reconstructed for every movie using Schnitzcells (see paragraphs 2.2.2 and 2.2.3) thanks to Maxime Ardré. Experiments that had been previously carried out in the lab with *P. aeruginosa* wild-type strain PAO1 (details in [207]) were analyzed in the same way.

To measure the temporal evolution of morphological properties of different *E. coli* strains (see appendix A), growing microcolonies were imaged with the Leica SP8 microscope (see section 2.1) at 34 and 28 $^\circ$ C [5]. The sample was seeded with two different strains that were spatially separated by the oxygen supply channel (see appendix B.1). Phase images were taken over 10 fields of view (roughly 5 per strains) every 4 minutes. Acquisition was interrupted when bacteria started to form a second layer on top of the initial monolayer. Colony mask were then calculated as described in 2.2.1.

4. When a single cell divides, the two daugther cells soon slide one along the other very quickly compared to the growth dynamics. We refer to this phenomenon as the reorganization.

5. For experiments carried out at 28 $^\circ$ C, the overnight growth also happened at 28 $^\circ$ C.

2.4 Laser ablation

In order to be able to keep the number of bacteria constant in the colony (see paragraph 2.4.2) and/or to disturb its stress balance (see paragraph 2.4.3), we have developed a set-up to perform targeted laser ablations on given bacteria in our sample.

2.4.1 Set-up

Description

The laser ablation set-up was mounted on the Olympus IX81 microscope (see section 2.1). A laser beam was focalized by the objective on the sample and an ablation was triggered whenever a bacterium had to be removed from the sample.

The chosen laser source was a diode-pumped solid state (DPSS) UV laser emitting at 349 nm (Explorer, Spectra Physics). Ablations were performed with a train of impulsions. We controlled the number, the frequency and the energy of the pulses. The energy was set by adjusting the value of the current powering the pumping diode (see calibration in figure 2.11). Typical values for a single cell ablation were 30 pulses with a 1 kHz frequency and a 1.5 A current. The width of the pulses was 6 ns. A 0.6 optical density (NE06A, Thorlabs) was placed in the beam path to lower the range of energies that could be reached with the accessible currents. For the usual settings, the surface density of deposited energy on the sample was 225 $\mu J/\mu m^2$ per pulse, corresponding to a surface power of 37.5 $kW/\mu m^2$.

The laser beam was injected inside a beam expender. A fine tuning of the distance separating the lenses ensured that the beam was parallel. The lenses were chosen in order for the beam to almost fill the rear pupil of the objective[6]. A set of two mirrors was used to inject the laser beam toward the microscope in order to be parallel to the objective optical axis. Internal mirrors inside the microscope lead the beam to the objective. The optical scheme is displayed in figure 2.9.

To position the spot on a bacterium, a movement of stage was triggered either manually (ablations at the 3-cells stage, paragraph 2.4.3) or automatically (ablations at the 2-cells stage, paragraph 2.4.2) via the LabView control program.

6. Having a too large beam would imply reflections on the objective tube.

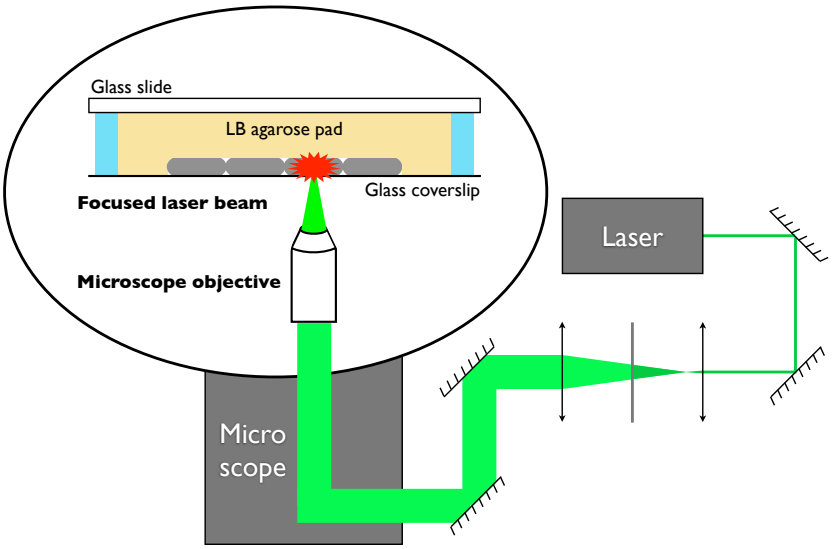

Figure 2.9 – Light path for laser albation.
The laser beam is extended prior to its entrance inside the microscope. Its intensity is lowered by a 0.6 optical density. It is focused by the objective to target a given bacterium in the sample.

Calibrations

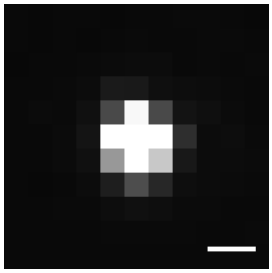

Figure 2.10 – Laser spot. Scale bar is 200 nm.

Performing targeted ablations on single cells required an accurate focalization of the laser beam in the focal plane of the objective. To address the spatial extension of the laser beam, we imaged the spot caused by a beam exiting a fluorescein-coated glass coverslip. The observed spot was 3 pixels wide, corresponding to about 200 nm (see figure 2.10). As required, it turned out to be smaller than the typical *E. coli* width that approximates 1 μm.

For a set of given current values, we checked the stability of the energy per pulse delivered by the laser with time. Systematic measurements displayed in figure 2.11 showed a slight decrease (less than 10 μJ per hour) in energy per pulse during the first hour after we turned the laser on. As it appeared stable (less than 0.1 μJ per hour) over one day after the first hour, we took care to switch on the laser at least one hour before each experiment.

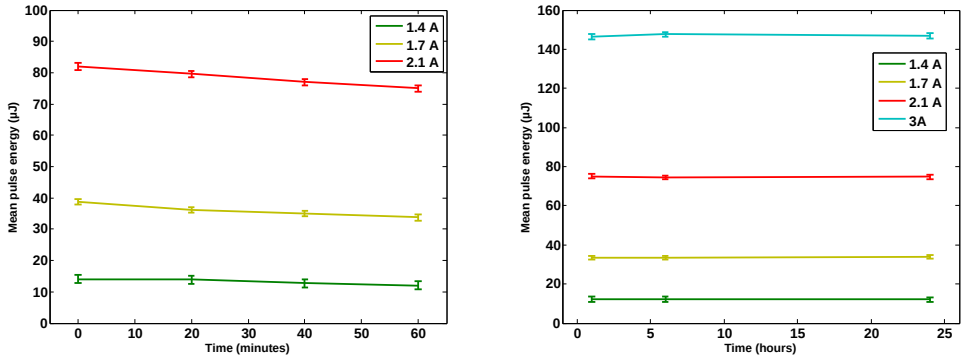

(a) First hour drift in pulse energy.

(b) Day drift in pulse energy.

Figure 2.11 – Pulse energy drift measurements.
For different values of the current controlling the laser, there was a slight decrease of the mean pulse energy with time during the first hour (a) but after that, the value remained stable for one day (b). Fitted drifts (in μJ per hour) for the first hour: -2.16 for 1.4 A, -4.92 for 1.7 A and -7.2 for 2.1 A; for the first day: -0.01 for 1.4 A, $+0.01$ for 1.7 A, -0.002 for 2.1 A and $+0.01$ for 3 A.

2.4.2 Ablation at the 2-cells stage

In order to study individual adhesion properties, we developed an experimental procedure to maintain a bacterium isolated over many generations despite bacterial division.

Experimental procedure Samples were prepared as described in appendix B.1 from an overnight culture (LB, 37 °C, 200 rpm) of the wild-type *E. coli* strain MG1655 diluted 10^4 fold in fresh LB medium. Bacteria grew confined between a glass coverslip and a 1% LB-agarose gel providing nutrients. Acquisitions were performed with the Olympus IX81 microscope (see section 2.1) thermalized at 34 °C. Starting from a field of view with a single cell, the acquisition procedure unfolded as follows for each time step (typically 4 minutes):

1. a correlation image of the field of view was acquired,
2. segmentation was performed on the image to detect the number of present cells (see paragraph 2.2.2),

3. if a division was detected (two cells in the field), an ablation was triggered automatically on one of the daughter cells depending on its spatial position. The daughter cell to be killed was chosen either on a different side of the mother septum at each generation (alternating side ablation experiments) or always on the same side (same side ablation experiments) as described in figure 2.12.

On average, we were able to follow an isolated bacterium over 12 generations, when ablations were performed on one side, and for 8 generations, when ablations were performed on alternating sides. After a large number of ablations, the presence of residues attributed to lysis waste or damaged agarose could mislead the segmentation algorithm into triggering inappropriate ablations [7]. In such cases, we stopped the analysis.

Analysis Each movie was analyzed with Schnitzcells (see paragraphs 2.2.2 and 2.2.3) in order to measure the cell elongation and the position of the center of mass of the bacterium at each generation. The measured displacement of the center of mass was resulting from a real displacement and a displacement of the whole image due to the centering routine that prevented lateral drifts (see section 2.1). In order to get rid of this second component, we used a correlation algorithm to align the whole time stack on a fixed point of the image –the chosen fixed point was typically a dust in the image. With the same method as for asymmetric adhesion assays (see section 2.3.3), we fitted the elongation versus displacement with a linear law. An asymmetry parameter was thus defined by the fitted slope for each generation (see equation 3.1).

2.4.3 Ablation at the 3-cells stage

We inoculated cells (mothers) on an agarose pad at a relatively high density (approximately 10 bacteria in the field of view). Samples were prepared as described in appendix B.1 from an overnight culture (LB, 37 $^\circ$ C, 200 rpm) of the wild-type *E. coli* strain MG1655 diluted 10^3 times in fresh LB medium. Bacteria grew confined between a glass coverslip and a 1% LB-agarose gel providing nutrients. Acquisition was performed over 1 to 4 different locations on the sample with the Olympus IX81 microscope (see section 2.1). Bacterial growth was first recorded at a low frequency (4 minutes between

7. When two cells were detected instead of one, inappropriate ablations were triggered potentially leading to the death of the cell (alternating side experiments) or to an uncontrolled growth (same side experiments).

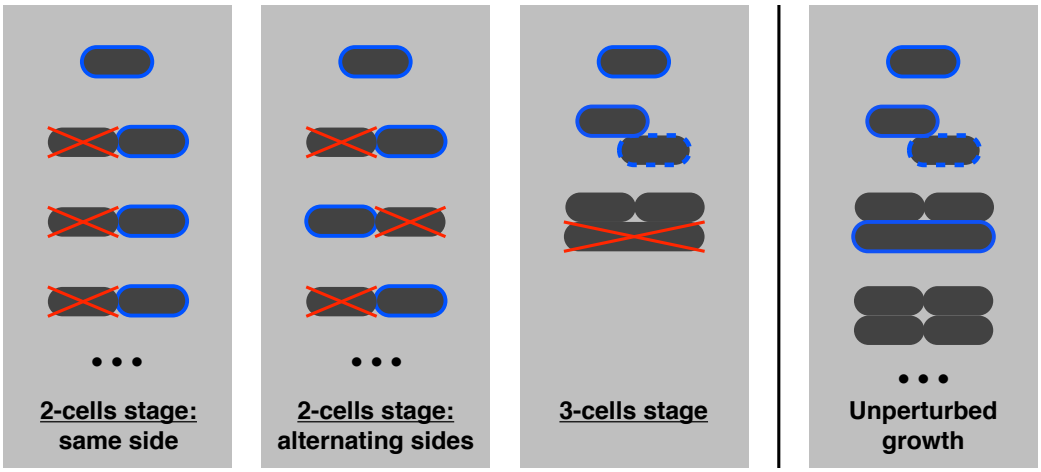

Figure 2.12 – Summary of ablation rules for the different experiments.
The three ablation experiment procedures are displayed to be compared to a regular unperturbed growth (right panel). For each situation, time increases when going down and in between each step, a division event occurred. When displayed, the next cell to divide is circled with a blue solid line. When 2 divisions should theoretically be simultaneous but are slightly desynchronized due to intrinsic noise, the cell with a delayed division is circled with a blue dashed line. The ablated cells are crossed in red.

frames). After the first division, the two daughter cells used to slide along one another. Due to cell variability, one of the daughter cells happened to divide slightly before the other. At the onset of this second division, we monitored the septum formation in the first dividing daughter. Once we estimated this bacteria has fully divided, we manually triggered an ablation of the non-yet-divided other bacterium (see figure 2.12). Most of the time, ablation triggered a reorganization of the two remaining grand-daughter bacteria, similar to the one observed after the first division. Thus, a timelapse of a few minutes after the ablation was recorded with a subsecond time resolution in order to monitor the position, orientation and length of the cells. When no reorganization was observed, we checked that the daughter bacteria has indeed divided by ablating one of the grand-daughter cells to see whether the other one underwent lysis or not. Accurate septation detection and cell length measurements were performed as described in paragraph 2.2.4.

2.5 Traction force microscopy

The traction force microscopy (TFM) technique consists in measuring the forces applied by cells on a deformable substrate. For that purpose, fluorescent tracers are embedded in the substrate during its fabrication. By tracking the movements of the fluorescent tracers, and knowing the mechanical properties of the substrate, one can derive the force field applied on the substrate.

This part of the project was realized in collaboration with Martial Balland from the Motiv team at LIPhy.

2.5.1 Adaptation of the technique to prokaryotic cells study

Principle TFM has initially been developed to study forces transmitted to the substrate during cell migration [212, 213]. Traditionally, substrates used for force measurements are polyacrylamide (PAA) hydrogels, that are transparent and which rigidity can easily be tuned by adjusting the polymer (acrylamide) / cross-linker (bis-acrylamide) ratio [214]. Typical rigidities range from a few to a few tens kPa. Fluorescent beads with a diameter of a few hundreds nanometers are added to the polyacrylamide solution before polymerization. To ease bead detection and force computation, beads have to be located in a plane, close to the surface of the polyacrylamide gel. To achieve this condition, the gel polymerization takes place between two glass coverslips. In such a configuration, electrostatic interactions drive the beads near the glass surfaces. Tuning the concentration of beads and the speed of polymerization through the quantity of catalyzer leads to a substrate with homogeneously distributed fluorescent tracers near its surface (see lower left panel of figure 2.14).

For typical experiments with eukaryotic cells, the polyacrylamide substrate is coated with adhesive proteins such as fibronectin or collagen. Cells spontaneously adhere to these substrates, where they spread out by forming focal adhesions. They are imaged in bright field or phase contrast while the beads are simultaneously imaged in fluorescence. The positions of the beads are compared to a reference image of the relaxed substrate after cells have been washed off. From the difference in position between these two images and, knowing the mechanical properties of the substrate, a stress field can be calculated.

Challenges of the transfer to prokaryotic cells Our goal was to measure the forces at play in a growing bacterial microcolony confined in 2D to get further insight into the morphogenesis of such colonies. Compared to preexisting protocols developed for eukaryotic cells, this involved a number of challenges:

(i) the bacteria we studied are at least 10 times smaller than mammalian cells, and likely to exert much smaller forces on their environment. Moreover, they are mostly rigid rods, but can interact with the substrate via surface appendages (pili, flagellum...). We thus had to adapt the rigidity range in order to observe significant bead displacements: rigidities lower than 7 kPa yield measurable displacements.

(ii) in order to maintain a geometry similar to that of previous experiments and confine the microcolony, we sandwiched the cells between two gels: the PAA substrate for force measurement and an agarose gel containing nutrients. A 2% (w/v) agarose gel[8] assorted with a 4 kPa PAA gel offered a proper confinement for a reasonable amount of time (more than 5 generations for *E. coli* in LB). In this configuration, the beads were slightly defocused by the bacteria as the colony was growing (see scheme 2.13). Thus, the fluorescence image was recorded in a lower plane than the focal plane –the usual shift was 200 nm.

(iii) contrary to eukaryotic cells that are detached with trypsin at the end of an experiment to obtain a stress-free image of the gel, bacteria could not be removed from the substrate in the sandwiched configuration. Thus, we considered that on the first image of a movie, with only one or two bacteria, the gel was close to its relaxed state; we used this image as a reference to measure bead displacements.

(iv) since the bacteria were proliferating during the experiment, we had to take into account the change in area of the colony to calculate forces, as described in paragraph 2.5.3.

(v) the duration of a typical experiment (a few hours) was much longer than the duration of an experiment with eukaryotic cells (a few minutes), so that we had to optimize the stability of the gel over this time range: this involved improving the preparation protocol and adjusting parameters such as the polymerization time (see paragraph 2.5.4).

8. The lower documented rigity for a 1% (w/v) agarose gel is 15 kPa [215, 216]. Given that the rigidity tends to increase rapidly with concentration, a 2% (w/v) will have a higher rigidity.

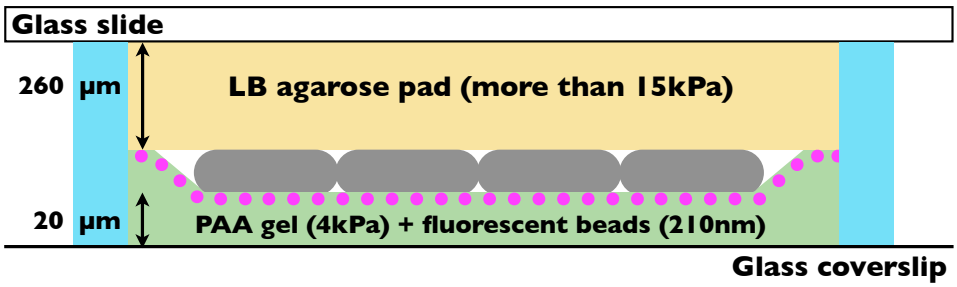

Figure 2.13 – Schematic representation of a TFM sample.
Bacteria are sandwiched between a soft polyacrylamide gel (green) and a stiffer agarose pad (beige). Imaging is done through the lower glass coverslip and the thin polyacrylamide gel. Bacteria locally deform the PAA gel. Relative scales are not realistic and the oxygen supply channel is not represented.

2.5.2 Experimental procedure

Culture conditions Unless mentioned otherwise, force measurements were carried out in non-limiting nutrient conditions. The strain of interest (see appendix A) was grown overnight in LB (37 ° C, 200 rpm), diluted 100 fold in 5 mL of fresh LB and grown again in the same conditions for 2 hours. This solution was diluted 100 to 1000 fold and seeded on a 2% LB-agarose pad. The PAA gel bound to a glass coverslip was deposited and sealed on the seeded agarose (see scheme 2.13). Gel and sample preparation are detailed in appendix B.2. For calibration experiments without bacteria, a LB drop was deposited on the LB-agarose pad instead of the bacterial solution.

For force measurements in low iron conditions, *P. aeruginosa* wild-type strain PA14 was grown overnight in LB (37 ° C, 200 rpm), washed and resuspended at a 100-fold dilution in 5 mL of fresh succinate minimum medium (SMM) [9] for another overnight growth at 28°C, 200 rpm. Two hours prior to sample preparation, the solution was again washed and resuspended at a 100-fold dilution in 5 mL or fresh SMM supplemented with transferrin [10] (Sigma) at 4% (w/v) and $NaHCO_3$ at 0.84% (w/v) to create iron-depleted conditions. The culture was kept shaking (200 rpm) at 28 ° C for 2 hours, diluted 100 to 1000-fold and seeded on a 2% agarose pad prepared in the

9. SMM composition: 6 g/L K_2HPO_4, 3 g/L KH_2PO_4, 1 g/L $[NH4]_2SO_4$, 0.2 g/L $MgSO_4$ $7H_2O$, and 4 g/L sodium succinate, with the pH adjusted to 7.0 by adding NaOH.
10. Transferrin is an iron-binding protein that control the level of free iron in a fluid.

same medium (SMM + transferrin + $NaHCO_3$). The PAA gel was mounted as described for LB experiments.

Acquisition Imaging was performed through the glass coverslip and the PAA gel (see figure 2.13) with the inverted Olympus IX81 microscope (see section 2.1). We recorded the growth of microcolonies started from isolated cells, on 4 to 5 positions of the sample. Every 4 to 5 minute, a phase image of the colony and a fluorescent image of the beads were acquired. Acquisition was stopped when bacteria started to form a second layer.

2.5.3 Tracking of beads and calculation of forces

The exploitation of the data collected by TFM unfolded in two main steps: first, the displacement of each bead was reconstructed in time, then the two-dimensional stress field was calculated. A Matlab routine written by Irene Wang (Motiv team, LIPhy) was adapted for our purpose.

On every image, three zones were defined:
— *the colony zone*, obtained by calculating the binary mask of the colony (see section 2.2.5),
— *the enlarged colony zone* or *zone of influence of the colony*, calculated by dilating (by 50 pixels or 3.2 μm) the mask of the colony in order to include all the stresses due to the colony (see figure 2.14),
— the background of the image, complementary of the enlarged mask.

The tracking of beads took place as follows:

1. Each fluorescent image was aligned with respect to the first one thanks to a subpixel correlation algorithm. The mean intensity of the fluorescence image stack was also normalized.
2. A Particle Image Velocimetry (PIV) algorithm was used on 128 pixels windows in order to find the mean displacement component of the beads in this region, $\overrightarrow{D_{window}}$. The displacement was subtracted to realign the current windows to the same window on the reference image. Under the enlarged colony zone where displacements are expected to be larger, PIV windows were allowed to overlap of 8 pixels to get a better precision on these displacements.
3. A Single Particle Tracking (SPT) algorithm ran on PIV pretreated windows in order to determine the remaining fine displacement component associated with each individual bead, $\overrightarrow{d_{bead}}$. Beads were detected on

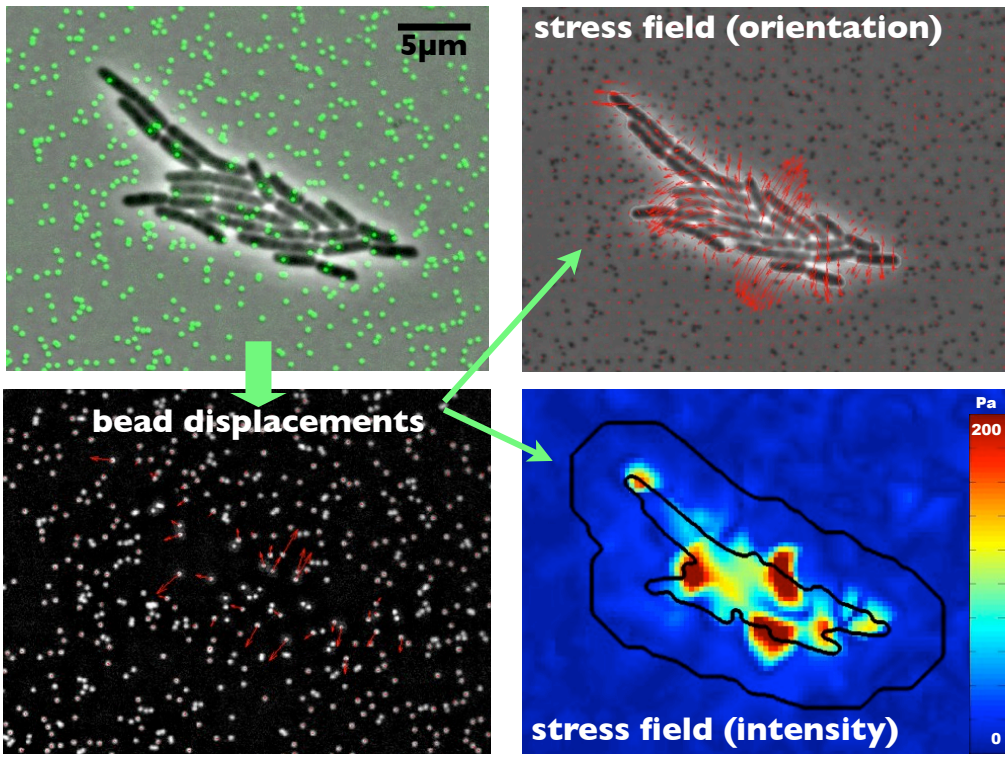

Figure 2.14 – TFM principle.
Displacements of the beads are derived from the fluorescence images (red arrows are amplified 10 times compared to real displacements). From an extrapolated displacement field, a two-dimensional stress field is calculated: orientations are represented in the upper right panel (the size of the arrows is in arbitrary units) and intensities are represented in the lower right panel in Pa. The inner dark line shows the edge of the colony, while the outer one delimits the zone of influence of the colony. A background value of the noise stress is calculated outside of this latter line.

each PIV pretreated window with a subpixel resolution. Each bead in the image n was then associated to the corresponding bead in the image $n+1$.

The final displacement for each bead was calculated as $\overrightarrow{D_{window}} + \overrightarrow{d_{bead}}$. Compared to preexisting analyses, the routine has been modified to only consider beads which were isolated, and thus trackable, all along the movie. This ensured the dynamics of the displacement field was not modified.

Calculation of forces The displacement field $\vec{u}(\vec{r})$ is derived from a stress field $\overrightarrow{T}(\vec{r'})$ with the following formula:

$$\vec{u}(\vec{r}) = \int d\vec{r'}\ \mathbf{K}(\mid \vec{r} - \vec{r'} \mid)\ \overrightarrow{T}(\vec{r'}) \tag{2.1}$$

where $\mathbf{K}$ is the Green's function that depends on the Young's modulus and the Poisson's ratio [11] of the gel. We faced an inverse problem since we aimed at computing stresses $\overrightarrow{T}(\vec{r'})$ by measuring displacements $\vec{u}(\vec{r})$. To overcome this difficulty, the calculation was considered in a two-dimensional Fourier space. Hence, equation 2.1 becomes:

$$\mathrm{TF}[\vec{u}(\vec{r})] = \mathrm{TF}[\mathbf{K}(\mid \vec{r} - \vec{r'} \mid)] \cdot \mathrm{TF}[\overrightarrow{T}(\vec{r'})] \tag{2.2}$$

and is easily transformed in:

$$\overrightarrow{T} = \mathrm{TF}^{-1}[\ \mathrm{TF}[\mathbf{K}]^{-1} \cdot \mathrm{TF}[\vec{u}]\ ]. \tag{2.3}$$

Calculations are detailed in a paper by Butler et al. [217]. However, to obtain a continuous stress field and to calculate numerically the Fourier transform, the displacement field needed to be interpolated on a lattice. Also for numerical reasons, it was necessary to know the value of the continuous mode of the Fourier transform of the stress field which is given by:

$$\mathrm{TF}[\overrightarrow{T}](\vec{k})\ |_{\vec{k}=\vec{0}} = \int d\vec{r}\ \vec{T}(\vec{r}), \tag{2.4}$$

the right hand side being the first moment of the stress field. For eukaryotic cells, which occupied a constant area along the experiment, this quantity was assumed to be zero. However, in the case of a growing microcolony, the sum of stresses under the enlarged colony area had no reason to be null –and turned out not to be. Thus, we calculated the stress field by iterating the value of each component of the continuous Fourier mode with the formula 2.4. The

11. The Poisson's ratio was always taken to be 0.5 assuming the gel was incompressible.

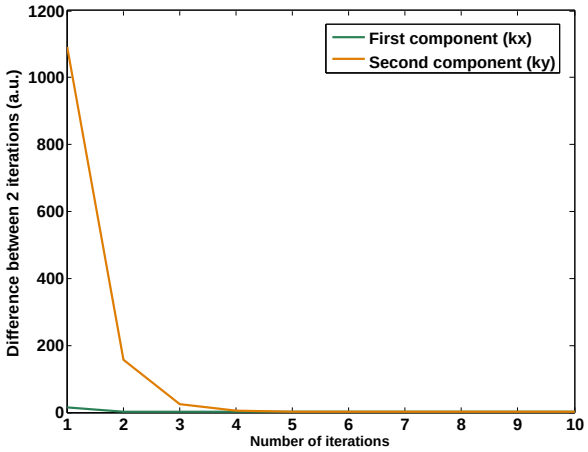

Figure 2.15 – Representative example of the convergence of the continuous mode of the stress field for the two components of the Fourier space.

figure 2.15 shows that a total of less than 5 iterations lead to a stable value for both components. All the analyses were performed with this method. A regularization parameter was used to take into account the spreading of the displacements due to a punctual stress, we kept this parameter at the small value $\lambda = 10^{-9}$. Finally, since stresses were calculated over surface elements of 511 nm×511 nm, the stress field could convert into a local force field.

2.5.4 Calibration of the gel stability

During preliminary experiments, we observed spontaneous sudden beads displacements far from the colony. In order to reduce the probability of such movements, we modified the protocol used for eukaryotic cell: (i) we increased the polymerization time of our gel from 45 minutes to 1.5 hour, (ii) after polymerization, gels were rinsed successively in two sterile filtered water baths for one hour each to wash away any free bead [12]. Spontaneous bead movements seemed less frequent but were still observed (see figure 2.16 for an example). To check the integrity of the gels over time, we carried out long-term experiments without cells in order to measure the evolution of the position of the beads in the absence of external stress. This allowed us to calibrate the precision of our force measurements.

12. This rinsing step was also performed to dilute any toxic component likely to disturb the bacterial growth.

Most of the beads experienced displacements smaller than half a pixel [13] (see figures 2.17a and 2.17d), corresponding to less than 35 nm. These displacements are not significant when compared to displacements induced by bacteria, which typically ranged between 3 and 6 pixels. From these displacements, we estimated the noise on our force measurements. On average over 12 experiments, the mean force measured on the gel was 1.5 ± 0.7 pN.

Additionally, isolated beads could occasionally exhibit step displacements of a few pixels (see figure 2.17b). The new position of the bead appeared stable and very few beads experienced such a displacement over a field of view (between 0 and 5 over an average of around 1 300 beads per field of view). In any case, over more than 15 000 analyzed beads, none experienced a displacement greater than 4 pixels, corresponding to 280 nm. We calibrated the contribution of these displacements to the force distribution. The maximal local forces we measured were on average 9.6 ± 5.9 pN over our calibration experiments, with a maximum of 23.5 pN. In both cases, it is smaller than typical maximal forces measured inside bacterial colonies (around 85 pN for *E. coli* and 30 pN for *P. aeruginosa*). Furthermore, being constant in time, such contributions are easy to detect.

Finally, both the probability to observe such displacements (see figure 2.17c) and the level of noise increased with time (see figure 2.17d). A possible degradation of the gel as well as a time integration of slight imprecisions in the beads detection could account for this latter phenomenon. In order to measure such effects during forces measurements with bacteria, we calculated the average and maximal forces outside the colony. This allowed us to detect any possible defaults in our fabrication process [14], assess the quality of our gel, and thus to exclude potentially invalid experiments.

13. Detection of beads is achieved with a subpixel resolution (see paragraph 2.5.3).

14. For instance, trouble in the conservation of APS could lead to unusual global movements of the beads that were easily detected by our analysis.

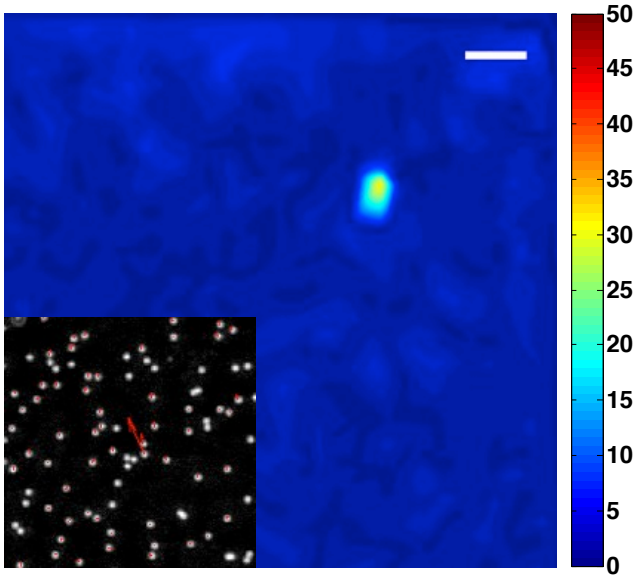

Figure 2.16 – Example of sudden bead displacement.
Force map calculated from a experiment without bacteria. Scale bar is 5 μm and colors represent forces in pN. The high force patch corresponds to a sudden displacement of 246 nm (arbitrary units on the figure), displayed with a red arrow on the fluorescent image of beads in this region (lower left corner).

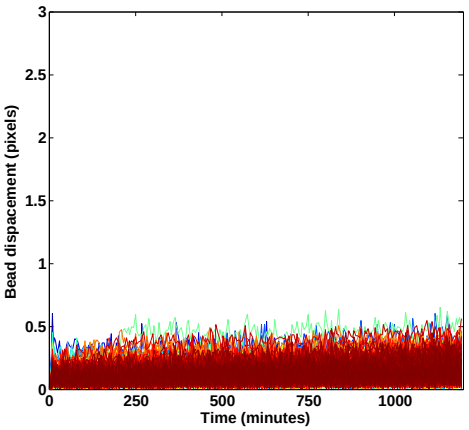

(a) Example with no sudden displacement.

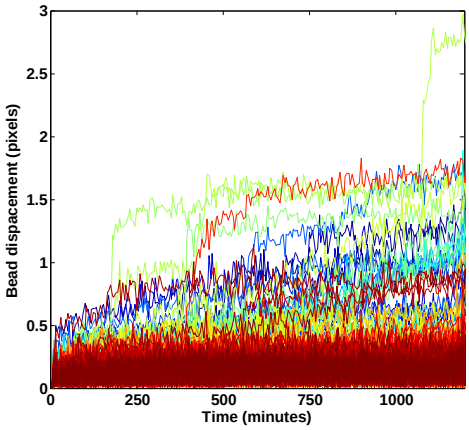

(b) Example with sudden displacements.

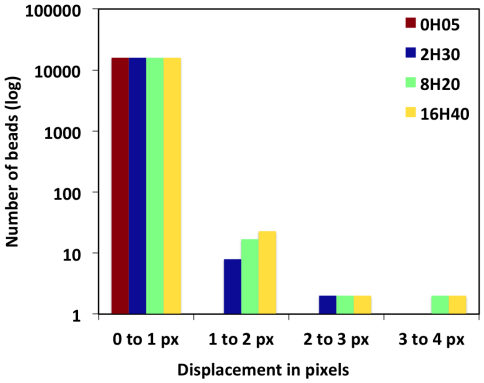

(c) Histogram (counts in log scale) of the displacements sizes depending on time.

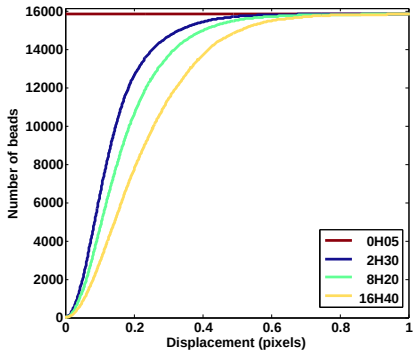

(d) Cumulative distribution of the displacements depending on time.

Figure 2.17 – Calibration of bead displacements in the absence of stress. Examples of the temporal evolution of bead displacements with respect to the reference image. (a) and (b) represents all the beads in a field of view followed over 16 hours and 40 minutes for two different acquisitions. Most of the beads do not move more than half a pixel whereas a few of them experience sudden displacements of a few pixels. (c) and (d) describe the evolution of the distribution of displacements over 12 experiments for a total of 15857 beads detected. 2H30 and 8H20 correspond to typical durations of experiments in respectively a non-limiting and an iron-depleted medium. A pixel corresponds to 63.9 nm.

Chapter 3

Results and interpretation

3.1 One and two cells stage

3.1.1 Asymmetric adhesion

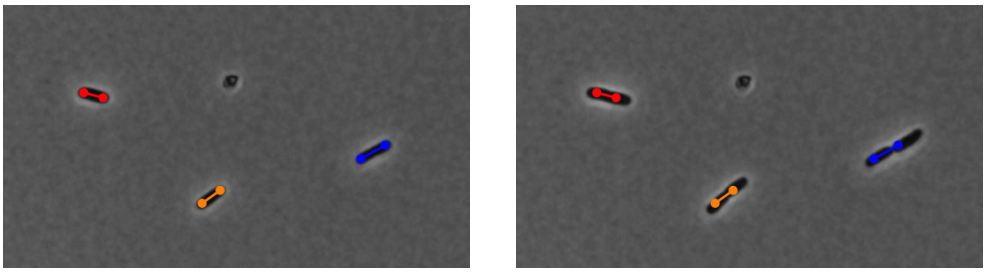

(a) First image. (b) After a few minutes of growth.

Figure 3.1 – The colored dumb-bells on the initial image stand for position of cells before growth. After a few minutes of growth, bacteria appear to have elongated asymmetrically compared to their initial position. All the images were recentered to correct for potential drifts on a fixed feature (here on the small particle).

Apparently asymmetric elongation

Despite the fact that cell wall insertion is known to be homogeneous (see paragraph 1.2.1), we noticed that isolated bacteria confined between agarose and glass appeared to grow asymmetrically (see figure 3.1). To quantify this phenomenon, we analyzed systematically the displacement of the center of mass of cells. For that purpose, we defined the asymmetry parameter A as the slope of the displacement of the center of mass $\Delta\overrightarrow{X_{CDM}}(t)$, projected over the initial orientation of the cell $\overrightarrow{c_{\parallel}}$ (oriented from the old pole to the

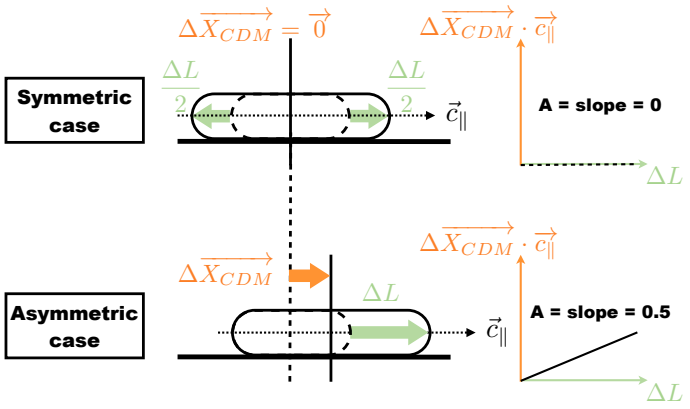

Figure 3.2 – Schematic definition of the asymmetry parameter A.
Two extreme cases are displayed.
Lower panel: the cell appears to elongate in a totally asymmetric fashion. Its center of mass moves of half its elongation ΔL. The asymmetry parameter, defined as the slope of the projected displacement of the center of mass with respect to the elongation (see equation 3.1), is A $= 0.5$.
Upper panel: the cell appears to elongate in a perfectly symmetric fashion. Its center of mass is not moving despite its elongation and A $= 0$.

new pole), as a function of the elongation $\Delta L(t)$ of the cell (see figure 3.2):

$$\Delta\overrightarrow{X_{CDM}}(t) \cdot \overrightarrow{c_\parallel} = A \cdot \Delta L(t). \tag{3.1}$$

Since we did not know the history of the poles when bacteria had just been deposited on the gel, the orientation of $\overrightarrow{c_\parallel}$ was chosen at random. Our observable was thus the absolute value of A, defined as $\left|\Delta\overrightarrow{X_{CDM}}(t) \cdot \overrightarrow{c_\parallel}\right| = |A| \cdot \Delta L(t)$. The quantity $|A|$ is expected to vary from 0 for a perfectly symmetric apparent elongation, to 0.5 for a fully asymmetric apparent elongation (see figure 3.2). The distribution of $|A|$ is displayed in figure 3.3a for the *E. coli* wild-type strain. Interestingly, when looking at a large number of cells, values of the asymmetry parameter were broadly distributed. We fitted the cumulative distribution of $|A|$ as a folded normal cumulative distribution (see the inset in figure 3.3a) in order to retrieve the mean value and standard deviation without the bias of the absolute value. For the wild-type, the mean value of the asymmetry was 0.126 and the standard deviation 0.117, indicating that cells could display an apparently asymmetric elongation.

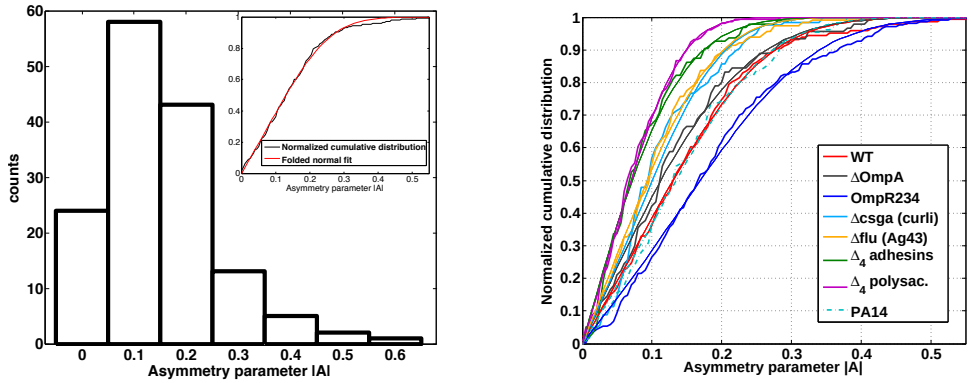

(a) Histogram of asymmetries for the wild-type *E. coli* strain (WT, N=146).

(b) Normalized cumulative distributions of asymmetries.

Figure 3.3 – Comparison of the asymmetry distributions for different mutant *E. coli* strains and the *P. aeruginosa* wild-type strain. (a) The inset represents the normalized cumulative distribution (black) and the fitted folded normal distribution (red), R^2=0.99. (b) Normalized distributions for different mutants, fits are plotted in the same color.

Strain	N	A(25%)	A(50%)	A(75%)	%(0.25)	Mean	Std
WT	146	0.08	0.15	0.23	21	0.126	0.117
ompA	90	0.06	0.11	0.19	13	0.093	0.131
ompR234	204	0.10	0.17	0.25	56	0.167	0.135
ΔcsgA	125	0.07	0.10	0.14	6	0.099	0.083
Δflu	116	0.05	0.10	0.14	6	0.089	0.089
Δ_4 adhesins	95	0.04	0.07	0.12	2	0.004	0.106
Δ_4 polysac.	159	0.04	0.07	0.11	0	0.067	0.067
PA14	129	0.08	0.13	0.20	17	0.133	0.110

Table 3.1 – Summary of the asymmetric adhesion assay.
The analyzed strains are listed here. All *E. coli* mutants were derived from UGB52. PA14 is a *P. aeruginosa* wild-type strain. N is the number of cells in the distribution. A(25%), A(50%) and A(75%) respectively represents the maximal asymmetry of the first quarter, the half and 3 first quarters of the distribution. %(0.25) indicates the percentage of cells that displayed an asymmetry greater than 0.25. Mean and std correspond to the mean and standard deviation of the fitted distribution ($R^2 > 0.98$ for all strains).

This result was surprising for two reasons. First, the geometry is *a priori* symmetric since the confinement due to the gel has not reason to be unbalanced with respect to the center of mass of the bacterium. Second, *E. coli* cells elongate by patchy, yet homogeneous, new peptidoglycan insertion over the cell length (see paragraph 1.2.1), excluding the possibility of a directional elongation. However, beside confinement, adhesion forces could also be at play in this situation. Indeed, an asymmetric repartition of adhesive bonds along the cell could break the symmetry of the force balance.

Link with adhesion

To test whether adhesins played a role in the apparent asymmetry in elongation, we used genetically modified strains, lacking or over-expressing known adhesins (see paragraph 1.3.2). For each strain, we analyzed a large number of cells and plotted the normalized cumulative distributions of their asymmetry parameters (see figure 3.3b). As described for the wild-type, we fitted the distribution by a folded normal distribution (see figure 3.3b and results in table 3.1). For the strain over-expressing curli fibers (OmpR234), the mean value of the asymmetry was significantly increased compared to the wild-type ($<|A|>_{OmpR234}$=0.167), indicating that more cells grew asymmetrically. On the other hand, for adhesins knock-outs, the mean value was reduced. In particular, for the antigen 43 and the quadruple polysaccharides knock-outs mutants, the mean value was close to the standard deviation of the fitted distribution, suggesting that the asymmetry effect was not pronounced. Moreover, for the quadruple knock-out of curli fibers, antigen 43, type I fimbriae and flagellum, almost no asymmetry was observed ($<|A|>_{\Delta_4 adhesins}$=0.004). These results confirmed that the apparent asymmetry in elongation depends on the presence of surface proteins involved in adhesion. Moreover, several adhesins seem to be implicated in this asymmetric adhesion process, with some redundancy in their function. Additionally, a quadruple polysaccharide knock-out also displayed a reduced apparent asymmetry in elongation. Finally, we analyzed the asymmetry distribution of a knock-out mutant of the outer membrane protein OmpA, which is not known to be involved in adhesion. The composition of the outer membrane of this strain is different from the wild-type [218]. The mean value of the asymmetry parameter was also reduced. However, a larger proportion of cells displayed highly asymmetric behaviors (A>0.25) compared to when adhesins are removed. Taken together, these findings support the idea that the repartition of adhesive bonds is asymmetric for a significant proportion of cells. More-

over, this trend is not specific to *E. coli*: we also observed asymmetrically elongating cells for *P. aeruginosa* (see figure 3.3b and table 3.1).

Discussion

An uniformly adhered cell may have trouble elongating. Now considering that a single adhesin is bound, if the bond strength is large enough, the bacterium will appear to elongate "around" this fixed point. If there were more than one bond, the cell would elongate "around" the tightest one. Of course, this picture could be dynamic as bonds are created and ruptured. This could be the case for bacteria with an asymmetry parameter close to 0, since our analysis would not discriminate such a case from a non-adhesive cell elongating symmetrically. Yet, the fact that some cells have larger asymmetry parameters supports the idea that a focal adhesion could be conserved during the cell cycle.

An asymmetry in bond repartition could arise at different levels:

(i) either the efficiency of binding (k_{on}) is dependent on the position along the cell in an asymmetric fashion,

(ii) or, the spatial repartition of adhesins (n_{adhesin}) along the cell is itself asymmetric.

Formulated in terms of probabilities, the probability to form a bond p_{bond} at a particular position l along the cell could be written as:

$$p_{\text{bond}}(l) = n_{\text{adhesin}}(l) \cdot k_{\text{on}}(l), \tag{3.2}$$

where $n_{\text{adhesin}}(l)$ is the density of adhesins at the position l and $k_{\text{on}}(l)$, the probability of one adhesin to bind the surface. Hypothesis (i) would consist in $k_{\text{on}}(l)$ being asymmetric while hypothesis (ii) would correspond to $n_{\text{adhesin}}(l)$ being asymmetric. With either or both hypotheses verified, the result would be an apparent asymmetric elongation like we measured in our experiments.

To check the validity of an asymmetry in efficiency of binding (hypothesis (i)), we analyzed how such a phenomenon could arise and what would be the consequences on the asymmetry distribution. Assuming $n_{\text{adhesin}}(l)$ uniform, the existence of a focal adhesion conserved through the cell cycle would directly support hypthesis (i). Indeed, if a specific zone over the cell length is moving less, it may be easier for adhesins in this zone to bind the surface. Consequently, $k_{\text{on}}(l)$ will no more be uniform. For this argument to be valid, a focal adhesion has to be formed in the first place. A focal adhesion could form even with an initially uniform efficiency of binding. For instance, if the

binding of an adhesin is stochastic (diffusion to find the surface for instance), not all adhesins will be expected to bind at the same time [1]. Depending on binding and unbinding rates, a focal adhesion would form in the place of the first strong enough bond. Such a simple picture would lead to a uniform probability of apparition of the focal adhesion along the cell axis. Thus, a uniform distribution of the asymmetry parameter would be expected. Since it is not the case (see figure 3.3), either the dynamics of establishment of a focus is more complex, or the initial probability to create a bond is not uniform. In particular, the latter could occur if the adhesin repartition was not uniform along the surface (ii).

Small variations in the distance between the cell envelop and the substrate, d, could also account for a modulation of the efficiency of binding with the position along the cell (hypothesis (i)): $k_{\text{on}}(d(l))$. We probed the planarity of the cells in our confined configuration using Reflection Interference Contrast Microscopy (RICM). It appeared that bacteria were flat (angle smaller than 1.2 degrees) with respect to the glass plane, when the colony counted less than 10 cells (see observations in appendix D.2). These observations were only preliminary and would need to be confirmed by more experiments. Yet, it suggests that the variations in distance from the substrate were smaller than 120 nm between the two cell poles. Thus, the eventuality of a longitudinal modulation of k_{on} due to distance variations between the cell and the substrate is unlikely.

Given the previous considerations, hypothesis (i) is not likely to account for the observed asymmetry. Let us now consider the hypothesis of a non-uniform adhesin repartition (ii). Hypothesis (ii) is supported by the fact that peptidoglycans are not renewed at the poles (see paragraph 1.2.1). Indeed, assuming an homogeneous insertion of adhesins along the cell, poles would count more adhesins at the end of a cell cycle, since they would not get "diluted" by elongation. After division, the newly formed pole would count few or no adhesins compared to the preexisting one, which would have accumulated adhesins during the previous cycle. Such a simple mechanism could explain the asymmetry. In that case, one would expect the asymmetry to be correlated with the age of bacteria. Indeed, the age of a bacterium corresponds to the age of its oldest pole (see paragraph 2.2.3 and figure 2.4), and thus represents the number of generations this mechanism could have been at play to build up the asymmetry. This could also explain the variability in asymmetry parameter observed in a population of cells. Alternatively, het-

1. $k_{\text{on}}(l, t = 0)$ uniform, but soon $k_{\text{on}}(l_0) > k_{\text{on}}(l \neq l_0)$ with l_0 position of the focal adhesion.

erogeneities of the level of expression adhesins at the scale of the population could also lead to a distributed asymmetry parameter. Finally, an active process to establish an asymmetry in adhesin repartition (i) is not to exclude either, but to our knowledge, has never been reported for the considered adhesins.

To test if the asymmetry was linked to the age of bacteria, we probed the evolution of the asymmetry on dividing, thus aging, bacteria maintained isolated via laser ablation (see paragraph 3.1.2).

3.1.2 Adhesion dynamics of pre-existing poles

In order to assess whether there was a systematic bias of the asymmetry towards one pole (new/pre-existing), we maintained a cell isolated for more than one generation. The goal was to know the history of the poles (new/pre-existing), while being able to monitor the age of the cell (see paragraph 2.2.3 and figure 2.4).

Age control via laser ablation

To achieve this, we started from a single cell and performed a laser ablation of one of the daughters after each division (see paragraph 2.4.2). Ablations could be performed always on the same side of the remaining cell. In this configuration, age increased at each generation. Ablations could also be performed on alternating sides at each division in order to maintain the cell at age 1. In both cases, we checked if the repeated ablations affected the viability of the remaining cell by assessing its growth rate over time (see figure 3.4). Under 10 generations, the growth rate remained constant independently of the side of ablation. For same side ablations, the growth rate always showed a steady decrease after exposure to 10 ablations. For further analysis, we considered only data obtained for the 10 first generations.

For each generation, we calculated the asymmetry parameter of the remaining cell. Past the first ablation, we knew which pole had just been formed by division. Hence, we systematically orientated the cell axis vector, $\overrightarrow{c_{\parallel}}$, from the old pole to the newly formed one in the definition of the asymmetry parameter (see equation 3.1 and figure 3.2). This oriented asymmetry parameter A could range from -0.5 (new pole totally immobile) to 0.5 (old pole immobile), with 0 still corresponding to a symmetric apparent elongation (center of mass immobile).

Old pole more anchored

For the first generation, we measured the absolute value of the asymmetry parameter $|A|$ since we ignored the orientation of $\overrightarrow{c_{\parallel}}$ (see paragraph 3.1.1). The values were consistent with the distribution of asymmetries observed for a large number of cells (see figure 3.3a). For the following generations, the oriented asymmetry parameter turned out to always be positive (see figure 3.5), for all experiments and independently of the number of ablations performed. Moreover, the value was usually greater than 0.25, corresponding to strong asymmetries. This indicated that the preexisting pole was always more anchored than the one just formed by division. These observations support the idea that adhesion asymmetry could arise from a constitutive asymmetry in adhesin repartition at the surface of the cell (cf. hypothesis (ii) in the discussion part of paragraph 3.1.1).

Technical limitations

Given our experimental protocol, artifacts could influence measurements and have to be kept in mind.

First, for same side ablation experiments, the two sides of the bacterium after ablation were not necessarily identical since one was previously occupied by the ablated cell. Indeed, the agarose gel could be easier to deformed on that side, soften by the ablation or still deformed by potential residues. Moreover, the ablated cell could have left molecules that acted as an attractant for the remaining cell. Alternating side ablation experiments were a control for these potential effects: as soon as two ablations had been performed, the two sides were symmetric regarding the previous considerations. Thus, if the systematic bias for a less motile preexisting pole was only due to surface or gel artifacts, this effect would be reduced for the alternating side ablations, which is not the case (see figure 3.5).

Second, despite ablations, there was a short moment where the cell was not isolated. Depending on the delay between septation and ablation [2], the two cells may have had enough time to slide along one another (phenomenon described in paragraph 3.1.3). This could perturb the adhesions establishment.

2. This delay depends on the synchrony between septation completion and septation detection (followed by ablation), which is limited by the acquisition rate, typically 4 minutes.

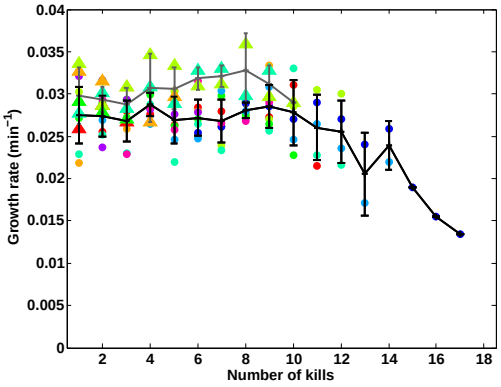

Figure 3.4 – The growth rate is not affected by the number of kills under 10 ablations. Disks represent same side ablations (N=9 experiments) and triangles alternating side ablations (N=5). Experiments are displayed in different colors and the solid lines represent the average of same side ablations (black) and alternating side ablations (gray). Error bars are standard deviations.

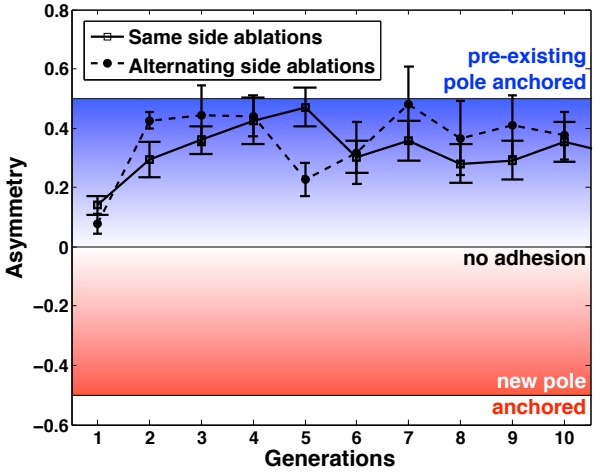

Figure 3.5 – Oriented asymmetry parameter at each generation during the single cell ablation experiments. If the asymmetry is positive/negative (blue/red area), the preexisting/newly formed pole is more anchored to the substrate. If it is 0, there is either no anchoring or a symmetric anchoring. Results are displayed for same side ablation experiments (squares and full line, N=9) and for alternating side ablation experiments (disks and dashed line, N=5). Error bars represent the standard errors. Both experiments indicated a preferential anchorage of the preexisting pole to the substrate.

Maturation dynamics

Despite these limitations, given the control of alternating ablations and the reproducibility of our results, we are confident that ablation experiments provide information about the dynamics of the establishment of the asymmetric adhesion.

In experiments where ablation was always performed on the same side, the preexisting pole grew older at each ablation. The asymmetry appeared to increase with age, reaching values close to 0.5 at the 4^{th} and 5^{th} generation. This suggests that the asymmetry in adhesion could mature over generations to achieve a full asymmetry after roughly 5 cycles. On the other hand, with alternating side ablations, the preexisting pole was always only one generation older than the newly formed one. Yet, the asymmetry already reached high values (A>0.4) at the 2^{nd} generation, suggesting, on the contrary, that the asymmetry in adhesion could establish in less than one generation. We believe that the sliding of bacteria along one another may result in underestimating some asymmetry parameters. This sliding was observed more frequently for same side ablations than for alternating sides ablations. This may be explained by a slight improvement of the experimental protocol between the two series of experiments. In conclusion, when unperturbed, the asymmetry in adhesion seemed to establish in less than one generation for a certain fraction of cells. Moreover, if this asymmetry was induced by an asymmetric repartition of adhesins, it could mean that this asymmetry did not exist in liquid culture (few adhesins and/or few asymmetry in repartition), but was induced upon attachment to a surface. Such switch would take place in less than one generation.

3.1.3 Buckling following the first division

The transition from a line of growing bacteria to a two-dimensional microcolony occurs very early in the colony development. In fact, the unidimensional growth is limited to a single bacterium. A few minutes after the first division, the two daughter bacteria slide along one another, initiating the two-dimensional growth process (see figure 3.6). The following study analyzes the origin of such a reorganization.

In terms of gel deformation, a configuration where the two daughter cells are side-by-side is energetically more favorable than an in-line configuration. Indeed, in two dimensions, the energy cost to deform the gel is proportional to the perimeter of the deforming object (line tension). For both cases, the perimeter can be estimated with l_{cell} and w_{cell}, the length and width of a cell

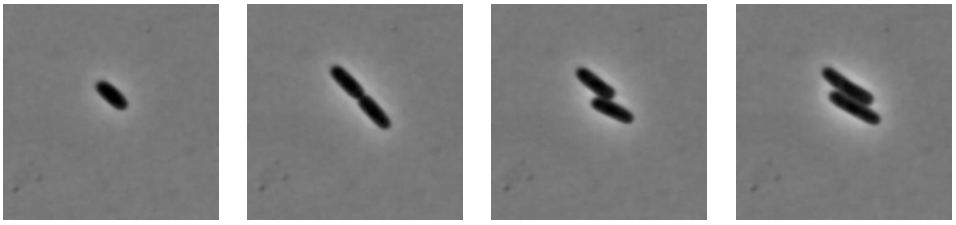

Figure 3.6 – Initial steps of colony formation: the transition from a linear growth to a planar growth occurs very early. Images width is about 20 μm.

that are considered to be equal for the two daughters:

$$\begin{cases} P_{\text{side-by-side}} = 2 \cdot (l_{\text{cell}} + w_{\text{cell}}) \\ P_{\text{in-line}} = 4 \cdot l_{\text{cell}} + 2 \cdot w_{\text{cell}} \end{cases} \Rightarrow P_{\text{side-by-side}} < P_{\text{in-line}}, \tag{3.3}$$

which provides that the side-by-side configuration is energetically more favorable. Yet, elastic deformation is not necessarily the process that drives the transition from one state to the other. In particular, the in-line configuration could be metastable (necessity to deform the gel even more to go from the in-line to the side-by-side configuration).

Our previous findings suggest an alternative scenario to explain the observed transition. As we have discussed in the first part of this section, our results show that, first, an individual cell is likely to anchor its pre-existing pole rather than its new pole, and second, this asymmetry can establish in less than one generation (see paragraphs 3.1.1 and 3.1.2). What does this finding imply for the next step in colony development? Right after division, the two daughter cells are facing each other with their old poles located at the extremities of the line they form (indicated by blue stars in the upper left panel of figure 3.7). Soon, these poles anchor and the cells attempt to elongate toward one another. This elongation may build up stress in the polar adhesions (red arrows in the upper left panel of figure 3.7) and result in a buckling instability. We claim that the observed reorganization may be due to the relaxation of this accumulated stress. This would be consistent with a previous study showing that the nature of the gel can influence the occurrence of the reorganization [219]. In the following, we propose two ways to test whether reorganization could derive from the relaxation of accumulated stress.

Correlation between the asymmetry of the mother cell and the reorganization of the daughters

In order to probe the reorganization dynamics with a good time resolution, we performed rapid acquisition of the initial steps of the colony formation (until the division of one of the two first daughter bacteria, see paragraph 2.3.2). Our observable was the distance between the centers of mass of the two daughter bacteria (see the right panel of figure 3.7). This quantity steadily increased at first, as cells elongated facing each other, then suddenly dropped, which is the signature of the reorganization. The reorganization dynamics varied both in terms of distance drop and rapidity. We checked if this variability could be better explained by one of the two proposed scenarios (gel-induced or adhesion-driven reorganization).

First, in order to correlate this reorganization to adhesion features, we color-coded our data depending on the asymmetry A of the mother cell (see definition is equation 3.1). For the reorganization to be driven by asymmetric adhesion forces, two adhesion gradients had to establish (one for each daughter). If the mother cell grew very asymmetrically, it meant that one of these two gradients already established. As expected, we observed a correlation between a sudden reorganization (important drop in a short time) and a high mother asymmetry parameter, suggesting that adhesion drives the reorganization process (see curves on the top right panel of figure 3.7).

Second, to test whether the reorganization could be induced by a relaxation of the elastic deformation of the gel, we tried to correlate the variability in the reorganization dynamics with an elasticity-related parameter. A naive approach can be to model the gel compression by two springs near the extremity of the line of bacteria (see lower left panel of figure 3.7). Since the springs have the same axis as the bacteria, the loaded stress is proportional to $l_{max} - l_0$, the difference between the line length before reorganization l_{max} and the initial line length l_0. We color-coded the reorganization curves, but this time with the $l_{max} - l_0$ difference this time (see curves on the lower right panel of figure 3.7). This showed no apparent correlation, suggesting that the gel confinement is not the major driving force for reorganization. An even more direct proof could be provided by varying the agarose rigidity.

In conclusion, adhesion seems to contribute more to the reorganization process than the gel elasticity. Given the energetic considerations (see equations 3.3), a potential energy barrier has to prevent the reorganization long enough for the stress to load. An incomplete septation could account for

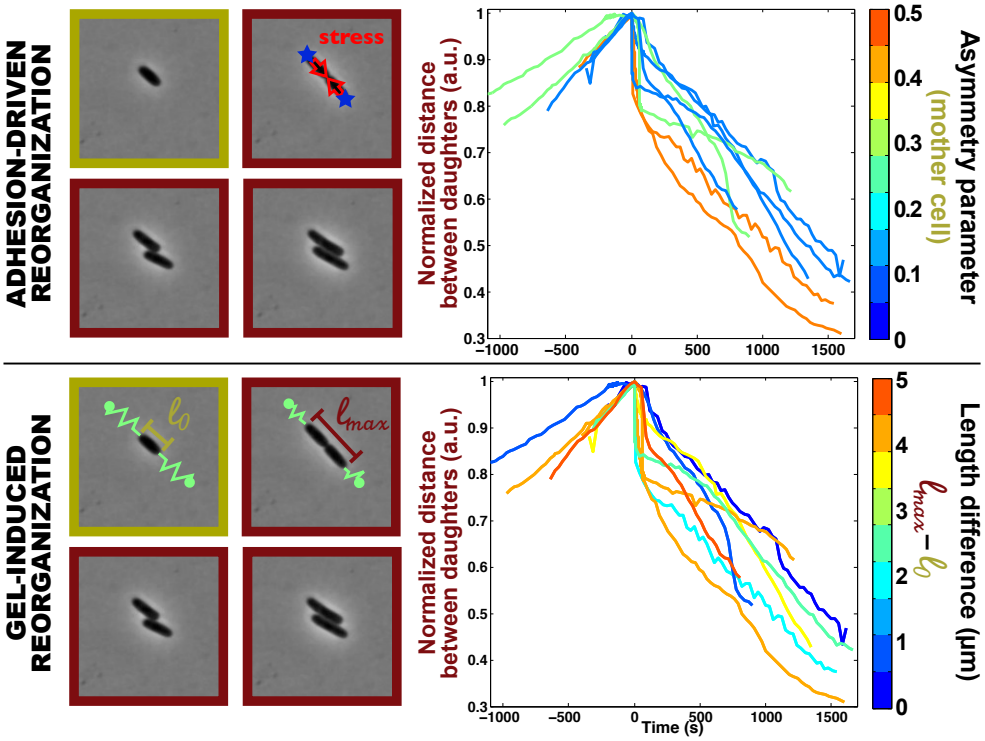

Figure 3.7 – Two hypotheses are analyzed to explain the reorganization: an adhesion-driven mechanism (upper panel) and a gel-induced mechanism (lower panel). For both cases, the normalized distance between the 2 daughter cells depending on time is displayed for all experiments. For each of the 7 experiments, the corresponding curve is color-coded depending on the asymmetry parameter of the mother cell (upper panel) or depending on the cell extension $l_{max} - l_0$, l_0 being the length of the initial cell and l_{max} the sum of the lengths of the daughter cells just before reorganization (lengths displayed on the left lower panel).

this effect. In particular, few is known about how the septum finally resolve. Cells could start to elongate, thus load stress, and still be linked together by a non fully resolved septum preventing the reorganization. In such picture, mechanical stress could be considered as a potential mechanism for septum completion. Additionally, as mentioned earlier, the in-line configuration could also be metastable from the point of view of gel deformation.

Reorganization triggered upon ablation

A configuration similar to the one preceding the reorganization (two cells in line) occurs later in the growth process. With the first reorganization, bacteria slide one along another. They keep growing and, at some point, one of the two cells usually divide slightly before the other. This results in a short time window during which there are three cells. In this configuration, the two short cells are in line and the third long one is preventing any reorganization from occurring [3] (see the upper image of figure 3.8). Removing this obstacle by laser ablation (see paragraph 2.4.3), and analyzing the reorganization that sometimes followed, gave us hints about the origin of the reorganization.

We performed triggered ablations at this 3-cells stage for around 50 microcolonies. Our initial goal was the measure cell lengths before and after reorganization, more details are provided in appendix D.1. While performing these experiments, we noticed two things that tend to support the hypothesis of an adhesion-driven reorganization. First, reorganization did not occur systematically after ablation of the obstacle cell. Instead, it seemed more likely to happen if the two cells had divided for a longer time. Unfortunately, we did not have access to the precise time of division. A proper quantification of this observation would require additional experiments. Yet, this observation was consistent with the idea that a delay is required after division for the elongation-induced instability to build-up. Second, V-shape configurations (see the lower middle image of figure 3.8) were sometimes observed after ablation. We checked if the two short cells were indeed separated by ablating one of them. Since it did not affect the other cell, we concluded that cytoplasms were separated. The occurrence of such configurations could be explained by a non-fully resolved septum as mentioned earlier.

3. Note that a reorganization on the external side of the microcolony has never been observed consistently with the idea that it may be prevented either by the cell-cell interaction or by the lateral confinement due to the gel.

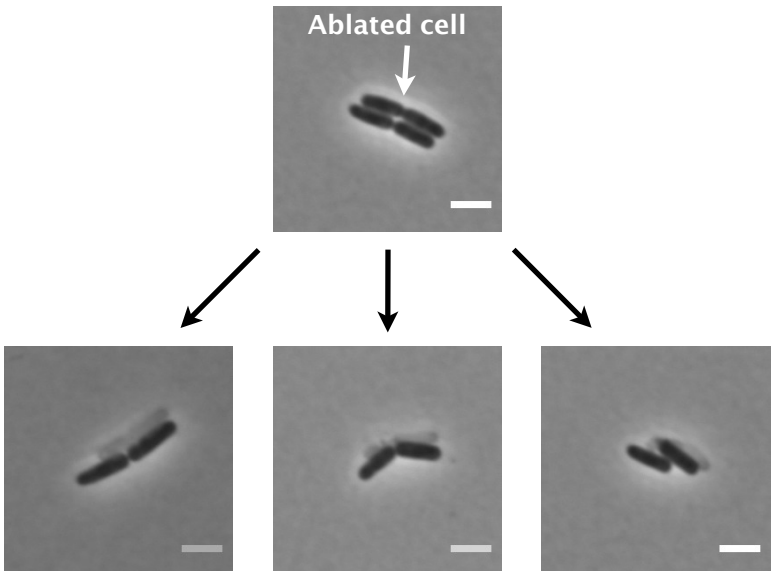

Figure 3.8 – Principle of the reorganization triggered upon ablation.
The upper image shows in which configuration the ablation is performed. The three lower images correspond to the configurations observed after ablation: reorganization (right), V-shape (center) and no reorganization (left). Scale bar is 3 μm on every image.

3.2 Single-cell dynamics and microcolony organization during planar growth

In this section, we analyze the characteristics of growing microcolonies with a single-cell resolution, for both *E. coli* and *P. aeruginosa* (see paragraph 2.3.3). Dimensions and growth rate of these strains were quantified in appendix C.

3.2.1 Centrifugal displacements driven by uniform growth within the colony

Cell position depending on cell age

After the first reorganization (two cells stage, see paragraph 3.1.3), the more anchored old poles were at the periphery of the microcolony. To see whether this trend would persist, we followed the position of the two first daughter cells within the colony. Interestingly, the eldest cells remained always located at the periphery of the microcolony (see figures 3.9a and b). When we measured the distance of the eldest cell with respect to the colony border, it always appeared comparable to the cell width (see figure 3.9c). This suggests that the eldest bacteria (the ones who inheriting the initial poles) are pushed away as the colony grows. To test this hypothesis, we analyzed on the one hand, the spatial distribution of individual growth rates inside the colony, and, on the other hand, the displacements of cells.

Radial pushing

The growth rate of individual cells did not depend on their radial position, estimated in terms of distance to the border of the colony (see figure 3.10a). On the contrary, the growth rate seemed homogeneous within the colony. Thus, the elongation of bacteria located near the center of the colony should induce movements of the peripheral cells. We thus analyzed the individual movements of cells to see whether such a pushing effect was taking place.

The distribution of distances travelled by each bacterium during its cycle was analyzed depending on the number of cells inside the colony (see paragraph 2.2.3). These distances were always broadly distributed, meaning that some bacteria experienced large displacements while others stayed roughly at the same position (see figure 3.10f). Yet, the medial travelled distance increased with the number of present cells, suggesting that the more cells

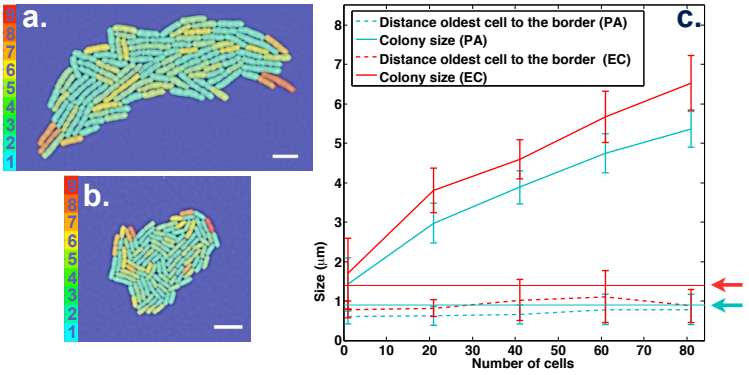

Figure 3.9 – Localization depending on age.
Image of about 100 cells microcolonies for *E. coli* (a) and *P. aeruginosa* (b). Scale bars are 5 μm and color represents the age of the cells expressed in number of generations (see paragraph 2.2.3 and figure 2.4). (c) Distance of the oldest pole in a colony with respect to the colony border (dashed line) compared to the characteristic size (calculated as the maximal distance to the border among cells inside the colony) of the colony (full line), for *E. coli* (red) and *P. aeruginosa* (blue). Red and blue arrows (and full straight lines) respectively mark the mean width of *E. coli* and *P. aeruginosa* cells.

there were, the more pushing occurred. Interestingly, outliers in this distribution moved by more than a cell length. This ruled out the possibility that these movements are only due to center of mass displacements resulting from individual cell elongations. Moreover, the travelled distance was likely to be larger when cells were located closer to the border of the colony (see figure 3.10e [4]). This corroborated the idea of a centrifugal pushing. Finally, we assessed the correlation between the displacement orientation α and the angular position θ of a given bacterium within the colony (see figures 3.10b and c, refer to figure 2.5b for a more detailed representation of the angles). Although broadly distributed, the difference $\alpha - \theta$ revealed a clear correlation between the two orientations (see figure 3.10d). This ensemble of measurements indicates that a centrifugal pushing, due to uniform growth, induces

4. Figure 3.10e also suggests that the organization is more regular when close to the border of the colony. Indeed, bacteria are preferentially located at around 0.7 μm and 2 μm. This roughly corresponds to 0.5 and 1.5 bacterial width. This is consistent with the observation that bacteria directly located on the edges of the colonies tend to align with the border. This alignment persists over at least two cell widths. It is difficult to probe this organization much further inside the colony due to the decreasing number of images of large colonies.

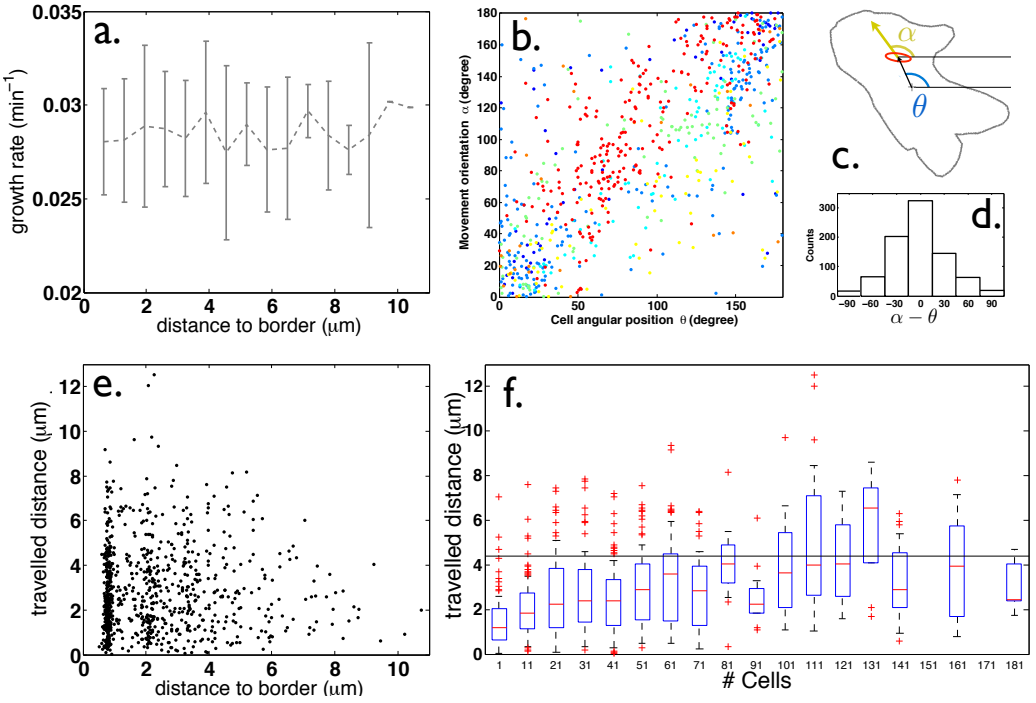

Figure 3.10 – Evidence of radial pushing in *E. coli* microcolonies.
(a) The growth rate of bacteria located at a given distance from the border of the colony are averaged with bins of 10 pixels (0.639 μm). (b) Orientation of the significant movement (greater than 3 μm) of the cells α versus the angular position of the cells θ. Each color stands for a colony (7 colonies were analyzed), each point represents a cell cycle (835 cells total). (c) Schematic representation of α and θ. (d) Distribution of the difference $\alpha - \theta$. (e) Travelled distance during one cell cycle versus the distance to the border of the colony. (f) Distribution of the travelled distances depending on the number of cell in the colony. For each point, the central red line is the median, the blue box contains the 25th and 75th percentiles, the whiskers extend to the most extreme data points not considered outliers, and outliers (larger than $2.5 \cdot q_{75} - 1.5 \cdot q_{25}$ or smaller than $2.5 \cdot q_{25} - 1.5 \cdot q_{75}$, where q_{25} and q_{75} are the 25th and 75th percentiles, respectively) are plotted as individual red crosses. The black line indicates the average length of an *E. coli* cell (4.4 μm).

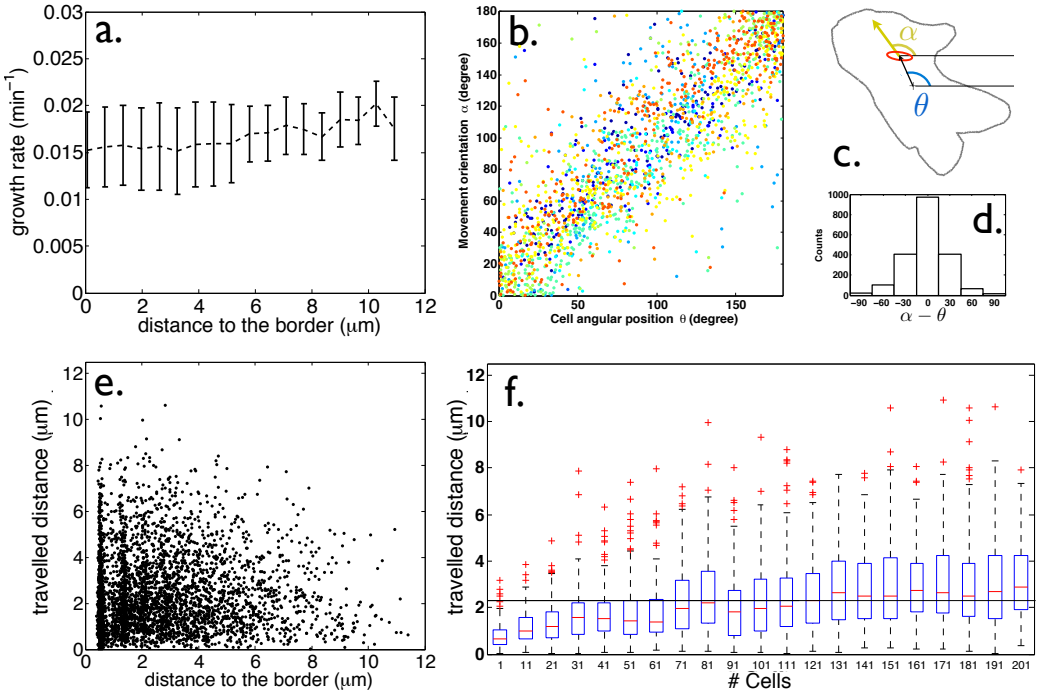

Figure 3.11 – Evidence of radial pushing in *P. aeruginosa* microcolonies. (a) The growth rate of bacteria located at a given distance from the border of the colony are averaged with bins of 10 pixels (0.639 μm). (b) Orientation of the significant movement (greater than 3 μm) of the cells α versus the angular position of the cells θ. Each color stands for a colony (7 colonies were analyzed), each point represents a cell cycle (1989 total). (c) Schematic representation of α and θ. (d) Distribution of the difference $\alpha - \theta$. (e) Travelled distance during one cell cycle versus the distance to the border of the colony. (f) Distribution of the travelled distances depending on the number of cell in the colony. For each point, the central red line is the median, the blue box contains the 25th and 75th percentiles, the whiskers extend to the most extreme data points not considered outliers, and outliers (larger than $2.5 \cdot q_{75} - 1.5 \cdot q_{25}$ or smaller than $2.5 \cdot q_{25} - 1.5 \cdot q_{75}$, where q_{25} and q_{75} are the 25th and 75th percentiles, respectively) are plotted as individual red crosses. A black line was superimposed to indicate the average length of an *P. aeruginosa* cell (2.3 μm).

radial movements of the cells within the colony. Similar observations were made for *P. aeruginosa* microcolonies (see figure 3.11), suggesting that such a mechanism may be general for growing microcolonies of rod-shape bacteria confined in 2D.

3.2.2 Organization of bacteria inside a microcolony

Shape dynamics

Initially, the microcolony develops as a line: first, the mother bacterium elongates, then, after septation, the two daughters keep elongating facing each other. But very early, with the reorganization (see paragraph 3.1.3 and figure 3.6), the colony starts to spread in two dimensions. To get an insight of how the spreading occurs next, we analyzed the temporal evolution of the aspect ratio (see paragraph 2.2.5) of colonies, for *E. coli* and *P. aeruginosa* (see figure 3.12). In general, *E. coli* colonies appeared more elongated than *P. aeruginosa* ones (see figure 3.13). Aspect ratios presented two trends: decrease at first, then increase. These trends were particularly marked for *E. coli* colonies. The initial decrease suggests that colonies first developed with a preferential dimension. When areas reached roughly 100 μm^2 (around 16 *E. coli* cells), aspect ratios started to increase indicating that spreading

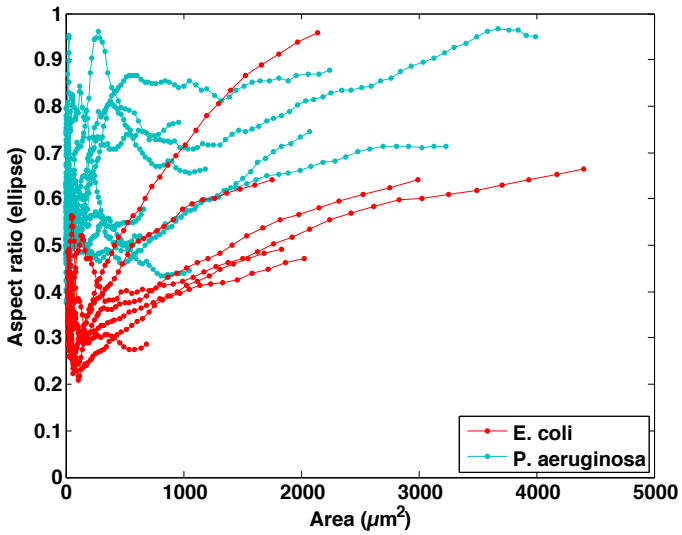

Figure 3.12 – Aspect ratio for *E. coli* and *P. aeruginosa* colonies.
Aspect ratios of the colony as a function of the colony area, for *E. coli* (7 colony growths, red) and for *P. aeruginosa* (10 colony growths, blue).

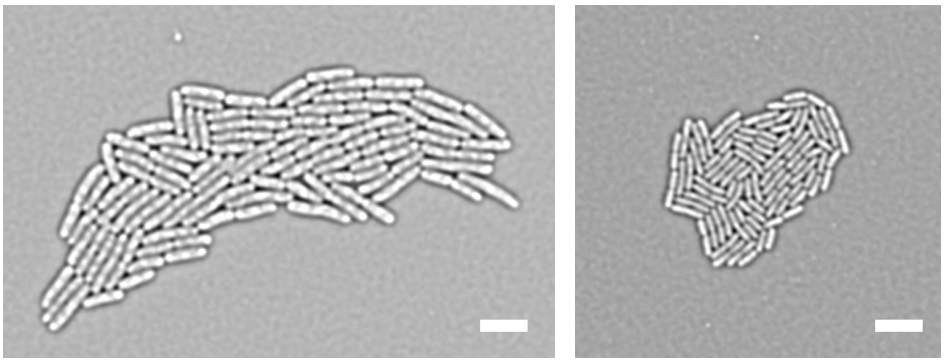

(a) *E. coli* 100 cells microcolony.

(b) *P. aeruginosa* 100 cells microcolony.

Figure 3.13 – Correlation images (see paragraph 2.1) of microcolonies counting approximately 100 cells for *E. coli* (left) and *P. aeruginosa* (right). Scale bar is 5 μm on each image.

became more isotropic. The radial pushing (evidenced in paragraph 3.2.1) as well as buckling instabilities (reported in paragraph 1.4 and evidenced in paragraph 3.1.3) are likely to explain this change in geometry. We wondered how this morphological change affects the internal organization of the colony, and in particular the orientation of bacteria.

Orientational order

Figure 3.14 represents the order parameter, $p = 2 <cos^2(\beta)> - 1$, where β is the angular orientation of a bacterium with respect to the orientation of the first one. Orientations were measured between 0 and 180 °, imposing that $p \in [0; 1]$. According to figure 3.14, bacteria progressively lost their orientational order as time proceeded. This decrease was exponential (see inset of figure 3.14) and the characteristic time for the loss of orientational order turned out to be 5 generations for *E. coli* and 2.2 for *P. aeruginosa*. This is consistent with the fact that *E. coli* colonies are more elongated than *P. aeruginosa* ones.

To understand the spatial organization, we studied pair correlations inside the colony. For each pair of cells (i, j), we calculated the quantity $(2 \cdot \cos^2(\beta_i - \beta_j) - 1)$ as a function of the distance between the cells (see figure 3.15). The analysis was carried out for colonies counting roughly 100

cells (see examples in figure 3.13). This pair correlation decreased exponentially with the cell-cell distance. The characteristic size over which the orientation of cells are correlated was respectively 8.9 μm and 4.5 μm for *E. coli* and *P. aeruginosa*. On average, this corresponds to the width of 6.5 side-by-side *E. coli* cells (respectively 4.6 side-by-side *P. aeruginosa* cells) and the length of 2 in-line *E. coli* cells (respectively 1.7 in-line *P. aeruginosa* cells).

These observations suggest that bacteria tend to align at short distances – probably due to cell-cell interactions and pushing forces– but are disorganized at larger distances –probably due to buckling.

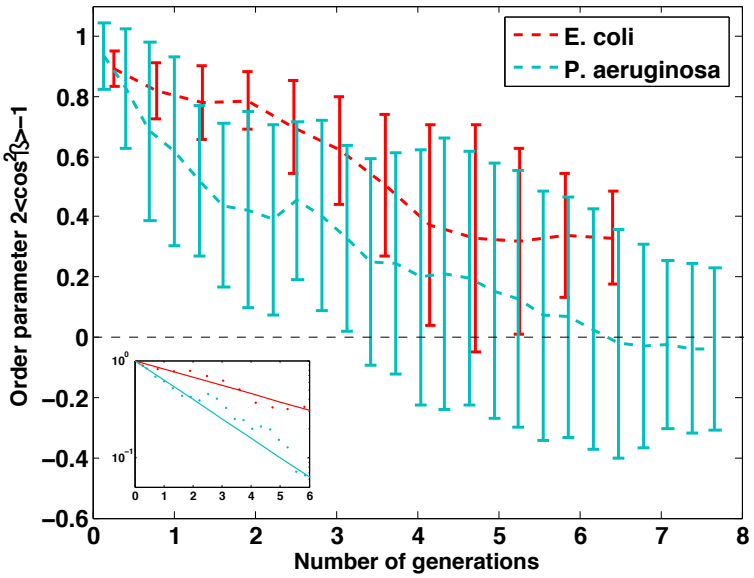

Figure 3.14 – Order parameter $p = 2 <cos^2(\beta)> - 1$ as a function of time, expressed in number of generations. The angle β is the orientation of a bacterium with respect to the orientation of the first cell of the colony. 7 and 10 growing colonies were analyzed respectively for *E. coli* (red) and *P. aeruginosa* (blue). Their respective mean generation times are 27 min and 50 min (see appendix C). Bin size is 15 minutes for both conditions. A semilog representation is proposed in inset for positive values of p, with fits $p = e^{-a \cdot t}$: a is respectively 0.20 min^{-1} and 0.46 min^{-1} for *E. coli* and *P. aeruginosa* ($R^2 = 0.9$ for both), corresponding to characteristic times of 5 and 2.2 generations.

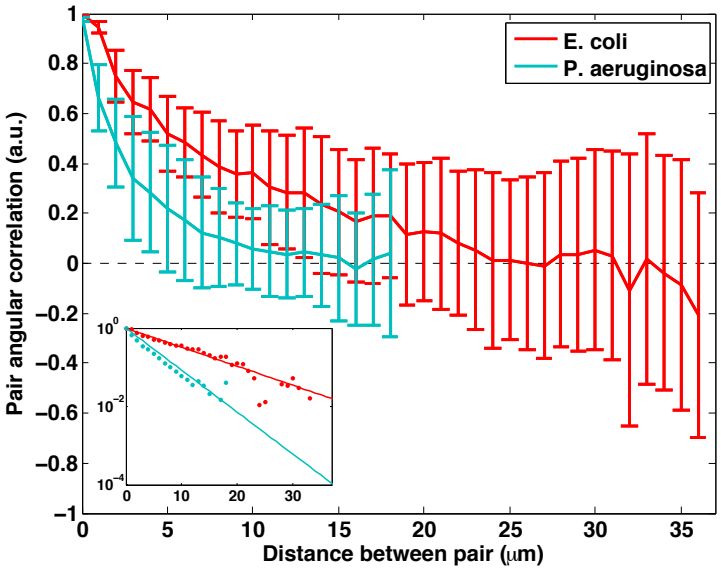

Figure 3.15 – Orientation correlation for pairs of cells depending on their distance. The correlation is calculated as $(2 \cdot \cos^2(\beta_i - \beta_j) - 1)$ for each pair of cells (i, j). 7 and 10 colonies counting around 100 cells were analyzed, respectively for *E. coli* (red) and *P. aeruginosa* (blue). Bin size is 1 μm and error bars represent the standard deviation. A semilog representation is proposed in inset for positive values of the correlation, with fits $y = e^{-a \cdot x}$: a is respectively 0.11 μm^{-1} and 0.25 μm^{-1} for *E. coli* and *P. aeruginosa*.

3.3 Cell-substrate adhesion during microcolony development

In part 3.1, we have demonstrated that adhesion is important for the mechanical description of the one and two cells stages. In part 3.2, we have shown that bacterial displacements can be significant within the growing colony, because cells are pushed by their neighbors. These displacements are likely to prevent the maturation of adhesion when the colony further develops. To probe the balance between these two effects (pushing forces and adhesion), we measured the cell-substrate interactions using a bacteria-adapted traction force microscopy technique (see part 2.5) that we developed.

We first present measurements for the *E. coli* wild-type strains (paragraphs 3.3.1, 3.3.2 and 3.3.3). Second, we analyze the changes in force level induced by modifications in the expression of adhesins (paragraph 3.3.4).

3.3.1 Spatio-temporal dynamics

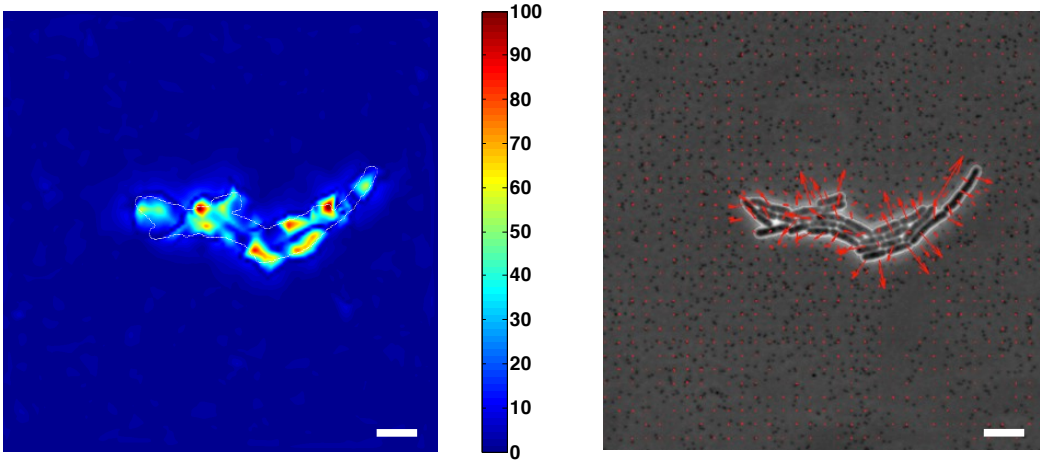

Figure 3.16 – Example of force measurements for wild-type *E. coli* colonies grown at 28 ° C. Scale bar is 5 μm on both panels.
Left panel: intensity maps of the measured forces (colorbar in pN). The thin white line represents the colony contour.
Right: the direction of forces (arbitrary units) overlaid on phase contrast images.

The distribution of forces inside the colonies turned out to be patchy, with zones of high forces and zones where the level of force was close to that of the background. The position of these patches was fluctuating with time. The forces were generally directed toward the exterior of the colony (see an example of force distribution in figure 3.16). Consequently, the denomination "traction force microscopy" does not seem appropriate in our case. From now on, we will talk about "force measurements".

Despite the spatial variability, the total force exerted by the colony on the substrate increased linearly with the variation in colony area (see figure 3.17a). The variation in colony area was calculated as the difference between the area of the considered colony and the area of the colony on the first im-

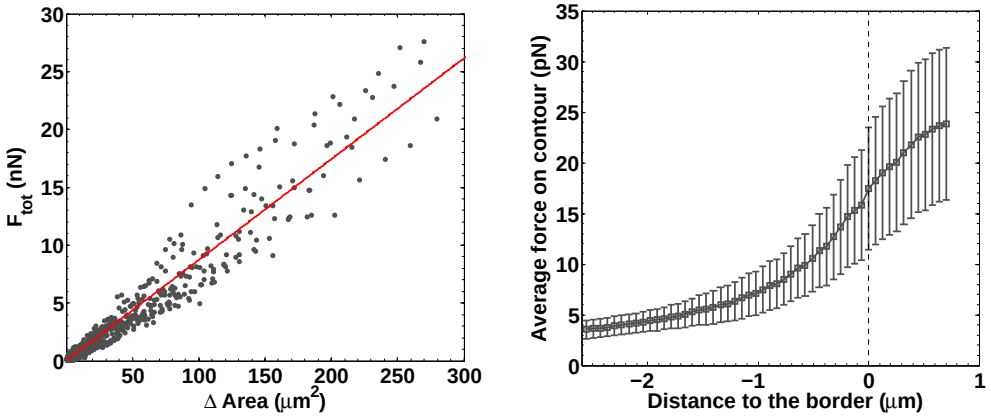

(a) Evolution of the total force.

(b) Force intensity vs the distance to the border.

Figure 3.17 – (a) Total force (sum of the intensity of local forces) exerted by a colony, depending on its variation in area compared to the first image. Each data point corresponds to a measurement at a given time for wild-type *E. coli* colonies growing at 28 ° C (a total of 13 colonies were analyzed). The data is well fitted ($R^2 = 0.93$) by a linear trend with slope 87 pN/μm^2. An area of 300 μm^2 corresponds to roughly 50 cells. (b) For colonies counting around 30 cells, we averaged the forces on rings (width 1 pixel, i.e. 63.9 nm) located at a given distance from the border of the colony (positive distance inside the colony, negative outside). The curve is averaged over 13 colonies. Bin size is 63.9 nm and error bars stand for the standard deviations between colonies.

age (in general, no more than 2 cells). Since the first image was used as a reference for the force calculation, its force level was set to zero by definition. The linear trend showed that the total force was proportional to the number of bacteria in the colony.

For force measurements, colonies were confined between a polyacrylamide gel, with embedded tracers, and an agarose gel containing nutrients (see figure 2.13). Far from the colony, the two gels were in contact. As the colony grew, the bacteria pulled apart the two gels. This vertical deformation could induce an horizontal component in the movements of beads. We wondered if the induced deformation could lead to artifactual force measurements. If it was the case, high force patches sould be located near the border of the colony. We thus analyzed the dependence of measured forces with the distance to the border of the colony. We averaged the force intensities over 1 pixel-wide[5] rings, located at a given distance from the colony border. The radial force appeared to increase smoothly when progressing from the outside to the inside of the colony (see figure 3.17b). This suggests that the contribution of the gel deformation is negligible when compared to forces attributed to cell-substrate interactions.

3.3.2 Rupture of adhesive bonds

Saturation of the maximal force inside the colony

We analyzed the maximal intensity of forces measured inside the colony, $F_{\max}$. Surprisingly, it appear to saturate for larger values of the colony area A (see figure 3.18a). We fitted this trend as:

$$F_{\max}(A) = F_{\max}^{\text{sat}} \cdot (1 - e^{-\frac{A}{A_0}}). \tag{3.4}$$

The characteristic area A_0 was 17 μm^2. This meant that for $3 \cdot A_0 = 51$ μm^2, or approximately 8 cells (see calibration the bacterial dimensions in table C.1 of appendix C), the saturation force was achieved (with a 5% tolerance). Such areas correspond to a situation where bacteria are surrounded by neighbors, the number of neighbors being on average 7 in these colonies [220]. Concomitantly, for colonies of such areas, displacements can start to be important inside the colony (see figure 3.18b). Taken together, these observations suggest that the saturation is linked to the elongation-induced displacements inside the colony.

5. 1 pixel is 63.9 nm.

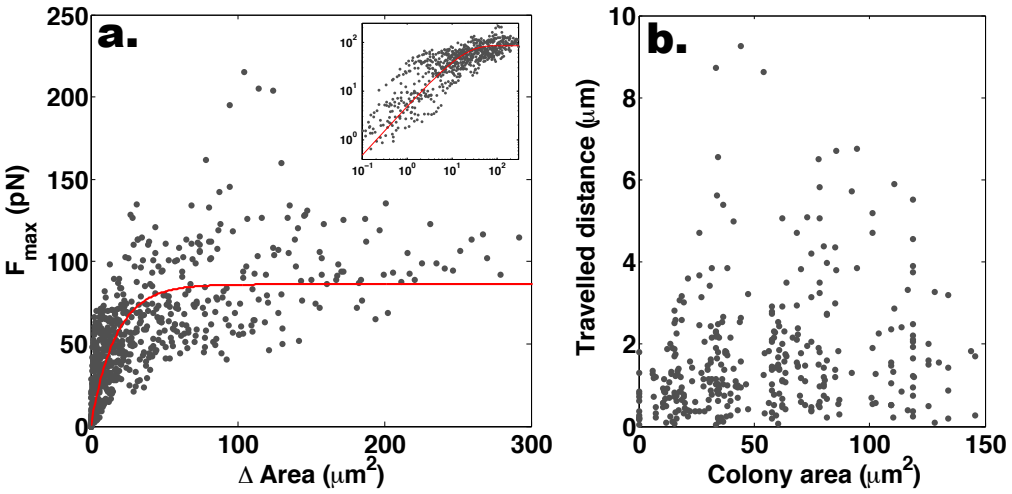

Figure 3.18 – (a) The maximal force observed inside the colony increases with the variation of area of the colony and then, saturates. Grey dots are extracted from measurements on 13 *E. coli* wild-type colonies growing at 28 °C. Each dot is a frame. The red line is the fitted trend: $F_{\max}(A) = F_{\max}^{\text{sat}} \cdot (1 - e^{-\frac{A}{A_0}})$ ($R^2 = 0.6$), with $F_{\max}^{\text{sat}} = 86$ $(83; 90)$ pN and $\frac{1}{A_0} = 0.059$ $(0.052; 0.066)$ μm^{-2} i.e. $A_0 = 17$ μm^2. The inset represents the data and the fit in log-scale. (b) Evolution of the travelled distance of bacteria over their cycle depending on the area of the colony. Each point stand for one bacterium. No data is provided for large areas since cells had not completed their cycle before the end of the acquisition.

It is unlikely that solid friction alone would explain the patchy force distribution we observed. We thus suspected that bacterial adhesion could significantly contribute to the forces we measured. To test this hypothesis, we carried out experiments with bacteria mutated in their adhesive properties. Levels of saturation were modified accordingly to the adhesive features of the strains (see paragraph 3.3.4). Such behavior could be explained by adhesive bonds being created and ruptured in a stick-slip-like phenomenon (see figure 3.19). In such case, when bacteria are motionless, no gel deformation should be observed, and thus no force. For increasing displacements, the force would first increase (load on the bond and possibly solid friction), and eventually relax as the bond ruptures. Such dynamics would account for the patchiness of the spatial force distribution. Moreover, it could also explain that the maximal force measured inside the colony saturates when displacements become large with the colony. In this context, the level of saturation may give an estimate of the maximal load that an adhesive bond (or an adhesive focus) can sustain before rupture. On the wild-type *E. coli* strain, this maximal load was measured to be 86 pN (see figure 3.18a).

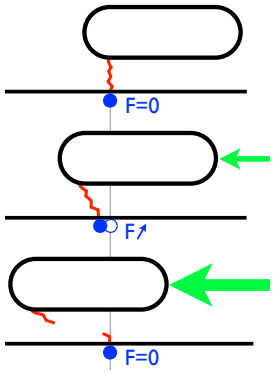

Figure 3.19 – Bond rupture scenario. F represents the force applied on the gel, measured from its deformation.

Anti-correlation between the instantaneous displacement and the variation of force at poles

In the literature, poles are described as inert surfaces from the point of view of peptidoglycan insertion (see paragraph 1.2.1). Thus, they are the only particular zone that keeps its integrity during the cell cycle despite elongation. In part 3.1, we showed that a gradient in adhesin concentration was established from the old pole to the new pole within two generations. These two considerations lead us into tracking the cell poles across generations, in order to investigate the dynamics of formation and rupture of adhesive bonds.

For each pole, we analyzed the force on the substrate and the displacement, compared to the position where the pole was created (see figure 3.20a for an example). We observed that the force increased when the pole had slightly moved on the surface. On the contrary, the force decreased when the pole moved a lot, suggesting that adhesive bonds could be ruptured. Such

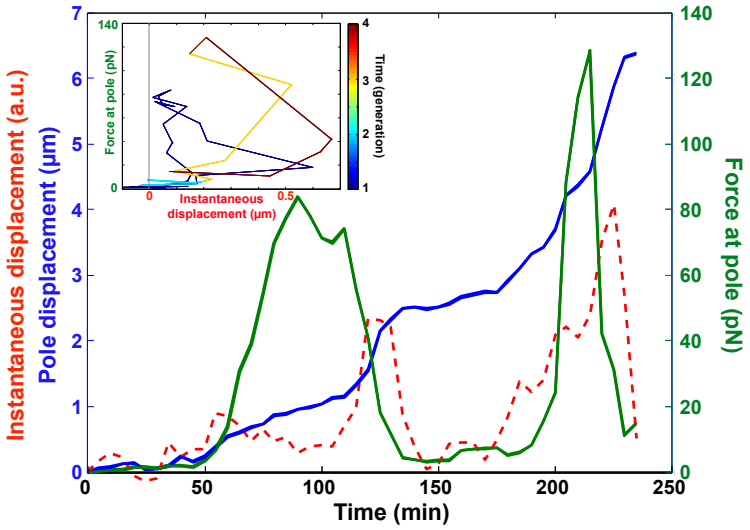

(a) Example of a pole displacement (blue), instantaneous displacement (red) and force (green).

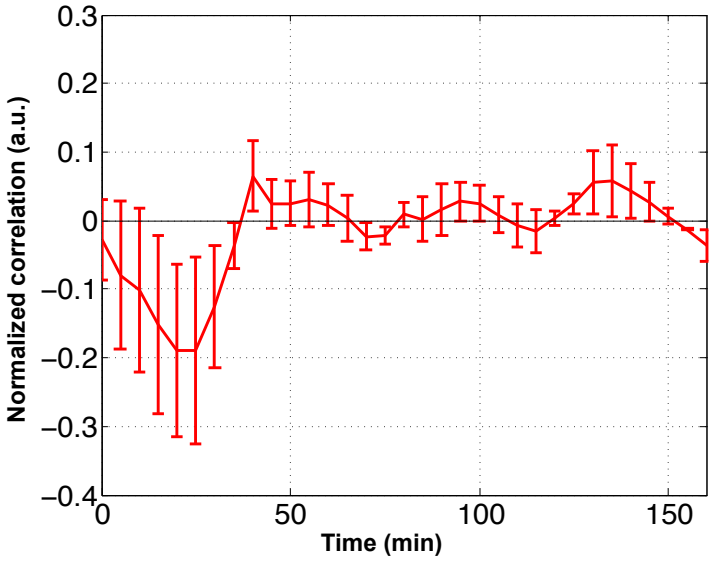

(b) Correlation between the instantaneous displacement and the variation of force.

Figure 3.20 – Displacement and force for poles tracked through generations. (a) Example of pole trace: the displacement with respect to the initial position (blue), the instantaneous displacement (red) and the force (green) are represented as a function of time. The force was averaged over a disk of 64 nm (10 pixels) in radius around the position of the pole. The inset shows the force as a function of the instantaneous displacement. The color code displays the time in generation (blue= 1, red= 4). (b) Normalized correlation of the instantaneous displacement and the variation of the force. These time series were smoothed over 3 time points. The curve was averaged over all the poles in 13 colony growths. Bin size is 5 minutes (acquisition rate) and error bars are standard errors.

trends corroborate the adhesive bond scenario: when the pole is immobile, the bond forms; when displacement is too large and/or too sudden, the bond is ruptured.

In order to probe this dynamics more systematically, for every tracked pole, we analyzed the correlation between the instantaneous displacement and the variation in force (see figure 3.20b). They turned out to be anti-correlated at short times (less than 40 minutes). This is consistent with the idea that when displacement increases, the force decreases with a given delay (adhesion rupture). The anti-correlation is maximal between 20 and 25 minutes, corresponding roughly to half a generation (generation times are calibrated in table C.1 of appendix C).

Three characteristic times are involved in a bond formation/rupture event:

1. the time during which the adhesion maturated, $\tau_{\text{maturation}}$,
2. the characteristic time of rupture, τ_{rupture},
3. the relaxation time of the gel deformation once the adhesion ruptures, τ_{gel}.

τ_{gel} corresponds to the delay between a bond rupture and the return of the gel to its relaxed state. $\tau_{\text{gel}} \approx 0$ since the gel is mostly elastic.
$\tau_{\text{maturation}}$ corresponds to the time the pole remained immobile enough for an adhesive bond to form. There is probably a lower boundary for this time under which no adhesion can form. Besides, the longer the maturation, the more important the strength of the adhesion, F_{max}, is likely to be. $<\tau_{\text{maturation}}(t)>$ may decrease as time proceeds, since average displacements increase inside the colony. $\tau_{\text{maturation}}$ corresponds to a quasi-null displacement and an increasing force. Its contribution to the considered correlation function should thus be weak.
τ_{rupture} may be expressed as:

$$\tau_{\text{rupture}} = \frac{\text{max distance}}{V_{\text{moy}}} \propto \frac{F_{\text{max}}}{V_{\text{moy}}} \tag{3.5}$$

where V_{moy} is the average speed of the pole, max distance represents the maximal distance an adhesion can be pulled away from the point where it maturated without rupturing. This distance is a priori linked to the strength of the adhesion, F_{max}. For instance, in the case of an elastic adhesion, max distance would be proportional to F_{max}.
Regarding these considerations, the delay between the increase in displacement and the decrease in force should be mostly governed by τ_{rupture}. The fact that it should be correlated to F_{max}, which varies both with time and space, might account for the broad anti-correlation peak.

3.3.3 Evidence for polar adhesion asymmetry in growing colonies

We observed an asymmetry in adhesion between the two poles of an isolated cell (see part 3.1). Force measurements offer a way to probe whether such an asymmetry persists during subsequent stages of growth, despite large cell movements (see paragraph 3.2.1 and figure 3.18b) during colony spreading. We thus developed a method to quantify this asymmetry in force measurement experiments. For each image, we located the preexisting and newly formed pole of each cell (see left panel of figure 3.21). A distribution of forces was obtained for the ensemble of preexisting poles on one hand, and for the ensemble of newly formed poles on the other hand. A spatial extension of radius 64 nm (10 pixels) around the position of the pole offered enough statistics to get an average force at the pole without loosing the spatiality of the measure. The maximal force value was computed for each distribution. We defined the normalized asymmetry in force as:

$$A_N(F) = \frac{F_{\max}^{\text{old}} - F_{\max}^{\text{new}}}{F_{\max}^{\text{sat}}} \ , \tag{3.6}$$

$F_{\max}^{\text{sat}}$ corresponding to the saturation value measured in figure 3.18.

The normalized asymmetry in force is displayed as a function of the area of the colony in figure 3.21. On average, the asymmetry is positive. This indicates that higher forces were measured at the preexisting poles, confirming the trend observed for isolated cells [6].

6. The initial null asymmetry corresponds to the two cells stage when all stresses applied on the substrate relaxed after the reorganization (see paragraph 3.1.3).

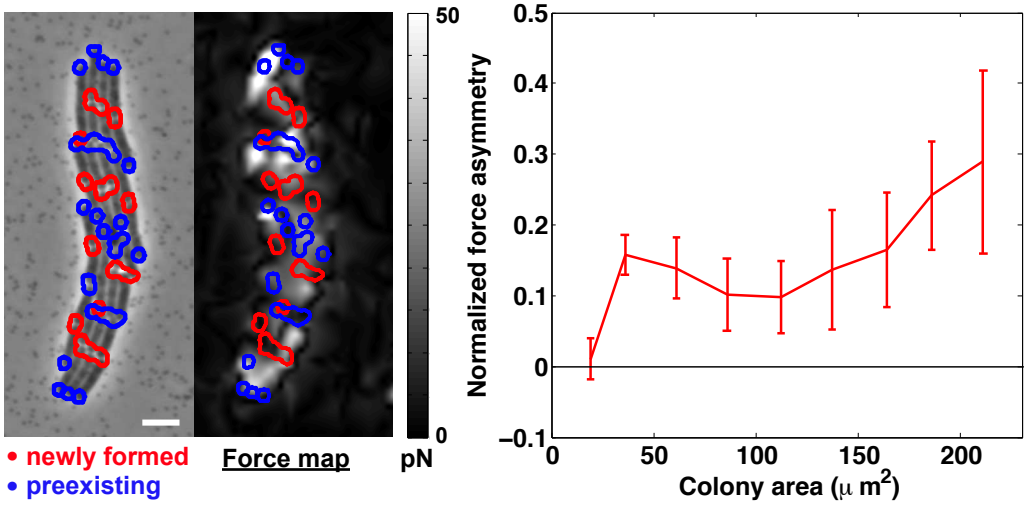

Figure 3.21 – Force asymmetry persists in a developing microcolony.
On the left panel, the location of preexisting (blue) and new (red) poles (spatial extension 64 nm in radius) is overlaid on the phase contrast image of the colony and the force map. Scale bar on phase contrast image is 5 μm. Right panel shows the evolution of the normalized asymmetry in force $A_N(F)$, defined by equation 3.6, as a function of the colony area. Positive values mean that the maximal force at preexisting poles is higher than the maximal force at newly formed poles. The presented curve is an average over 13 colony growths. Bin size is 25 μm^2 and error bars represent the standard errors.

3.3.4 Strength of adhesins

To ensure our technique was sensitive to adhesion forces, we carried out force measurements with strains modified for adhesin expression, for both *E. coli* and *P. aeruginosa* (see appendix A).

All the studied strains displayed the same behaviors as the *E. coli* wild-type strain. On the one hand, the total force was linear with the variation of colony area (see paragraph 3.3.1, figure 3.17a). On the other hand, the maximal force measured in the colony saturated with the variation of colony area (see paragraph 3.3.2, figure 3.18a). These observations offered two ways to quantify the adhesive strength of a given strain:

— the total force per unity of area, $F_{\text{tot}}^{\text{slope}}$ (left panel of figures 3.22 and 3.23),

— the saturation value of the local forces measured inside the colony, $F_{\text{max}}^{\text{sat}}$ (right panel of figures 3.22 and 3.23).

$F_{\text{max}}^{\text{sat}}$ is a local quantity. According to paragraph 3.3.2, it can be interpreted as the maximal load an adhesion can sustain before rupturing. $F_{\text{tot}}^{\text{slope}}$ gives of an measure that depends both on the value of$F_{\text{max}}^{\text{sat}}$ and on the number of bacteria within the colony.

E. coli appendages adhesive strength quantification

We measured forces for a quadruple mutant lacking (i) the subunit protein of curli fibers csgA, (ii) the subunit and tip proteins of type I fimbriae, fimA and fimH, (iii) antigen 43 and (iv) fliE and fliR, proteins necessary for the flagellum secretion (see paragraph 1.3.2). This strain will be referred to as Δadh and colored in green. We also studied OmpR234, a mutant strain that displayed an enhanced expression of the genes which expressions are controlled by the regulatory protein OmpR. In particular, curli fibers are about 3.5-fold more expressed for OmpR234 than for the wild-type [125]. OmpR234 is displayed in blue on figure 3.22. These strains were compared with the wild-type, referred to as WT and displayed in red. Since temperatures below 30 °C were shown to promote curli fibers expression (see paragraph 1.3.2), experiments were carried out at 34 °C and 28 °C.

For both temperatures, the total force per unity of area, $F_{\text{tot}}^{\text{slope}}$, was reduced for Δadh compared to the WT. This is consistent with the fact that appendages implied in adhesion were knocked-out in Δadh. However, the saturation value of local forces $F_{\text{max}}^{\text{sat}}$ was significantly decreased for Δadh at 28 °C but not at 34 °C. This strongly suggests that, among the 4 knock-

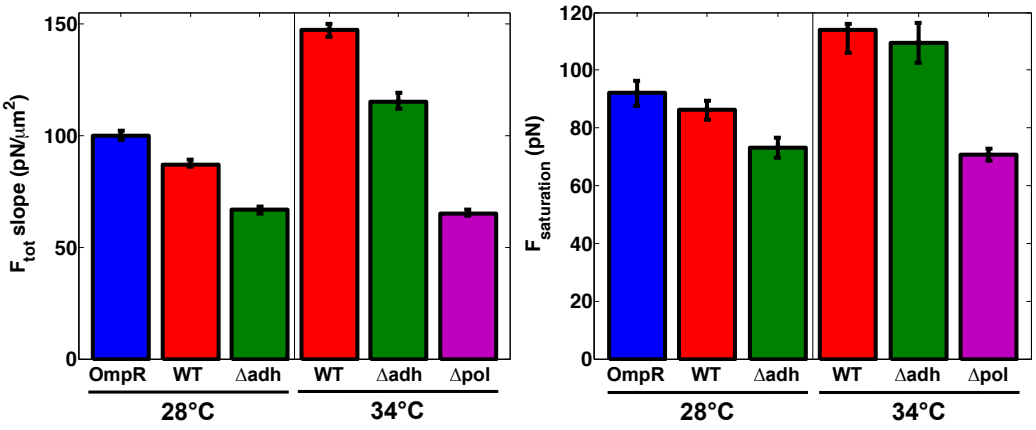

Figure 3.22 – Adhesive strength quantification for *E. coli*.
The total force is linear with the variation of area of the colony, compared to the reference image (see figure 3.17a). The left panel represents the slope of the fitted trend. The maximal force measured in the colony saturates with the variation of area (see figure 3.18). The right panel shows the saturation value $F_{\max}^{\text{sat}}$. Results are displayed for the wild-type and different adhesion mutants derived from the *E. coli* strain UGB52, studied at 28 ° C and 34 ° C. Error bars are given by the uncertainty of the fit (95% confidence interval).

out in Δadh, curli fibers are mainly responsible for the 13 pN increase in sustainable load observed at 28 ° C for the WT compared to Δadh.

A 28 ° C, the total force per unity of area, $F_{\text{tot}}^{\text{slope}}$, was increased when the expression of curli fibers was enhanced (strain OmpR234). On the other hand, the average values of $F_{\max}^{\text{sat}}$ were comparable (OmpR234 slightly higher than the WT but within the error bars). Considering that curli fibers are supposed to be over-expressed by a factor of 3.5 for OmpR234, $F_{\max}^{\text{sat}}$(OmpR234) $\approx F_{\max}^{\text{sat}}$(WT) suggests that $F_{\max}^{\text{sat}}$ may measure the rupture of a small number of bonds.

For both the WT and the quadruple adhesins/flagellum mutant (Δadh), higher forces were measured at 34 ° C than at 28 ° C. Several parameters are modified by a change in temperature and could account for modifications in adhesion. We know that the expression of curli fibers is reduced above 30 ° C, but other adhesion factors could be more expressed at 34 ° C than at 28 ° C. The bacterial growth rate is also modified. A change in the balance between these elements (adhesin expression and growth rate) would probably modify the dynamics of establishment of adhesions and influence force

measurements.

The removal of 4 polysaccharides induced a drastic drop in measured forces, both globally ($F_{\text{tot}}^{\text{slope}}$) and locally ($F_{\text{max}}^{\text{sat}}$) at 34 ° C.

P. aeruginosa fimbriae adhesive strength quantification

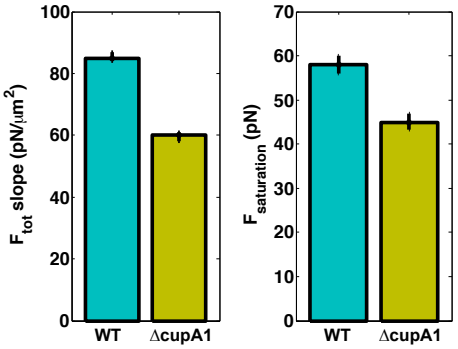

Figure 3.23 – Adhesive strength quantification for *P. aeruginosa*. Same quantities as in figure 3.22 for *P. aeruginosa* strain PA14 and PA14 ΔcupA1 at 34 ° C.

A similar study was carried out for *P. aeruginosa* strain PA14. A fimbriae knock-out ΔcupA1 was compared to the wild-type (see appendix A). The total force per area ($F_{\text{tot}}^{\text{slope}}$) was reduced by around 25%. The saturation value of the local forces measured in the colony ($F_{\text{max}}^{\text{sat}}$) decreased as well, by roughly 20%. These measurements suggest that, under our experimental conditions, the cup-encoded fimbriae play an important role in the adhesion of *P. aeruginosa* .

Moreover, one can note that forces measured for *P. aeruginosa* strains are lower than the ones measured for *E. coli*. Again, this could be attributed to a large number of factors that affect the force balance inside the colony (adhesins expression and strength, growth rate, internal organization, cell-cell interaction) as well as to the size of individual bacteria that differs by a factor of 3 [7].

7. Small size may involve less adhesins at the surface of the bacteria and thus, possibly, less adhesion forces. Moreover, in a flow, smaller bacteria experience smaller drag forces. Consequently, they might develop weaker adhesions than larger bacteria.

3.4 Contribution of adhesion to the morphogenesis of microcolonies

In parts 3.2 and 3.3, we showed that adhesions can be ruptured as bacteria are pushed by neighboring cells. Reciprocally, we wondered to which extent adhesion modifies the morphology of the colony.

3.4.1 Influence on morphology

To understand whether the shape adopted by a microcolony was related to adhesion, we carried out experiments for *E. coli* adhesion mutants (see appendix A). We measured aspect ratios (see paragraph 2.2.5) of growing colonies for two temperatures (28 ° C and 34 ° C) and in two different configurations –between agarose and glass (similarly to parts 3.1 and 3.2, see paragraph 2.3.3) or between agarose and polyacrylamide (force measurements, see paragraph 2.5.2).

Growth between agarose and glass at 34 ° C

In the agarose/glass configuration at 34 ° C, the wild-type *E. coli* strain (UGB52) was compared to single mutants lacking either (i) the subunit protein of curli fibers csgA, or (ii) the subunit and tip proteins of type I fimbriae, fimA and fimH, or (iii) antigen 43, or (iv) fliE and fliR, proteins necessary for the flagellum secretion (see paragraph 1.3.2). A quadruple mutant presenting these 4 deletions and a quadruple mutant of polysaccharides were studied as well.

The average aspect ratio of colonies formed by the wild-type (WT) was roughly constant and equal to 0.5 (see figure 3.24a). For the two quadruple mutants, the average aspect ratios were constant when area exceeded 100 μm^2 and their respective values were about 0.37 for the quadruple mutant of polysaccharides ($\Delta_4$polysaccharides) and about 0.25 for the quadruple mutant of adhesins and flagellum ($\Delta_4$adhesins). For single mutants of antigen 43 (Δflu) and fimbriae (ΔfimAH), the aspect ratio took intermediate values compared to the WT and $\Delta_4$adhesins. Taken together, these observations suggest that the value of the plateau is decreased when adhesion is reduced. Two mutants displayed an atypical behavior: for ΔfliER and ΔcsgA, the aspect ratio increased as the colony grew larger. We will discuss the case of ΔcsgA in the paragraph about the role of curli fibers.

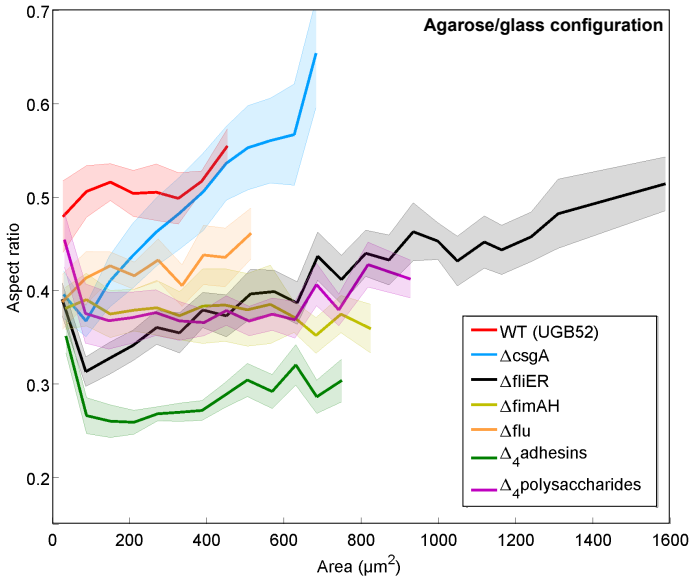

(a) Aspect ratios of different *E. coli* colonies.

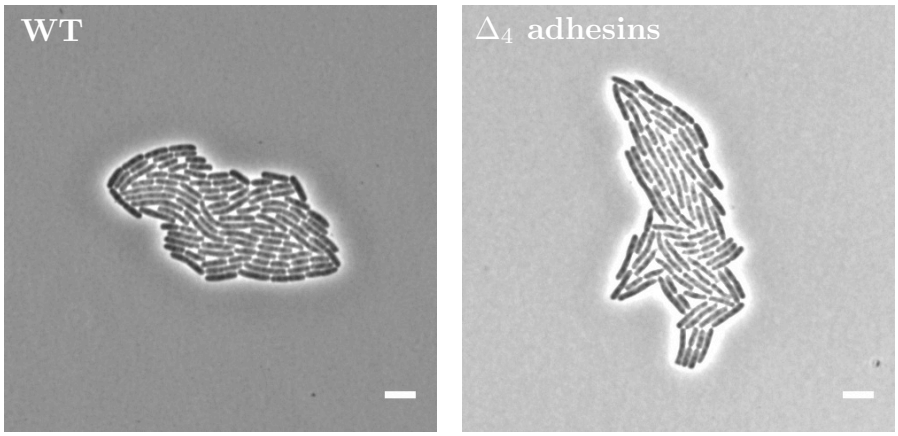

(b) Images of colonies formed by the *E. coli* WT (left) and $\Delta_4$adhesins (right).

Figure 3.24 – Comparison of the morphology of colonies formed by adhesion mutants of *E. coli* UGB52 growing between agarose and glass at 34 °C.
(a) Aspect ratios are shown depending on the area of the colony. Curves were averaged over at least 5 colony growths (up to 21) and were cut arbitrarily. Bin size is 60 μm^2. The shaded error interval represents the standard error.
(b) Phase contrast images of colonies formed by the wild-type (left) and $\Delta_4$adhesins, the quadruple adhesins and flagellum mutant (right). Scale bar is 5 μm for both images.

Shape modification depending on the temperature and the confinement

For all conditions, colonies formed by the WT grew more compact than the ones formed by $\Delta_4$polysaccharides (see figure 3.25). This suggests that adhesion, especially when mediated by the knock-out adhesins and/or flagella, is important to form compact colonies. This is consistent with the trend observed at 34 ° C between glass and agarose.

Additionaly, WT colonies grew in a more elongated fashion at 28 ° C than at 34 ° C between agarose and glass (see the left panel of figure 3.25). Consistently with what was observed on force measurements, this suggests that the level of adhesion is lower at 34 ° C than at 28 ° C. However, surprisingly, the temperature did not seem to significantly affect the shape of colonies between polyacrylamide and agarose (right panel).

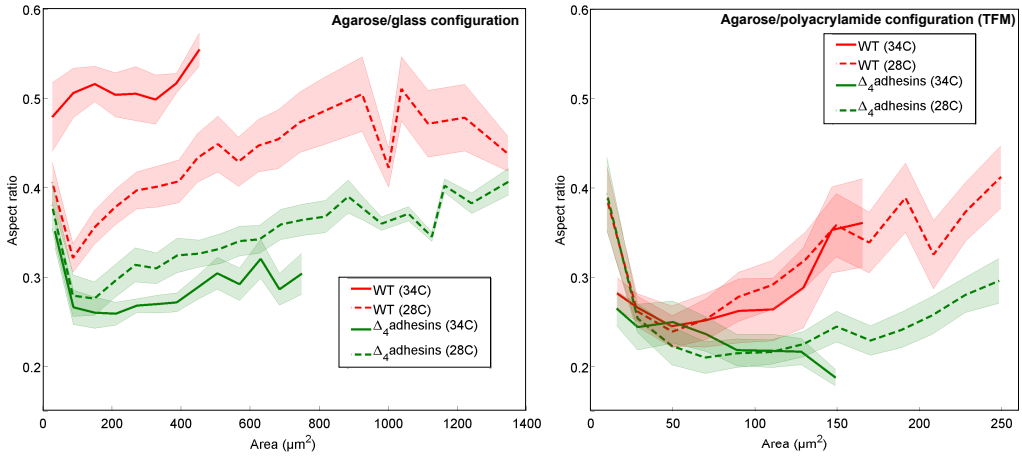

Figure 3.25 – Comparison of the shape of colonies formed by the *E. coli* wild-type (red) and $\Delta_4$adhesins, the quadruple adhesins and flagellum mutant (green) at 34 ° C (full lines) and 28 ° (dashed lines). Colonies were grown either between agarose and glass (left panel) or between agarose and polyacrylamide (right panel). Aspect ratios are shown depending on the area of the colony. Curves were averaged over at least 7 colony growths. Bin size is 60 μm^2 (left) and 20 μm^2 (right). The shaded error interval represents the standard error.

Role of curli fibers

Similarly to what we did for force measurements, we assessed the role of curli fibers at 28 ° C, since their expression is promoted at temperatures below 30 ° C. More adhesion forces had been measured for the curli overproducing strain OmpR234 (blue) than for the WT (see paragraph 3.3.4). Nevertheless, OmpR234 formed colonies with aspect ratios close (agarose/glass) or lower (agarose/polyacrylamide) than the WT (see figure 3.26). Similarly to what was observed for ΔcsgA at 34 ° C between agarose and glass (see figure 3.24a), it indicates that a reduced expression of curli fibers (other adhesins being the same) accelerates the recovery of a compact colony shape. Although less clear, the comparison of OmpR234 and OmpR234 ΔcsgA (turquoise) colonies seems to corroborate this idea (see the right panel of figure 3.26). This suggests that curli fibers could be implied in cell-cell adhesion. Indeed, cell-cell adhesion is expected to maintain the orientational order inside the colony and, thus, to drive colonies into more elongated shapes. In that case, depending on the major contribution of curli fibers (cell-adhesion or cell-substrate adhesion), it could explain that strains with a higher expression of

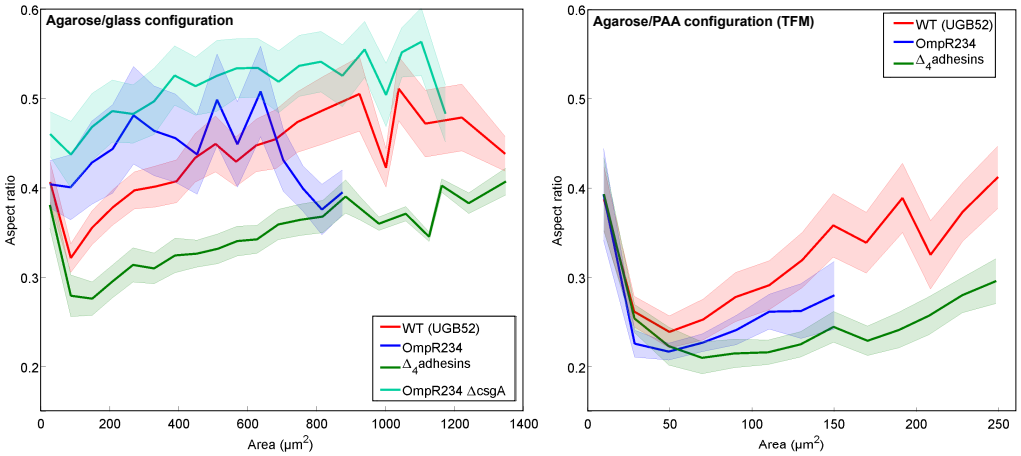

Figure 3.26 – Influence of the expression of curli fibers on the morphology of *E. coli* colonies grown at 28 ° C.
Colonies were grown either between agarose and glass (left panel) or between agarose and polyacrylamide (right panel). Aspect ratios are shown depending on the area of the colony. Curves were averaged over at least 7 colony growths. Bin size is 60 μm^2 (left) and 20 μm^2 (right). The shaded error interval represents the standard error.

curli fibers grow into more elongated shapes.

3.4.2 Role of adhesion in the transition from planar to a terraced colony

Context

All the presented experiments were performed for microcolonies confined in between two surfaces (glass/agarose or polyacrylamide/agarose). In either case, at least one of them was deformable allowing bacteria to start forming a second layer on top of the initial microcolony at some point in the development (see figure 3.27). Results reported so far were obtained in the first phase of colony growth, when it remained two-dimensional. We are now going to see which information can be deduced from the transition to 3D growth.

The gel is confining the colony vertically as well as laterally (see figure 3.28). Thus, to be able to spread in-plane, the colony has to overcome a lateral confinement which gets integrated over a larger and larger perimeter.

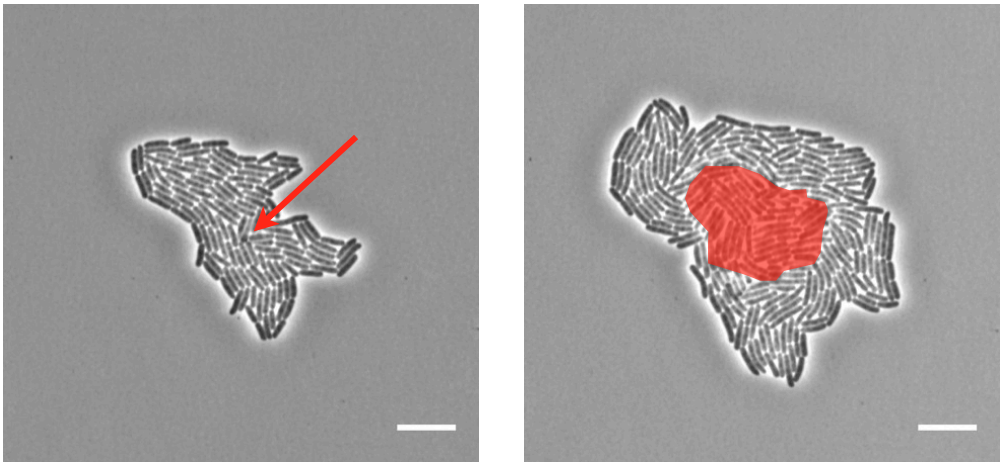

Figure 3.27 – Appearance of the second layer.
Images of a growing *E. coli* wild-type colony. Scale bar is 10 μm. Red arrow in the left image indicates the location of the first bacterium that buckles in the third dimension. The right image was taken 35 minutes after the leftone. The second layer is shaded in red.

Moreover, bacteria in the center have to push the surrounding cells that tend to adhere to the substrate (see paragraph 3.2.1 and figure 3.28). As their number increases, the adhesion force to overcome also gets higher. Thus, at some point in the colony development, the force to overcome laterally (increasing during the process) will become larger than the force required to deform the gel vertically (fixed for given bacterium). At this point, a second layer of cells will start growing on top of the first one. This phenomenon has been described for *E. coli* growing between glass and agarose in [204]: the area at which a second layer appears was shown to decrease with the stiffness of the agarose gel. However, the way bacteria-surface interaction influences the area at which the second layer appeared remained to be explored. Understanding this relationship motivated this last part of our study.

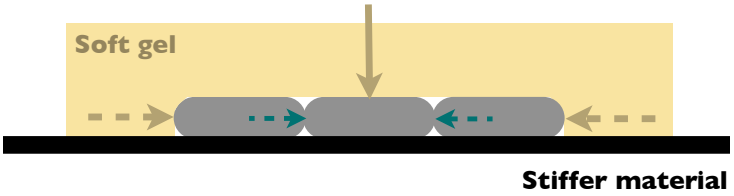

Figure 3.28 – Schematic representation of the external forces to overcome for the colony to grow: in beige, normal and lateral confinement due to the gel, and in blue, lateral confinement due to the other cells. The dashed forces (lateral confinement) are increasing as the perimeter of the colony extends.

Level of spreading depending on adhesion

The colony area at which the second layer first appears was systematically studied for the different *E. coli* strains (see appendix A and paragraph 3.4.1 for a detailed description). Independently from the confinement and from the temperature, less adhesive strains reached larger colony areas before they formed a second layer (see figures 3.29 and 3.30, left panel). The correlation between adhesion forces and area at double-layer formation could be quantified for both *E. coli* and *P. aeruginosa*[8] on force measurement experiments (see figure 3.30, right panel). The resulting plot shows a linear dependance between the number of cells inside the colony at second layer appearance and the saturation value of the maximal force measured inside

8. For *P. aeruginosa*, areas at second layer appearance are shown and discussed in paragraph 3.4.3.

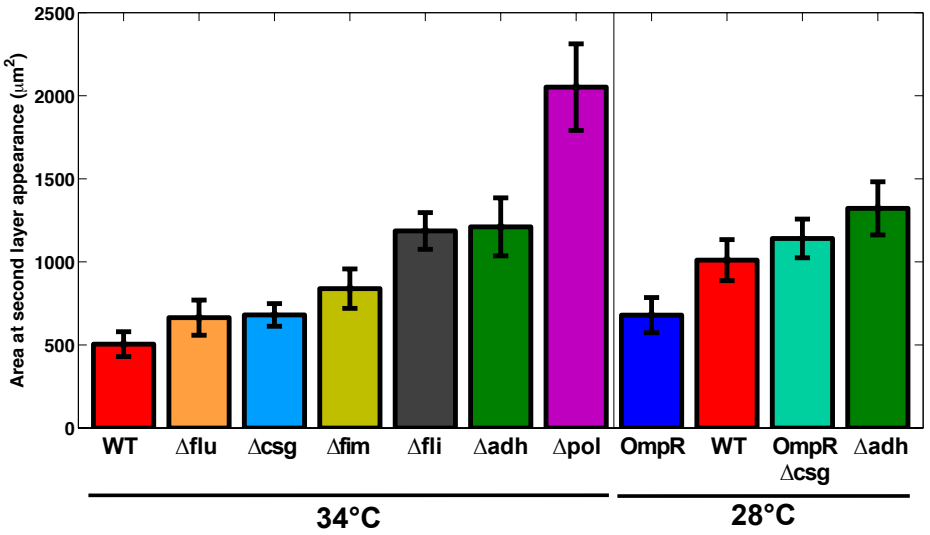

Figure 3.29 – Average surface of the colony at appearance of the second layer for *E. coli* mutants grown between agarose and glass. Error bars represent the standard deviations.

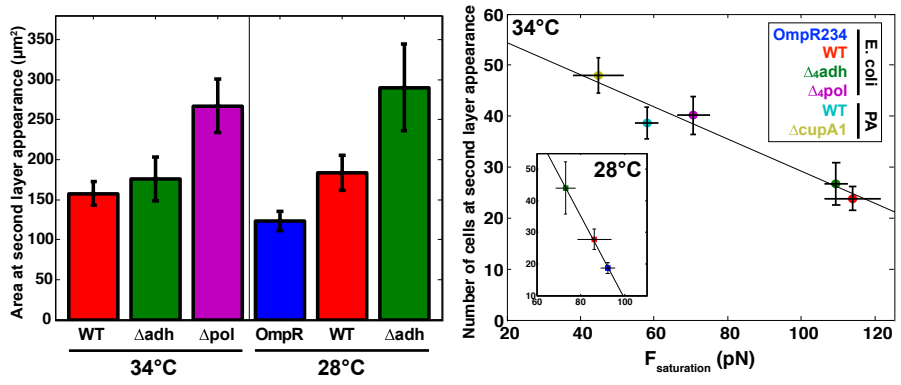

Figure 3.30 – Average surface of the colony at appearance of the second layer for *E. coli* mutants grown between agarose and polyacrylamide (left panel). The number of cells at appearance of the second layer is linear with the saturation value of the maximal force measured inside the colony. Fits: $N_{bact} = -a \cdot F_{\max}^{\text{sat}} + b$, with a = 0.31 pN^{-1} and b = 61 at 34 °C (*E. coli* and *P. aeruginosa*) and a = 1.31 pN^{-1} and b = 140 at 28 °C (*E. coli*); R^2=0.99 (see right panel). Error bars on the surfaces or number of cells are the standard errors, error bars on the force saturation are the uncertainty of the fit (95% confidence interval).

the colony, $F_{\max}^{\text{sat}}$ [9]. This strongly suggests that, in our case, the driving parameter in the transition from 2D to 3D growth is adhesion. Surprisingly, both *E. coli* and *P. aeruginosa* results at 34 °C could be fitted as a single trend, suggesting that this mechanism could be universal. Yet, the dynamics is different for experiments carried out with *E. coli* at 34 °C or at 28 °C. A possible explanation could come from the fact that the growth rate is affected by the change in temperature. Finally, the gel confinement may compete with the cell-substrate adhesion to induce the transition (see figure 3.28). In particular, for strains that only develop weak adhesions on their substrate, the gel confinement may trigger the second layer formation before enough adhesive forces had time to built up.

3.4.3 Adaptation to the environmental challenge

Iron is an essential nutrient for life, in particular for bacteria. *P. aeruginosa* cells retrieve the environmental iron by secreting molecules –siderophores– that have an high affinity with iron. In the extracellular environment, siderophores bind to iron and the cell eventually take them back in. This last process is driven by diffusion and is thus very unefficient. In the context of confined microcolonies, the concentration of pyoverdine, the main siderophore, was observed to be lower near the colony borders compared to the center [207]. This indicated that contact interactions are a way to prevent iron-bound siderophores from diffusing out. Thus, from the point of view of iron retrieving, minimizing the exchange surface with the environment seems beneficial. In a physical framework, this can be seen as a surface tension: creating a surface has a cost in terms of metabolism. Consequently, growing in 2D is less beneficial that growing in 3D. In order to see whether there could be a morphological adaptation to environmental conditions, we carried out force measurement experiments with *P. aeruginosa* wild-type strain PA14 in different iron conditions (see paragraph 2.5.2). A strain defective in fimbriae (ΔcupA1) was also studied.

As expected, under low iron conditions, PA14 grew more compact colonies than under normal conditions (see figure 3.31b). Moreover, PA14 formed double layers for smaller colony surfaces in low iron conditions (see left panel of figure 3.31a). Concomittantly, the maximal forces measured in the colonies did not reach a saturation level, as observed for both the WT and ΔcupA1 under normal conditions (see right panel of figure 3.31a). Additionally, higher forces were measured under low iron conditions. These observations suggest

9. The same trend was observed for the total level of force per unit of area, $F_{\text{tot}}^{\text{slope}}$.

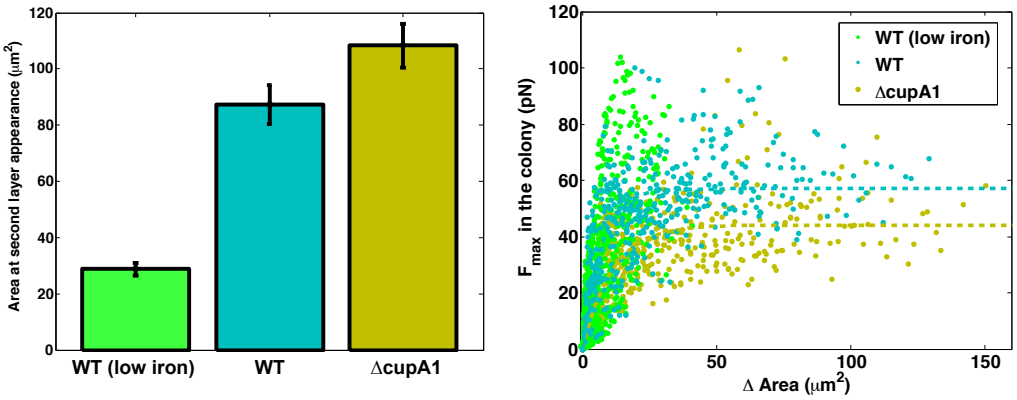

(a) Adhesion strength set the area of 2D spreading.

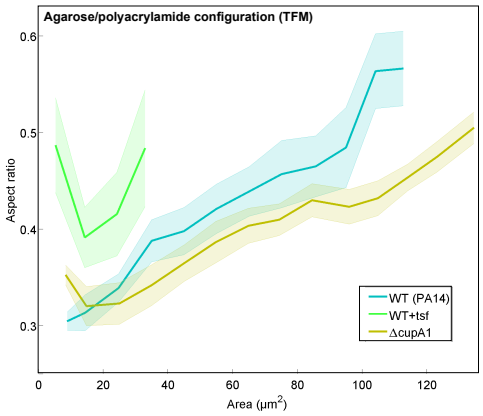

(b) Shape.

Figure 3.31 – Iron depletion.
The following strains were studied between agarose and polyacrylamide at 34 ° C: *P. aeruginosa* WT (PA14) under rich (LB medium, 16 colony growths, blue) and under low iron conditions (MMS medium+transferrin, 12 colony growths, green) and for PA14 ΔcupA1, a fimbriae mutant, under rich conditions (14 colony growths, beige). (a) Left panel displays the average colony surface when the second layer appears. Error bars are standard errors. Right panel represents the maximal forces measured within the colony depending on the area variation for the same conditions. For PA14 and PA14 ΔcupA1 under rich conditions, a saturation fit is proposed: the saturation values are respectively 58 pN and 45 pN (see paragraph 3.3.4). (b) Aspect ratio of the colony depending on its area. Bin size is 10 μm^2. The shaded error interval represents the standard error.

that adhesion could be a mechanism by which PA14 regulates its shape in response to low iron conditions. This is consistent with the fact that the less adhesive strain ΔcupA1 grows in a more elongated fashion and forms a double layer for larger colony areas (see figure 3.31).

Conclusion and perspectives

Bacteria develop sessile biofilms where they are less vulnerable to environmental aggressions. Compared to an isolated way of life, living in a biofilm confers an evolutive advantage to the cells. When a biofilm develops at a solid interface, bacteria strongly bind to the surface. The goal of this thesis was to advance our understanding of how bacteria adhering to a substrate are able to elongate while maintaining their contact with the surface.

For isolated cells, we have shown that growth is not symmetric with respect to their center of mass, despite an homogeneous elongation of the cell wall. This suggests that adhesion is asymmetric at the scale of a single cell. In order to probe the orientation of this asymmetry, we carried out laser ablation experiments which enabled us to follow an isolated cell through several generations. We have shown that the asymmetry always consists in a more anchored preexisting pole compared to the newly formed pole. Moreover, this asymmetry could maturate in less than two generations after the bacterium was brought in contact with the surface. We have emphasized that this asymmetry is important for the transition from a linearly growing cell to a two-dimensional compact colony. Indeed, after the first division, preexisting poles are located at both extremities of the line formed by the two daughter cells. This anchoring of preexisting poles biases the growth of the two cells toward each other and makes them slide along one another after septation.

Inside a colony, we have shown that individual growth rates are the same everywhere. The combination of these individual elongations results in a radial pushing which interferes with cellular adhesions. We wanted to understand how adhesion and elongation forces balance at the scale of a microcolony. This led to the development of a bacteria-adapted microscopy technique, which could accurately quantify the forces transmitted by bacteria to their substrate. Localized high force patches appeared and disappeared during colony growth. The total force exerted by the colony increased linearly

with the number of cells, but the maximal local force appeared to saturate. We interpreted this saturation as the signature of ruptures of adhesive bonds due to pushing forces resulting from elongation. This hypothesis is supported by the study of several adhesion mutants that displayed modified saturation levels. The level of saturation thus offered a way to measure the strength of *E. coli* and *P. aeruginosa* adhesins. For our wild-type *E. coli* strain, we measured forces on the order of 80 pN, which is consistent with previous measurements performed with other techniques.

Finally, by using mutant strains, we showed that adhesion influences the morphology of microcolonies. Indeed, when adhesion was weaker, colonies were more elongated and switched to a three-dimensional growth for larger colony areas. Taken together, these findings suggest that the expression of adhesins and their location at the surface of the cell could be used by bacteria to actively tune their interactions with the environment on one hand, and with their neighbors on the other hand, in order to modulate the shape of the group in which they reside.

Furthermore, our results indicate that additional forces may be at play during the morphogenesis of microcolonies. Indeed, most adhesins not only involved in cell-substrate adhesion but also in cell-cell interaction. In particular, the contribution of curli fibers to colony morphogenesis cannot be fully explained when considering only cell-substrate adhesion. A quantification of cell-cell interaction would thus provide a more complete understanding of microcolonies morphogenesis.

Appendix A

Bacterial strains used in this project

Name	*Genotype*	*Ancestor*	*Description*
MG1655			Wild-type strain
UGB52	MG1655		Wild-type strain
UGB935	MG1655 ΔcsgA::SpecR	UGB52	Deletion mutant of curli fibers
UGB2059	MG1655 ΔfliER::CmR	UGB52	Deletion mutant of flagella
UGB2139	MG1655 ΔfimAH::ZeoR	UGB52	Deletion mutant of type I fimbriae
UGB2416	MG1655 Δflu	UGB52	Deletion mutant of antigen 43
UGB2441	MG1655 gfpamp ΔfliER::Cm Δflu::FRT ΔfimAH::zeo ΔcsgA::spec	UGB52	Deletion mutant of the 4 main adhesion factors
UGB3582	MG1655 ΔyjbEH::cat ΔbcsA::KmFRT phaA::uidA-zeo cps5::Tn10	UGB52	Deletion mutant of the 4 described polysaccharides
UGB3323	MG1655 ΔompA::KmR	UGB52	Deletion mutant of OmpA porine
UGB1236	OmpR234	UGB52	Over-expression of the regulatory protein OmpR
UGB3485	OmpR234 ΔcsgA	UGB52	Over-expression of the regulatory protein OmpR, deletion mutant of curli fibers

Table A.1 – *E. coli* strains.
The strain derived from UGB52 were given by Jean-Marc Ghigo and Christophe Beloin from the Genetics of Biofilms lab in Institut Pasteur. The first MG1655 strain provided data presented in part 3.2, all other experiments were carried out with UGB strains.

Name	*Genotype*	*Ancestor*	*Comment*
PAO1			Wild-type strain
PA14			Wild-type strain
ΔCupA1	PA14 ΔCupA1	PA14	Deletion mutant of fimbriae

Table A.2 – *P. aeruginosa* strains.

Appendix B

Experimental protocols

B.1 Agarose/glass sample preparation protocol

Bacterial solution In order to grow a bacterial microcolony confined between glass and agarose, the strain of interest (see appendix A) was grown overnight in LB (lysogeny broth) lennox as a shaking culture at 37 ° C at 200 revolutions per minutes (rpm). This solution was diluted to have a single or many isolated cells in each field of view [1].

Agarose pad preparation A fresh agarose solution was prepared for each experiments at the desired concentration in a given medium. A typical concentration was 1% (0.1 g of agarose in 10 mL of medium) in LB. The solution was warmed up in a microwave by successive heating cycles. Still warm, 200 μL of the solution were moulded in a double sided adhesive spacer, bound to a glass slide. In order to have a flat surface on top of the gel, another glass slide was deposited on the gel. In this configuration, the gel was allowed to solidify for about 10 minutes at 4 ° C.

Under sterile conditions, the upper slide was slid off the gel parallel to the surface plane in order to avoid making any defaults on the gel surface. A channel was opened in the middle of the gel and the spacer to supply the bacteria with oxygen. The sample was thus separated in two parts that could be used to image two different strains at the same time. Each side of the agarose pad was seeded with a 2 μL drop of bacterial solution. The agarose pad, seeded with bacteria, was then sealed onto a glass coverslip thanks to

1. Typically, from 1000-fold to 10 000-fold for a single cell per field when overnight culture reached saturation, which was usually the case. The width of the squared field of view varied from 70 to 140 μm.

the adhesive spacer. A schematic of the sample is displayed in figure B.1.

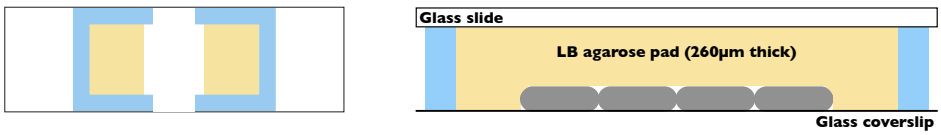

(a) Top view. (b) Side view.

Figure B.1 – Schematic representation of a sample.
The sample is composed of an agarose pad (hatched in (a) and beige in (b)) moulded in a spacer (blue). A oxygen supply channel was cut separating the pad in two sides (a). Imaging was done through the lower glass coverslip (b). Scales of scheme (b) are not realistic.

B.2 Force measurement protocol

B.2.1 Prior to experiment

Preparation of the polyacrylamide solution

— Dilute the acrylamide and bis-acrylamide commercial solution in dPBS in different proportions depending on the desired stiffness (see table B.1).
— Vortex the solution.
— Solutions can be kept at 4 °C (for 3 month maximum).
— An aliquot of 167 μL is used for each gel.

for 10 mL	1 kPa (1.10±0.34)	2 kPa (2.01±0.75)	3 kPa (3.24±0.58)	4 kPa (4.47±1.19)	7 kPa (7.43)
dPBS	8.75 mL	8.5 mL	7.5 mL	8 mL	7.2 mL
Acrylamide	0.75 mL	1 mL	1 mL	1.25 mL	2.5 mL
Bis-acrylamide	0.5 mL	0.5 mL	1.5 mL	0.75 mL	0.3 mL

Table B.1 – Correspondence between the gel stiffness and the acrylamide-bisacrylamide concentration [214]. All the presented experiments (see parts 3.3 and 3.4) were performed with a 4 kPa concentration.

BindSilane coating of large coverslips

— Dilute 484 μL of 10% acetic acid and 55.7 μL of pure BindSilane (Dutsher 17-1330-01) in 14.46 mL of ethanol. This solution can be kept at 4 $^\circ$C for a few months.
— Put a drop of around 180 μL of the diluted solution on a large coverslip.
— Spread and wipe out with a KimTech paper to have it homogeneous on the surface before it dries.
— Conserve the coated coverslips in a parafilm-sealed Petri dish.

[Optional] Small coverslip coating with SigmaCote

— Immerse a small coverslip in a non diluted SigmaCote solution (binding is quasi-instantaneous).
— Dry the coverslip under a hood.
— Cook for 15 minutes at 37 $^\circ$C to strengthen the coating.
— Rinse thoroughly with sterile water and dry again under a hood.

B.2.2 Preparation on experiment day

Polyacrylamide gel polymerization

— Prepare a 167 μL aliquot of dPBS-acrylamide-bisacrylamide solution.
— Sonicate the fluorescent bead stock (FC02F, Bangs Laboratories) for 1 minute.
— Add 2 μL of fluorescent beads to the polyacrylamide solution.
— Sonicate for 1 minute.
— Add 1 μL of TEMED. Homogenize by shaking the aliquot.
— Add 1 μL of previously unfrozen and vortex 10% APS solution.
— Vortex.
— Put a 10 μL drop of the solution on a large coverslip (BindSilane coated) and carefully deposit a small glass coverslip (15 mm$\times$15 mm) on top.
— Put the gel in a humid and dark chamber (Petri dish with a humid KimTech paper) and let it polymerize for 1.5 hours. Do not displace the gel during polymerization. Make sure the gel is not dry after this time.

Small coverslip removal After polymerization, add a drop of distilled water (around 1 mL) on the gel and carefully detach the upper coverslip by inserting a scalpel in between the gel and the coverslip at a corner. Maintain

the gel with tweezers.

Rinsing step In order to limit the toxicity due to the acrylamide and remove potentially non-embedded beads, the gels are rinsed for 2 hours.

— Put the large coverslip inside a 25 mL bath of sterile filtered water with the gel facing down and leave it for 1 hour.
— Switch bath and leave again for 1 hour.

Agarose gel preparation Under sterile conditions,

— prepare a warm 2% agarose gel with the desired medium,
— warm it up until it is homogeneous and mould 200 μL to fill a double side adhesive spacer on a glass slide,
— put a second slide on top,
— let the gel polymerize for around 10 minutes at 4 $^\circ$C,
— remove the upper slide by translating it on top of the gel.

Sample preparation Under sterile conditions,

— cut a few millimeters on each side of the agarose pad and open two side channels in the spacer for oxygen supply,
— remove the protection of the spacer,
— put 2 μL of bacterial solution (usually diluted 10^3 to 10^4 times in LB compared from a saturated solution),
— remove the acrylamide gel from the rinsing bath and remove the remaining water with a paper by capillarity without touching the gel,
— close the sample by putting the acrylamide coverslip on top on the agarose pad,
— seal the adhesive spacer by softly pressing on the adhesive spacer.

Appendix C

Growth rate and bacterial size quantification

For our two experimental situations (agarose/glass or agarose/polyacrylamide), we calibrate the growth rate and size (surface, length after division and width) of the bacterial strains we studied (summary of all values in table C.1). In paragraph C.1, we propose the detailed analysis for *E. coli* and *P. aeruginosa* wild-type strains grown at 34 $^\circ$ between agarose and glass. In paragraph C.2, we report the results of a similar analysis for force measurement experiments. They were carried out at 28 $^\circ$ C for different stains of *E. coli* and *P. aeruginosa*.

C.1 Colonies growing between agarose and glass at 34 degrees C

C.1.1 Growth rate

The growth rate can be estimated for individual cells (see paragraph 2.2.3 and figure 2.5a) or for the whole microcolony. We measured the global growth rate of *E. coli* and *P. aeruginosa* by fitting the area $\mathcal{A}$ of the colony masks (see paragraph 2.2.1) as $\mathcal{A} = \mathcal{A}_0 \cdot e^{\alpha t}$, where α was the growth rate and $\mathcal{A}_0$ a constant. A semilog plot of the areas versus time is displayed in figure C.1 for each colony growth. The values of strain growth rate (averaged over multiple colonies growths) are 0.026 ± 0.0005 min^{-1} for *E. coli* and 0.014 ± 0.002 min^{-1} for *P. aeruginosa*. The corresponding generation times are respectively 26.7 minutes and 49.5 min.

The beginning of the growth is not well described by the exponential law. Indeed, there is always a variable lag (between 1 and 3 hours) for bacteria taken from a stationary liquid phase, to start growing exponentially again in solid conditions. This lag can be observed on figure C.1, but does not affect the quality of the fits.

C.1.2 Mean bacterial size

C.1.2.1 Mean bacterial area

Estimating the size of individual bacteria is not trivial since bacterial length doubles within a cell cycle. To get rid of this variability, we combined single segmentation (see paragraph 2.2.2) with global colony segmentation (see paragraph 2.2.1). Since the plot of the colony area vs the number of bacteria inside the colony is consistent with a linear relation, the slope of the linear fit provides an average estimation of the area occupied by a single bacterium (see figure C.2). Underlying hypothesis are (i) that the colony is compact and (ii) that the cell size, averaged over the cycle, does not depend on time[1]. The goodness of the fits ($R^2 > 0.97$) and the apparent compactness of colonies (see figure 3.13) suggest that effect (i) would be insignificant. We neglected effected (ii) since we were far from the saturation regime (colonies kept growing for hours after we stopped the experiment).

The estimated bacterial surface, averaged over multiple colony growths, was 6.5 ± 0.3 μm^2 for *E. coli* and 2.3 ± 0.2 μm^2 for *P. aeruginosa*, where errors are the standard deviation of the distributions.

C.1.2.2 Mean bacterial dimensions

Length after division The bacterial length varies along the cell cycle. In order to estimate a mean bacterial length without being disturbed by this variability, we estimated the mean bacterial length after division (see figure C.3a). The average value is 4.4 ± 0.7 μm for *E. coli* ($N = 2501$) and 2.3 ± 0.4 μm for *P. aeruginosa* ($N = 7360$).

Width On the other hand, the bacterial width is not affected by growth. We estimated it for all segmented cells (see figure C.3b). The average value is 1.4 ± 0.1 μm for *E. coli* ($N = 15177$) and 0.9 ± 0.1 μm for *P. aeruginosa* ($N = 69620$).

1. For instance, bacteria become shorter when they enter the saturation phase (see paragraph 1.1.2).

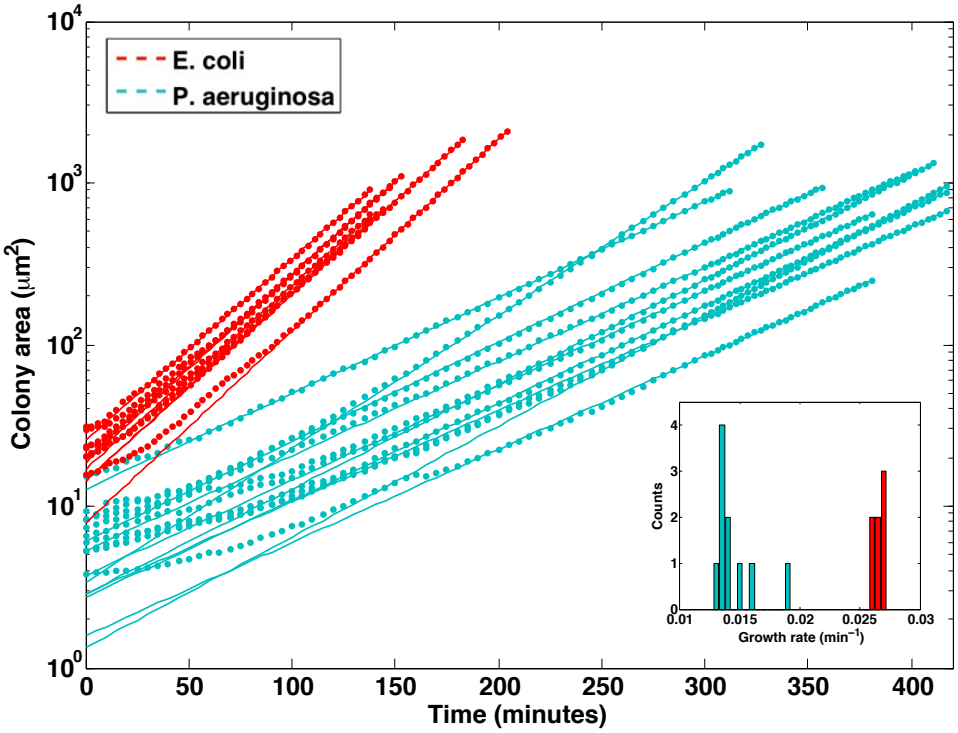

Figure C.1 – Colony area depending on time for *E. coli* (red) and *P. aeruginosa* (blue). The colony area $\mathcal{A}$ is represented in log scale, and fitted with an affine relation: $\log \mathcal{A} = \alpha t + \beta$ (all $R^2 > 0.99$). Slopes α define the growth rate of the colony and their distribution is displayed in the inset for each strain. $< \alpha^{\text{E. coli}} >= 0.026 \pm 0.0005$ min^{-1} and $< \alpha^{\text{P. aeruginosa}} >= 0.014 \pm 0.002$ min^{-1}, corresponding respectively with characteristic times of 38.5 min and 71.4 min.

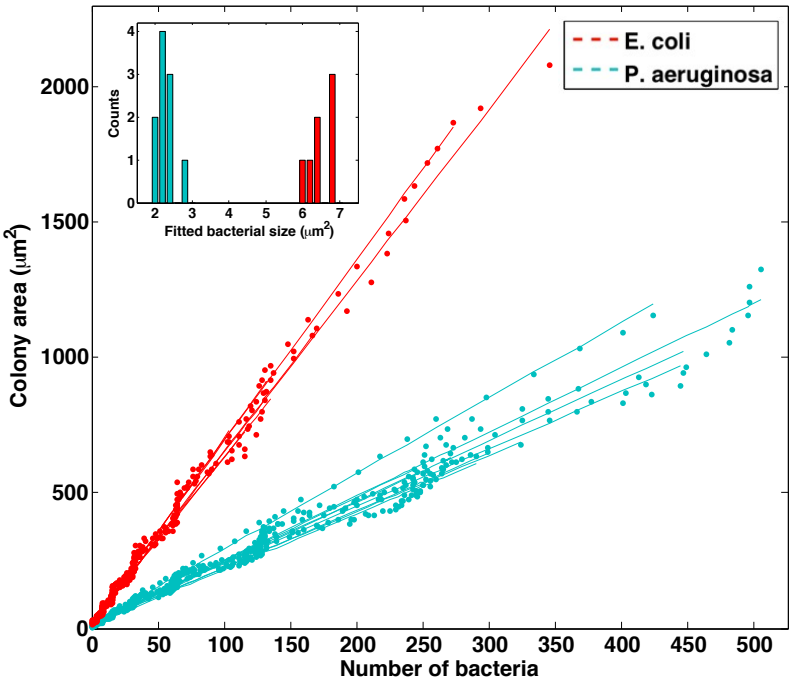

Figure C.2 – Linear fits of the colony area depending on the number of bacteria in the colony for *E. coli* (red) and *P. aeruginosa* (blue). The distribution of the slopes, corresponding to the average bacterial surface, are displayed in the inset (bin size is 0.2 μm^2). 7 colony growths were considered for *E. coli* and 10 for *P. aeruginosa*.

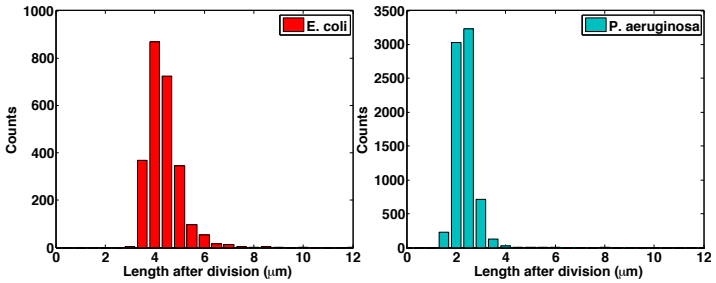

(a) Lengths after division distributions.

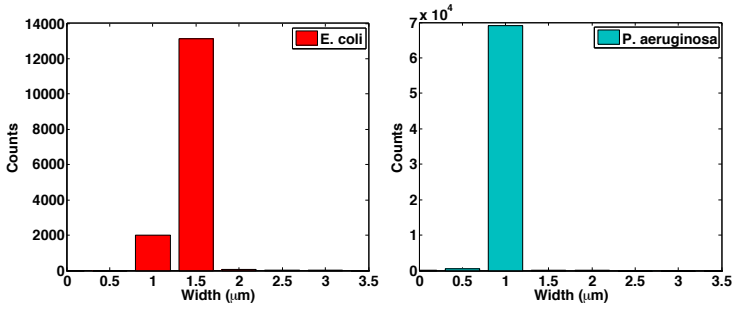

(b) Width distributions.

Figure C.3 – Distribution of lengths after division (a) and the width (b) of *E. coli* (red) and *P. aeruginosa* (blue). The average length after division is 4.4 ± 0.7 μm for *E. coli* ($N = 2501$) and 2.3 ± 0.4 μm for *P. aeruginosa* ($N = 7360$). The average width is 1.4 ± 0.1 μm for *E. coli* ($N = 15177$) and 0.9 ± 0.1 μm for *P. aeruginosa* ($N = 69620$).

C.2 Colonies growing between agarose and polyacrylamide at 28 degrees C

The same analyses were carried for force measurement experiments. Results are displayed in table C.1.

	Strain	Growth rate (min^{-1})	Generation time (min)	Cell surface (μm^2)	Length after division (μm)	Width (μm)	Growth medium	Temperature ($^\circ$C)
Agar./glass	*E. coli*							
	WT	$0.026 \pm 5 \cdot 10^{-4}$	26.4	6.5 ± 0.3	4.4 ± 0.7	1.4 ± 0.1	LB	34
	P. aeruginosa							
	WT	$0.014 \pm 2 \cdot 10^{-4}$	49.5	2.3 ± 0.2	2.3 ± 0.4	0.9 ± 0.1	MMS	34
Agarose/PAA	*E. coli*							
	WT	0.015 ± 10^{-3}	46.2	6.15 ± 1.2	4.7 ± 1.5	1.4 ± 0.1	LB	28
	OmpR234	$0.014 \pm 9 \cdot 10^{-4}$	49.5	5.4 ± 0.6	4.0 ± 0.9	1.4 ± 0.1	LB	28
	$\Delta_4$adhesins	0.015 ± 10^{-3}	46.2	6.3 ± 1.0	5.6 ± 1.3	1.4 ± 0.1	LB	28
	P. aeruginosa							
	WT	$0.017 \pm 8 \cdot 10^{-4}$	40.8	2.8 ± 0.3	2.5 ± 0.7	0.9 ± 0.2	LB	34
	ΔcupA1	0.016 ± 10^{-4}	43.3	2.7 ± 0.2	2.3 ± 0.6	0.9 ± 0.1	LB	34

Table C.1 – Growth rate and bacterial size calibration for all the experiments that were segmented at a single-cell level. Errors associated with mean values are given by standard deviations.

Appendix D

Preliminary experiments

In this appendix, we report experimental observations that would require further confirmation. Yet, we thought they could provide interesting perspectives to the work presented in the main part of this thesis.

D.1 Cell length measurements during septation

Once it has divided, the first cell (mother) gives rise to two daughters that grow in-line, then slide along one another. We refer to this phenomenon as the reorganization (see paragraph 3.1.3). After the second division, the two grand-daughter cells are in a similar in-line configuration but reorganization is prevented by the non-yet-divided cell that is aside them (see figure D.1 and paragraph 3.1.3). By ablating the non-yet-divided cell (see paragraph 2.4.3), we gave the opportunity to the reorganization to happen if enough stress had been loaded in the facing cells. Initially, we wanted to assess whether the loaded stress could result in cell deformation. We thus developed a method to precisely measure cell lengths (see paragraph 2.2.4). Already in the in-line configuration, before performing the ablation, we noticed a curious phenomenon.

We compared the external pole-to-pole length [1] of the line formed by the cells in the in-line configuration (l_{1+2}) and the sum of cell lengths also in the in-line configuration ($l_1 + l_2$). Notations are explain in figure D.1. We systematically measured a difference $\epsilon = l_{1+2} - (l_1 + l_2)$ (see figure D.2). The average value of this difference is $\epsilon = 353 \pm 70$ nm. This is significant regarding the uncertainty on length measurements (on average 60 nm). To

1. The location of the poles was also determined precisely using the same principle as the length measurement method (see paragraph 2.2.4).

date, since ϵ is small (close or smaller than the diffraction limit), we cannot rule out the possibility of an artifact either due to our measurement method or to the imaging technique. Additional experiments would be required to validate this finding. In particular, fluorescent labels on membranes or inside the cytoplasm could provide hints about the origin of this phenomenon. Our current hypothesis is that we could be measuring the extension of the septum after the inner membranes of the two daughters separated.

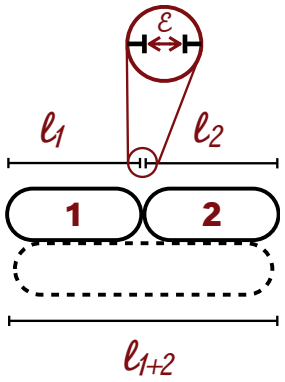

Figure D.1 – Length measurements before the eventual ablation-induced reorganization. The cell to be ablated is represented by a dashed line. Measured lengths refer to the short cells, denoted 1 and 2.

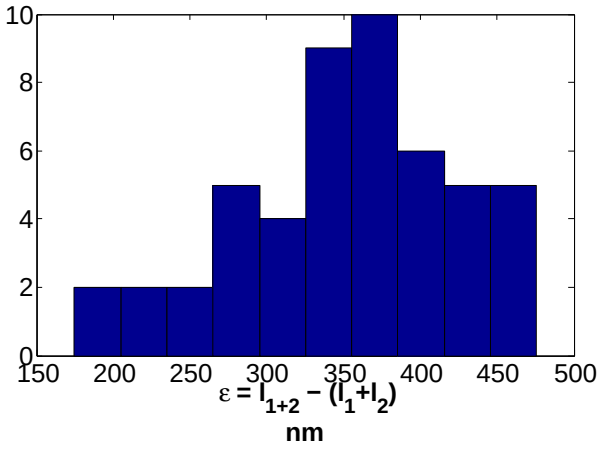

Figure D.2 – Estimation of ϵ.
Histogram of the difference (expressed in nm) between the external pole-to-pole distance l_{1+2} and the sum of individual cell lengths before ablation (in the in-line configuration). 50 experiments are displayed on this histogram.

D.2 Reflection Interference Contrast Microscopy

These experiments were performed with Delphine Débarre (DyFCoM, LIPhy).

Reflection Interference Contrast Microscopy (RICM) provides the opportunity to measure the distance between two close surfaces with a nanometer precision [221]. The technique relies on the detection of the light reflected by the two surfaces. If their distance is small enough (inferior to half the coherence length of the light source), the two beams will interfere. From intensity modulations, information on the distance between the two surfaces can be retrieved.

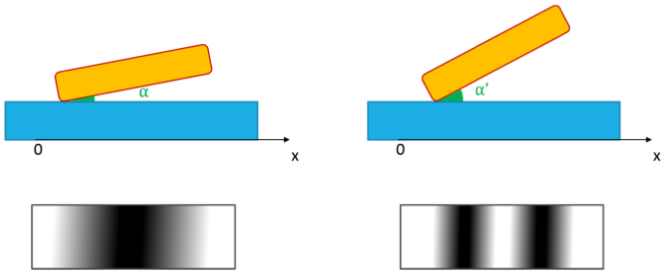

Figure D.3 – Principle of RIC microscopy.
For an almost flat bacterium, gray levels are dark inside the cell and white on the edges (left). When the bacterium is significantly tilted, an intensity modulation appears along the axis of the bacterium (right).

In our case, the two surfaces are the envelop of the bacterium and the glass slide. To a first approximation, *E. coli* cells can be considered as rigid rods. Consequently, a cell that forms an angle with the glass surface will display interference fringes (see figure D.3). Typically, the optical path difference separating two successive fringes corresponds to half the wavelength [2], 250 nm in our case.

We carried out two preliminary experiments using RICM to image *E. coli* microcolonies confined between an agarose gel and a glass slide (see appendix B.1). For small colonies (typically less than 10 cells), no fringes were observed. For comparison, a transition from black to white (half a fringe) from

2. This does not take into account the geometrical effect due to the inclination of the surface.

one pole of the cell to the other would mean that the white pole is around 125 nm higher than the black one. This would correspond to an angle of 1.2 ° between the bacterium and the glass surface. If bacteria appear black, their angle with the glass slide is thus inferior to 1.2 ° . As the colony grew larger, some bacteria displayed inclination that could relax a few minutes later. As growth proceeded, a larger number of bacteria appeared tilted and the corresponding angles increased. These experiments suggest that the appearance of the double layer (described in paragraph 3.4.2) may be the result of a continuous process.

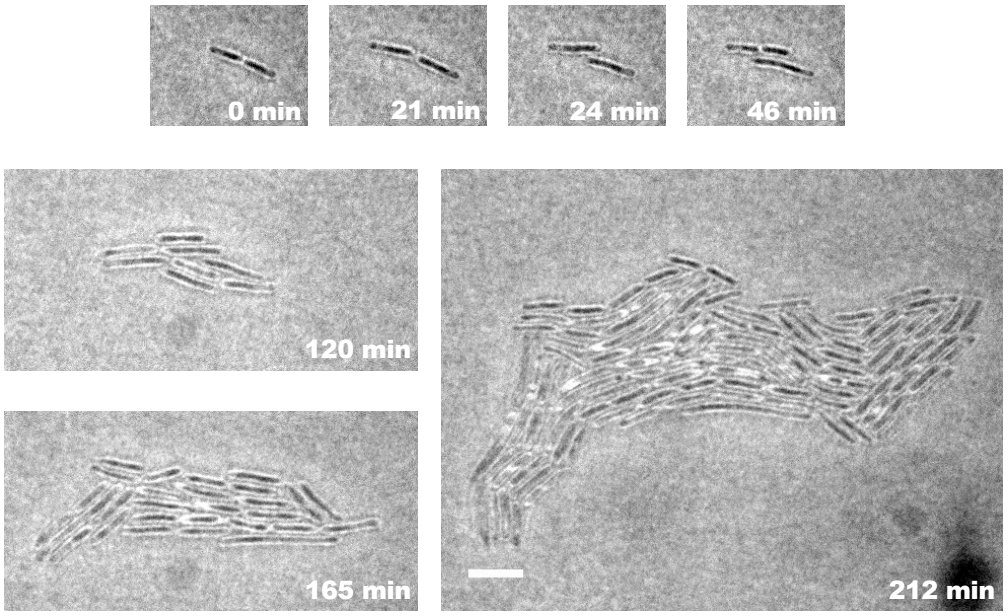

Figure D.4 – Preliminary RICM experiment.
Images show different times during the growth of an *E. coli* microcolony confined between an agarose gel and a glass slide. Gray levels are indicative of the distance between the cells and the glass substrate, which highlights zones where bacteria are pushed away from the substrate. The scale is the same for every image and scale bar is 5 μm.

Appendix E

French summary / Résumé en français

E.1 Résumé global

Ce travail nous a permis de proposer un cadre pour sonder la morphogenèse d'une micro-colonie bidimensionnelle. Plus particulièrement, nous avons exploré la manière dont les effets individuels de croissance et d'adhésion se combinaient au cours de la croissance de la micro-colonie. Nous avons montré (i) que l'adhésion de cellules isolées est asymétrique du fait d'un vieux pôle plus ancré et (ii) que l'allongement des bactéries peut induire des forces de poussée à l'intérieur des colonies. Dans la mesure où ces deux effets, combinés à l'échelle d'une micro-colonie, sont susceptibles de générer des contraintes mécaniques, nous avons développé une technique pour mesurer les forces d'adhésion résultantes à l'aide de substrats déformables. Nous avons ainsi démontré que des adhésions focales sont créées et rompues dynamiquement, avec un biais au vieux pôle des cellules. Nous avons aussi examiné le rôle de l'adhésion sur la forme des colonies. Nous avons montré que l'adhésion polaire était responsable de la transition d'un régime de croissance linéaire à un régime bidimensionnel qui est observée après la première division. Pour des colonies de taille plus importante, le niveau d'adhésion était aussi corrélé avec la forme globale des colonies. Enfin, l'adhésion est aussi impliquée dans la transition d'une colonie bidimensionnelle à une colonie tridimensionnelle. L'ensemble de ces résultats suggère que l'expression des adhésines ainsi que leur localisation à la surface des cellules pourraient permettre aux bactéries de moduler activement la forme du groupe dans lequel elles vivent.

E.2 Avant-propos

Bon nombre d'espèces s'organisent en communautés. Des troupeaux de gnous aux volées d'oiseaux ou aux meutes de loups, des villes humaines aux nids d'insectes, se regrouper requiert un certain niveau d'organisation, notamment pour accéder aux ressources extérieures. En effet, en vivant dans un groupe, ses membres peuvent bénéficier des interactions avec d'autres membres. A l'inverse, le fait d'avoir de nombreux individus au même endroit, ou même la proximité, influence la manière dont un individu va interagir avec l'environnement. Vu sous cet angle, la géométrie du groupe semble être déterminante pour la survie des membres qui le composent.

Les bactéries n'échappent pas à cette tendance et forment des colonies macroscopiques appelées biofilms. Ces communautés adoptent différentes formes selon les conditions environnementales et internes. Certaines caractéristiques morphologiques sont associées à une fonction particulière en terme d'accès aux ressources extérieures. Il est alors intéressant de comprendre comment une forme particulière émerge. Bien que les biologistes aient étudié cette question d'un point de vue biochimique, il ne semble pas exister à ce jour de cadre mécanique défini pour comprendre la formation et le développement de telles colonies.

Nous avons restreint notre travail à l'étude de micro-colonies monoclonales, confinées dans le plan et issues d'un unique bacille. Bien que cette situation soit simplifiée mécaniquement, nous avons observé des phénomènes mécaniques non triviaux dans cette configuration. En particulier, nous avons été surpris de voir que la forme finale des colonies ne reflétait pas la symétrie de ses composants élémentaires. Ce projet a vu le jour suite à des discussions concernant l'origine de la transition d'une bactérie s'allongeant linéairement à une colonie compacte et bidimensionnelle. Trois ans de travail ont transformé nos discussions en ce manuscrit. Le premier chapitre décrit le mode de vie en biofilm et les caractéristiques bactériennes susceptibles d'influencer la forme des colonies. Le second chapitre présente les techniques expérimentales que nous avons mis en place pour sonder les interactions mécaniques en jeu lors de la morphogenèse. Le troisième chapitre rassemble nos résultats et notre compréhension actuelle de la mécanique de croissance d'une microcolonie bactérienne. Enfin, les appendices proposent une description des souches utilisées, le détail des protocoles expérimentaux, les caractéristiques de croissance mesurées dans nos conditions et des expériences préliminaires qui alimentent encore nos discussions.

E.3 Chapitre 1 : Introduction

E.3.1 Le biofilm

Dans la nature, les bactéries peuvent nager individuellement ou se regrouper en biofilm à l'interface de deux milieux ou entre une surface et un milieu. Dans ce dernier cas, une bactérie adhère à la surface d'abord faiblement, puis plus solidement. Par division ou recrutement d'autres bactéries (de la même espèce ou non), un agrégat de cellules se forme. Il peut atteindre des tailles millimétriques en quelques heures. Lorsque le biofilm est mature, des bactéries peuvent s'en échapper pour retourner à un mode de vie planctonique et coloniser d'autres habitats. Au sein des biofilms, les bactéries sont moins vulnérables aux attaques environnementales : par exemple, un biofilm peut être jusqu'à 1000 fois plus tolérant aux antibiotiques que la même souche bactérienne en solution. Dans un biofilm, certaines bactéries sécrètent des biopolymères, ils forment une matrice qui donne au biofilm sa cohérence mécanique. La forme du biofilm dépend de certains facteurs environnementaux qui influencent, en particulier, la quantité de matrice sécrétée. Par ailleurs, bien qu'il constitue une entité mécanique cohérente, le biofilm est hétérogène chimiquement et biologiquement. Des gradients de nutriments s'établissent en raison de la localisation des sources, de la consommation ou de la production locale de certain nutriments et de la diffusion. Ces gradients résultent en un partitionnement du biofilm en zones où les bactéries sont dans des états métaboliques différents. Par exemple, elles ne produisent pas toutes de la matrice. On parle de variabilité phénotypique. Les biofilms sont ainsi spatialement structurés. Leur morphogenèse s'adapte dynamiquement de façon à réguler la position des cellules par rapport aux sources de nutriments, ce qui en retour influe sur les gradients chimiques présents dans le biofilm.

E.3.2 Le cycle cellulaire

Les bacilles sont des bactéries sphéro-cylindriques. Leur forme est maintenue par un cytosquelette (protéine MreB) et leur intégrité est assurée par un réseau de polymères, les peptidoglycans. Dans le cas de bactéries Gram-negatives, les peptidoglycans se situent entre les deux membranes lipidiques. Au cours d'un cycle cellulaire, les bacilles s'allongent et se divisent. Pour *Escherichia coli*, l'allongement s'effectue par ajout homogène de peptidoglycans le long de la paroi cellulaire. Seuls les pôles ne sont pas affectés par ces ajouts. La phase de septation est coordonnée par la protéine FtsZ qui est responsable de la constriction de la bactérie en son milieu.

E.3.3 L'adhésion

La surface des bactéries est recouverte de macro-molécules. Les protéines impliquées dans l'adhésion sont appelées adhésines. C'est le cas des fimbriae de type I, de l'antigène 43, des curlis et des flagelles pour *E. coli*. Les polysaccharides sont des exemples de macro-molécules non protéiques probablement impliquées dans l'adhésion. Deux types d'adhésion peuvent être envisagées : l'adhésion à un substrat et l'adhésion entre cellules. Les propriétés adhésives peuvent être étudiées à différentes échelles (biofilm, bactérie individuelle ou adhésine isolée). Plusieurs techniques (angle de contact, centrifugation, flux, AFM, pinces optiques) ont permis de donner des ordres de grandeurs des forces mises en jeu : de l'ordre du nN à l'échelle du biofilm, de la centaine de pN à l'échelle de cellule et de la dizaine de pN pour une adhésine isolée. Par ailleurs, les propriétés d'adhésion avec un substrat dépendent des propriétés chimiques, biologiques (spécificité de certaines adhésines avec des biomolécules particulières) et mécaniques de ce dernier.

E.3.4 Mécanique de croissance d'une micro-colonie bactérienne

Il a été montré que l'allongement et l'adhésion de bactéries individuelles peuvent générer des contraintes mécaniques. En particulier, des instabilités de type flambage ont été observées dans des colonies bidimensionnelles et matures. Elles ont été attribuées au fait que les bactéries poussent et s'ordonnent sous l'effet des interactions de contact. En revanche, ces études ne considèrent pas l'adhésion avec le substrat dans l'équilibre des forces. Nous avons choisi d'étudier spécifiquement la contribution de l'adhésion avec le substrat. Nous nous sommes restreints à l'étude de micro-colonies confinées en deux dimensions afin (i) de pouvoir suivre individuellement toutes les bactéries et de (ii) nous placer dans une situation simplifiée tant sur le plan mécanique que biologique.

E.4 Chapitre 2 : Matériels et méthodes

La plupart des expériences que nous avons menées consistent en l'acquisition à intervalle régulier (de quelques secondes à quelques minutes) d'images d'une micro-colonies se développant entre un gel d'agarose et une lamelle de verre. L'analyse de telles images nous permet d'avoir accès au masque de la colonie, au masque de chaque bactérie individuellement et au lignage. À partir de ces informations, il nous a été possible de suivre par exemple

la position, la taille, l'orientation, le mouvement, l'âge de différentes bactéries. Nous avons par ailleurs mené des expériences d'ablations laser dans différentes configurations. Enfin, nous avons adapté la microscopie à force de traction, utilisée typiquement pour des cellules eukaryotes, afin de quantifier les forces exercées par des micro-colonies bactériennes confinées sur leur substrat. Cette technique permet de mesurer les forces d'adhésion appliquées sur un substrat mou (gel de poly-acrylamide dans notre cas) en suivant sa déformation à l'aide de marqueurs fluorescents. Après modification du protocole expérimental pour satisfaire aux besoins de nos expériences, nous avons calibré la stabilité de nos gels de poly-acrylamide en terme de bruit sur les mesures de forces. Le calcul des forces a aussi été adapté à notre situation expérimentale.

E.5 Chapitre 3 : Résultats et interprétations

E.5.1 Stade 1 à 2 cellules

De façon surprenante, le centre de masse d'une bactérie isolée semble se déplacer pendant sa croissance. L'allongement de la paroi cellulaire étant homogène, cela suggère que l'adhésion à l'échelle de la bactérie individuelle n'est pas uniforme. Nous avons défini un paramètre d'asymétrie en estimant la pente du déplacement du centre de masse (projeté sur l'axe de la bactérie) en fonction de l'allongement. Nous avons analysé la distribution de cette quantité pour des souches mutantes de la bactérie *E. coli* présentant des propriétés d'adhésion différentes. Cela nous a permis de montrer que, à l'échelle d'une population, la moyenne du paramètre d'asymétrie augmentait lorsque les curli étaient sur-exprimées et diminuait en cas de délétion d'une ou plusieurs adhésines. Une analyse de ce phénomène semble indiquer que pour pouvoir adhérer tout en s'allongeant, l'adhésion d'une cellule doit être focale. Ainsi, l'asymétrie impose que la position de ces adhésions focales soit asymétrique. La dissymétrie entre vieux et nouveau pôle pourrait permettre d'expliquer cette asymétrie, auquel cas le vieux pôle serait *a priori* plus ancré que le nouveau.

Pour mettre en évidence un éventuel biais quant à l'orientation de l'asymétrie, nous avons effectué des expériences d'ablations laser nous permettant de conserver une cellule isolée sans modifier son taux de croissance. Après chaque division, une des deux cellules filles était supprimée par ablation. En effectuant les ablations toujours du même côté, nous avons montré que le vieux pôle était toujours plus ancré et que le paramètre d'asymétrie semblait saturer en moins de deux générations. L'ancrage systématique au vieux pôle

a été observé pour des expériences contrôles où nous changions de côté à chaque ablation.

Lorsque la croissance n'est pas perturbée, après la première division, les deux cellules filles glissent l'une contre l'autre et se réorganisent parallèlement. Ce phénomène est rapide comparé au temps de division mais son temps caractéristique est distribué. Cette réorganisation semble plus rapide lorsque la cellule mère présentait une asymétrie importante. À l'inverse, la rapidité de la réorganisation ne semble pas corrélée à la déformation du gel le long de l'axe de la bactérie entre le moment où la bactérie a été déposée sur le gel et le moment de la réorganisation. Bien que la force de confinement impose que la configuration des cellules après réorganisation est énergétiquement plus favorable que la configuration précédant la réorganisation, les observations précédentes suggèrent que la force de confinement du gel n'est pas l'élément déclencheur de la réorganisation. À l'inverse, il semble plus probable qu'une instabilité de type flambage soit à l'origine de la réorganisation. En effet, avant la réorganisation, les vieux pôles sont situés aux extrémités de la ligne formée par les bactéries filles. Lorsqu'ils s'ancrent, les cellules s'allongent l'une contre l'autre créant l'instabilité.

E.5.2 Dynamique à l'échelle de la cellule unique et organisation de la micro-colonie au cours de la croissance bidimensionnelle

Pour les souches sauvages de *Escherichia coli* et *Pseudomonas aeruginosa*, il apparait que les taux de croissance individuels sont homogènes au sein de la colonie. L'analyse des positions et déplacements des bactéries indique qu'elles se déplacent radialement et d'autant plus lorsqu'elles sont en périphérie. De plus, l'amplitude moyenne des déplacements augmente au cours du temps. Ces observations suggèrent que les bactéries centrales poussent les bactéries périphériques afin de pouvoir s'allonger.

Par ailleurs, le rapport d'aspect des colonies diminue puis augmente. L'ordre nématique au sein de la colonie décroît au cours du temps et la corrélation angulaire diminue avec la distance entre les bactéries.

E.5.3 Adhésion cellule-substrat lors du développement de la micro-colonie

Afin de comprendre comment poussée et adhésion s'articulent, nous avons mesuré les forces exercées par une colonie sur son substrat au cours de sa croissance. Bien que le champ de force soit très hétérogène et fluctuant dans

le temps, la force totale développée par la colonie sur son substrat croît linéairement avec l'aire de la colonie. À l'inverse, la force maximale sature suggérant que les adhésions se cassent sous l'effet de la poussée et que la force de saturation correspond à la charge maximale que peut soutenir une adhésion. Ces hypothèses sont validées par une analyse locale de la force mesurée sous les pôles des bactéries. La comparaison des forces aux nouveaux et aux vieux pôles indique que l'asymétrie mise en évidence au stade une cellule (cf. paragraphe E.5.1) persiste à des stades de croissance avancée des micro-colonies. Enfin, une étude comparative de souches mutantes de *E. coli* et *P. aeruginosa* montre que le niveau de force mesuré dépend du niveau d'expression des curlis et de la présence des adhésines et polysaccharides. Par ailleurs, plus généralement, le niveau de force est plus important à 34 ° C qu'à 28 ° C.

E.5.4 Contribution de l'adhésion à la morphologie des micro-colonies

Afin d'évaluer l'effet d'adhésions plus ou moins fortes sur la morphologie des colonies, nous avons évalué le rapport d'aspect moyen de micro-colonies formées par différents mutants d'adhésion de la souche *E. coli*. De manière générale, les micro-colonies sont plus allongées si des adhésines sont délétées du génôme de la souche mutante. Le rapport d'aspect semble également dépendre du type de confinement et de la température à laquelle les bactéries sont cultivées. Cependant, inversement à la tendance générale, en l'absence de curlis, les colonies formées sont plus compactes. Ceci suggère que l'adhésion entre bactéries, en particulier par l'intermédiaire des curlis, pourrait aussi influencer l'allongement des micro-colonies, ce qui requerrait une étude plus approfondie.

L'adhésion a aussi un effet visible sur le passage d'une micro-colonie bidimensionnelle à une colonie se développant en trois dimensions. L'étude de différents mutants d'adhésion, couplée ou non à des mesure de forces, montre que plus une souche est adhésive, moins la colonie s'étalera en 2D avant de passer à 3D. Cette observation suggère que la transition subvient lorsque le confinement des bactéries du centre de la colonies est plus important latéralement (par l'ensemble des bactéries ancrés entre elles et la périphérie) que verticalement (par le gel). Ainsi, il est alors énergétiquement préférable pour elles de sortir de la mono-couche et de démarrer la croissance à 3D. Pour finir, nous nous sommes placés dans une situation où il est plus avantageux métaboliquement pour les bactéries de former des colonies compactes à 3D : *P. aeruginosa* en l'absence de fer. On constate (i) que les micro-colonies

s'étalent moins avant de former des colonies à 3D et (ii) que ce changement dans la morphogenèse provient d'une augmentation drastique des forces d'adhésions développées sur le substrat : elles ne semblent plus pouvoir être rompues par les forces de poussée. Cet exemple suggère que pour une souche donnée, moduler la force des adhésions est un moyen d'adapter sa morphologie aux conditions environnementales.

E.6 Conclusion et perspectives

Les bactéries forment des biofilms au sein desquels elles sont moins vulnérables aux agressions extérieures. Ainsi, vivre dans un biofilm confère un avantage évolutif par rapport à un mode de vie isolé. Lorsqu'un biofilm se développe sur une surface solide, les bactéries s'y attachent fermement. Au cours de cette thèse, nous avons cherché à comprendre comment des bactéries attachées à un substrat pouvaient se développer tout en restant en contact avec la surface.

Pour des bactéries isolées, nous avons montré que la croissance n'est pas symétrique par rapport au centre de masse, malgré une élongation homogène de la paroi cellulaire. Cela suggère que l'adhésion est asymétrique à l'échelle d'une cellule. Pour évaluer l'orientation de cette asymétrie, nous avons mené des expériences d'ablation laser qui nous ont permis de suivre des cellules isolées pendant plusieurs générations. Nous avons montré que l'asymétrie provenait d'un vieux pôle systématiquement plus ancré que le nouveau. De plus, cette asymétrie s'établit en moins de deux générations suite à la mise en contact de la bactérie avec la surface. Nous avons mis en évidence le fait que cette asymétrie est importante pour la transition d'une bactérie s'allongeant linéairement à une colonie compacte se développant en deux dimensions. En effet, après la première division, les vieux pôles sont situés aux extrémités de la ligne formée par les deux cellules filles. Elles s'allongent donc l'une vers l'autre en raison des ancrages aux vieux pôles. Cette situation instable provoque le glissement des deux bactéries l'une contre l'autre après la septation.

Par ailleurs, nous avons montré que, au sein d'une colonie, les taux de croissance individuels sont homogènes. Combinées, ces élongations individuelles génèrent des forces de poussée radiales susceptibles d'interférer avec les adhésions cellulaires. Pour comprendre comment adhésion et élongation s'équilibrent à l'échelle d'une micro-colonie, nous avons développé une technique de microscopie permettant de mesurer les forces transmises par des

bactéries à leur substrat. Des zones de forte contrainte apparaissent et disparaissent au cours de la croissance. La force totale exercée par une colonie augmente linéairement avec le nombre de cellules, alors que la force maximale observée localement semble saturer. Nous avons interprété cette saturation comme une signature de la rupture de lien adhésifs sous l'effet des forces de poussée dues aux allongements. Cette hypothèse est corroborée par l'étude de plusieurs mutants d'adhésion qui présentent des niveaux de saturation différents. Le niveau de saturation nous a ainsi permis de quantifier la force d'adhésion de certaines adhésines de *E. coli* and *P. aeruginosa*. Pour la souche sauvage de *E. coli*, nous avons mesuré des forces de l'ordre de 80 pN, conformément à ce qui avait été rapporté en utilisant d'autres techniques.

Enfin, en utilisant des souches mutantes, nous avons montré que les propriétés d'adhésion influencent la morphologie des micro-colonies. En effet, lorsque l'adhésion est affaiblie, les colonies sont plus allongées et ne deviennent tridimensionnelles que pour des aires plus grandes. L'ensemble de ces résultats suggère que l'expression des adhésines et leurs positions sur la paroi cellulaire pourraient être utilisées par les bactéries dans le but de moduler activement leurs interactions avec l'environnement d'une part, et avec leurs voisins d'autre part, pour réguler la forme du groupe dans lequel elles vivent.

Par ailleurs, nos résultats semblent indiquer que d'autres forces entrent en jeu dans la morphogenèse de ces micro-colonies. En effet, la plupart des adhésines sont impliquées dans les interactions entre cellules en plus de jouer un rôle dans l'adhésion avec le substrat. En particulier, la contribution des curlis n'est que partiellement expliquée si on considère uniquement l'adhésion cellule-substrat. Une quantification de l'interaction cellule-cellule permettrait ainsi de comprendre plus exhaustivement la morphogenèse des micro-colonies bactériennes.

Bibliography

[1] Chih-Horng Kuo, Nancy A. Moran, and Howard Ochman. The consequences of genetic drift for bacterial genome complexity. *Genome Res.*, 19(8):1450–1454, August 2009.

[2] Michael T. Madigan and Thomas D. Brock. *Brock biology of microorganisms*. Boston : Benjamin Cummings, c2012., 2012.

[3] William B. Whitman, David C. Coleman, and William J. Wiebe. Prokaryotes: The unseen majority. *PNAS*, 95(12):6578–6583, June 1998.

[4] Christopher Dye. After 2015: infectious diseases in a new era of health and development. *Philos. Trans. R. Soc. Lond., B, Biol. Sci.*, 369(1645):20130426, 2014.

[5] Sarah E. Rollins, MD, Sean M. Rollins, PhD, and Edward T. Ryan, MD. Yersinia pestis and the Plague. *Pathology Patterns Reviews*, 119(0):78–85, June 2003.

[6] William P. Robins and John J. Mekalanos. Genomic science in understanding cholera outbreaks and evolution of Vibrio cholerae as a human pathogen. *Curr. Top. Microbiol. Immunol.*, 379:211–229, 2014.

[7] A. K. Siddique and Richard Cash. Cholera outbreaks in the classical biotype era. *Curr. Top. Microbiol. Immunol.*, 379:1–16, 2014.

[8] Surendra K. Sharma and Alladi Mohan. Tuberculosis: From an incurable scourge to a curable disease - journey over a millennium. *Indian J. Med. Res.*, 137(3):455–493, March 2013.

[9] Peter J. Turnbaugh, Micah Hamady, Tanya Yatsunenko, Brandi L. Cantarel, Alexis Duncan, Ruth E. Ley, Mitchell L. Sogin, William J. Jones, Bruce A. Roe, Jason P. Affourtit, Michael Egholm, Bernard Henrissat, Andrew C. Heath, Rob Knight, and Jeffrey I. Gordon. A core gut microbiome in obese and lean twins. *Nature*, 457(7228):480–484, January 2009.

[10] Benjamin P. Willing, Anjalee Vacharaksa, Matthew Croxen, Teerawat Thanachayanont, and B. Brett Finlay. Altering Host Resistance to Infections through Microbial Transplantation. *PLoS ONE*, 6(10):e26988, October 2011.

[11] Rochellys Diaz Heijtz, Shugui Wang, Farhana Anuar, Yu Qian, Britta Björkholm, Annika Samuelsson, Martin L. Hibberd, Hans Forssberg, and Sven Pettersson. Normal gut microbiota modulates brain development and behavior. *Proc. Natl. Acad. Sci. U.S.A.*, 108(7):3047–3052, February 2011.

[12] Largus T. Angenent, Khursheed Karim, Muthanna H. Al-Dahhan, Brian A. Wrenn, and Rosa Domíguez-Espinosa. Production of bioenergy and biochemicals from industrial and agricultural wastewater. *Trends in Biotechnology*, 22(9):477–485, September 2004.

[13] Yong Jae Lee and Ki Jun Jeong. Challenges to production of antibodies in bacteria and yeast. *J. Biosci. Bioeng.*, April 2015.

[14] Wanmeng Mu, Tao Zhang, and Bo Jiang. An overview of biological production of L-theanine. *Biotechnol. Adv.*, April 2015.

[15] Artun Sukan, Ipsita Roy, and Tajalli Keshavarz. Dual production of biopolymers from bacteria. *Carbohydrate Polymers*, 126:47–51, 2015.

[16] Bernard R. Glick. The enhancement of plant growth by free-living bacteria. *Can. J. Microbiol.*, 41(2):109–117, 1995.

[17] Joris Am Missotten, Joris Michiels, Jeroen Degroote, and Stefaan De Smet. Fermented liquid feed for pigs: an ancient technique for the future. *J Anim Sci Biotechnol*, 6(1):4, 2015.

[18] Diego O Serra and Regine Hengge. Stress responses go three dimensional – the spatial order of physiological differentiation in bacterial macrocolony biofilms. *Environ Microbiol*, 16(6):1455–1471, June 2014.

[19] Luanne Hall-Stoodley, J. William Costerton, and Paul Stoodley. Bacterial biofilms: from the Natural environment to infectious diseases. *Nat Rev Micro*, 2(2):95–108, 2004.

[20] Frances Westall, Maarten J de Wit, Jesse Dann, Sjerry van der Gaast, Cornel E. J de Ronde, and Dane Gerneke. Early Archean fossil bacteria and biofilms in hydrothermally-influenced sediments from the Barberton greenstone belt, South Africa. *Precambrian Research*, 106(1–2):93–116, 2001.

[21] Birger Rasmussen. Filamentous microfossils in a 3,235-million-year-old volcanogenic massive sulphide deposit. *Nature*, 405(6787):676–679, 2000.

[22] Claude E. Zobell. The Effect of Solid Surfaces upon Bacterial Activity. *J Bacteriol*, 46(1):39–56, July 1943.

[23] Tom J. Battin, Anton Wille, Birgit Sattler, and Roland Psenner. Phylogenetic and Functional Heterogeneity of Sediment Biofilms along Environmental Gradients in a Glacial Stream. *Appl Environ Microbiol*, 67(2):799–807, February 2001.

[24] M. E. Davey and G. A. O'toole. Microbial biofilms: from ecology to molecular genetics. *Microbiol. Mol. Biol. Rev.*, 64(4):847–867, December 2000.

[25] S. W. Wessel, Y. Chen, A. Maitra, E. R. van den Heuvel, A. M. Slomp, H. J. Busscher, and H. C. van der Mei. Adhesion forces and composition of planktonic and adhering oral microbiomes. *J. Dent. Res.*, 93(1):84–88, January 2014.

[26] Oana Ciofu, Tim Tolker-Nielsen, Peter Østrup Jensen, Hengzhuang Wang, and Niels Høiby. Antimicrobial resistance, respiratory tract infections and role of biofilms in lung infections in cystic fibrosis patients. *Adv. Drug Deliv. Rev.*, December 2014.

[27] Angela H. Nobbs, Richard J. Lamont, and Howard F. Jenkinson. Streptococcus adherence and colonization. *Microbiol. Mol. Biol. Rev.*, 73(3):407–450, September 2009.

[28] Iolanda Francolini and Gianfranco Donelli. Prevention and control of biofilm-based medical-device-related infections. *FEMS Immunology & Medical Microbiology*, 59(3):227–238, 2010.

[29] Michael P. Schultz and Geoffrey W. Swain. The influence of biofilms on skin friction drag. *Biofouling*, 15(1-3):129–139, 2000.

[30] Masaaki Morikawa. Beneficial biofilm formation by industrial bacteria Bacillus subtilis and related species. *Journal of Bioscience and Bioengineering*, 101(1):1–8, January 2006.

[31] T. Shaw, M. Winston, C. J. Rupp, I. Klapper, and P. Stoodley. Commonality of Elastic Relaxation Times in Biofilms. *Phys. Rev. Lett.*, 93(9):098102, 2004.

[32] Hans-Curt Flemming and Jost Wingender. The biofilm matrix. *Nat. Rev. Microbiol.*, 8(9):623–633, September 2010.

[33] J. W. Costerton, Z. Lewandowski, D. E. Caldwell, D. R. Korber, and H. M. Lappin-Scott. Microbial biofilms. *Annu. Rev. Microbiol.*, 49:711–745, 1995.

[34] T. F. Mah and G. A. O'Toole. Mechanisms of biofilm resistance to antimicrobial agents. *Trends Microbiol.*, 9(1):34–39, January 2001.

[35] P. Gilbert, J. Das, and I. Foley. Biofilm susceptibility to antimicrobials. *Adv. Dent. Res.*, 11(1):160–167, April 1997.

[36] Algirdas J. Jesaitis, Michael J. Franklin, Deborah Berglund, Maiko Sasaki, Connie I. Lord, Justin B. Bleazard, James E. Duffy, Haluk Beyenal, and Zbigniew Lewandowski. Compromised host defense on Pseudomonas aeruginosa biofilms: characterization of neutrophil and biofilm interactions. *J. Immunol.*, 171(8):4329–4339, October 2003.

[37] Tyler D. Scherr, Cortney E. Heim, John M. Morrison, and Tammy Kielian. Hiding in Plain Sight: Interplay between Staphylococcal Biofilms and Host Immunity. *Front Immunol*, 5:37, 2014.

[38] M. O. Elasri and R. V. Miller. Study of the response of a biofilm bacterial community to UV radiation. *Appl. Environ. Microbiol.*, 65(5):2025–2031, May 1999.

[39] E. M. Espeland and R. G. Wetzel. Complexation, Stabilization, and UV Photolysis of Extracellular and Surface-Bound Glucosidase and Alkaline Phosphatase: Implications for Biofilm Microbiota. *Microb. Ecol.*, 42(4):572–585, December 2001.

[40] Woo-Suk Chang, Martijn van de Mortel, Lindsey Nielsen, Gabriela Nino de Guzman, Xiaohong Li, and Larry J. Halverson. Alginate production by Pseudomonas putida creates a hydrated microenvironment and contributes to biofilm architecture and stress tolerance under water-limiting conditions. *J. Bacteriol.*, 189(22):8290–8299, November 2007.

[41] Karol McNeill and I. R. Hamilton. Acid tolerance response of biofilm cells of Streptococcus mutans. *FEMS Microbiol. Lett.*, 221(1):25–30, April 2003.

[42] Joe J. Harrison, Howard Ceri, and Raymond J. Turner. Multimetal resistance and tolerance in microbial biofilms. *Nat. Rev. Microbiol.*, 5(12):928–938, December 2007.

[43] Sandrine Koechler, Julien Farasin, Jessica Cleiss-Arnold, and Florence Arsène-Ploetze. Toxic metal resistance in biofilms: Diversity of microbial responses and their evolution. *Res. Microbiol.*, April 2015.

[44] Carsten Matz, Diane McDougald, Ana Maria Moreno, Pui Yi Yung, Fitnat H. Yildiz, and Staffan Kjelleberg. Biofilm formation and phenotypic variation enhance predation-driven persistence of Vibrio cholerae. *Proc. Natl. Acad. Sci. U.S.A.*, 102(46):16819–16824, November 2005.

[45] P. Stoodley, I. Dodds, J.d. Boyle, and H.m. Lappin-Scott. Influence of hydrodynamics and nutrients on biofilm structure. *Journal of Applied Microbiology*, 85(S1):19S–28S, 1998.

[46] Mikkel Klausen, Arne Heydorn, Paula Ragas, Lotte Lambertsen, Anders Aaes-Jørgensen, Søren Molin, and Tim Tolker-Nielsen. Biofilm formation by Pseudomonas aeruginosa wild type, flagella and type IV pili mutants. *Molecular Microbiology*, 48(6):1511–1524, 2003.

[47] Ehud Banin, Michael L. Vasil, and E. Peter Greenberg. Iron and Pseudomonas aeruginosa biofilm formation. *Proc Natl Acad Sci U S A*, 102(31):11076–11081, August 2005.

[48] Christopher P. Kempes, Chinweike Okegbe, Zwoisaint Mears-Clarke, Michael J. Follows, and Lars E. P. Dietrich. Morphological optimization for access to dual oxidants in biofilms. *Proc. Natl. Acad. Sci. U.S.A.*, 111(1):208–213, January 2014.

[49] Iztok Dogsa, Mojca Brloznik, David Stopar, and Ines Mandic-Mulec. Exopolymer Diversity and the Role of Levan in Bacillus subtilis Biofilms. *PLoS ONE*, 8(4), 2013.

[50] Glud, Ramsing, and Revsbech. Photosynthesis and Photosynthesis-Coupled Respiration in Natural Biofilms Quantified with Oxygen Microsensors. *J. Phycol.*, 28(1):51–60, February 1992.

[51] A Schramm, L H Larsen, N P Revsbech, N B Ramsing, R Amann, and K H Schleifer. Structure and function of a nitrifying biofilm as determined by in situ hybridization and the use of microelectrodes. *Appl Environ Microbiol*, 62(12):4641–4647, December 1996.

[52] Karen D. Xu, Philip S. Stewart, Fuhu Xia, Ching-Tsan Huang, and Gordon A. McFeters. Spatial Physiological Heterogeneity in Pseudomonas aeruginosa Biofilm Is Determined by Oxygen Availability. *Appl. Environ. Microbiol.*, 64(10):4035–4039, October 1998.

[53] Suriani Abdul Rani, Betsey Pitts, Haluk Beyenal, Raaja Angathevar Veluchamy, Zbigniew Lewandowski, William M. Davison, Kelli Buckingham-Meyer, and Philip S. Stewart. Spatial Patterns of DNA Replication, Protein Synthesis, and Oxygen Concentration within Bacterial Biofilms Reveal Diverse Physiological States. *J. Bacteriol.*, 189(11):4223–4233, June 2007.

[54] Jurrien M. Vroom, Kees J. De Grauw, Hans C. Gerritsen, David J. Bradshaw, Philip D. Marsh, G. Keith Watson, John J. Birmingham, and Clive Allison. Depth Penetration and Detection of pH Gradients in Biofilms by Two-Photon Excitation Microscopy. *Appl. Environ. Microbiol.*, 65(8):3502–3511, August 1999.

[55] Philip S. Stewart. Diffusion in Biofilms. *J. Bacteriol.*, 185(5):1485–1491, March 2003.

[56] R. Kolter, Da Siegele, and A. Tormo. The Stationary-Phase of the Bacterial Life-Cycle. *Annu. Rev. Microbiol.*, 47:855–874, 1993.

[57] Erin Werner, Frank Roe, Amandine Bugnicourt, Michael J. Franklin, Arne Heydorn, Søren Molin, Betsey Pitts, and Philip S. Stewart. Stratified Growth in Pseudomonas aeruginosa Biofilms. *Appl. Environ. Microbiol.*, 70(10):6188–6196, October 2004.

[58] Kerry S. Williamson, Lee A. Richards, Ailyn C. Perez-Osorio, Betsey Pitts, Kathleen McInnerney, Philip S. Stewart, and Michael J. Franklin. Heterogeneity in Pseudomonas aeruginosa Biofilms Includes Expression of Ribosome Hibernation Factors in the Antibiotic-Tolerant Subpopulation and Hypoxia-Induced Stress Response in the Metabolically Active Population. *J. Bacteriol.*, 194(8):2062–2073, April 2012.

[59] Diego O. Serra, Anja M. Richter, Gisela Klauck, Franziska Mika, and Regine Hengge. Microanatomy at Cellular Resolution and Spatial Order of Physiological Differentiation in a Bacterial Biofilm. *mBio*, 4(2):e00103–13, May 2013.

[60] Hera Vlamakis, Claudio Aguilar, Richard Losick, and Roberto Kolter. Control of cell fate by the formation of an architecturally complex bacterial community. *Genes Dev*, 22(7):945–953, April 2008.

[61] Daniel López, Hera Vlamakis, Richard Losick, and Roberto Kolter. Cannibalism enhances biofilm development in Bacillus subtilis. *Molecular Microbiology*, 74(3):609–618, November 2009.

[62] J. Adler and Bonnie Templeton. The Effect of Environmental Conditions on the Motility of Escherichia coli. *J Gen Microbiol*, 46(2):175–184, February 1967.

[63] C. D. Amsler, M. Cho, and P. Matsumura. Multiple factors underlying the maximum motility of Escherichia coli as cultures enter post-exponential growth. *J. Bacteriol.*, 175(19):6238–6244, October 1993.

[64] Mingzhu Liu, Tim Durfee, Julio E. Cabrera, Kai Zhao, Ding J. Jin, and Frederick R. Blattner. Global transcriptional programs reveal a carbon source foraging strategy by Escherichia coli. *J. Biol. Chem.*, 280(16):15921–15927, April 2005.

[65] R. Lange and R. Hengge-Aronis. Growth phase-regulated expression of bolA and morphology of stationary-phase Escherichia coli cells are controlled by the novel sigma factor sigma S. *J. Bacteriol.*, 173(14):4474–4481, July 1991.

[66] Diego O. Serra, Anja M. Richter, and Regine Hengge. Cellulose as an Architectural Element in Spatially Structured Escherichia coli Biofilms. *J. Bacteriol.*, 195(24):5540–5554, December 2013.

[67] Christina Pesavento, Gisela Becker, Nicole Sommerfeldt, Alexandra Possling, Natalia Tschowri, Anika Mehlis, and Regine Hengge. Inverse regulatory coordination of motility and curli-mediated adhesion in Escherichia coli. *Genes Dev*, 22(17):2434–2446, September 2008.

[68] Eric Potvin, François Sanschagrin, and Roger C. Levesque. Sigma factors in Pseudomonas aeruginosa. *FEMS Microbiol. Rev.*, 32(1):38–55, January 2008.

[69] Mary Jo Kirisits, Lynne Prost, Melissa Starkey, and Matthew R. Parsek. Characterization of Colony Morphology Variants Isolated from Pseudomonas aeruginosa Biofilms. *Appl. Environ. Microbiol.*, 71(8):4809–4821, August 2005.

[70] Blaise R. Boles, Matthew Thoendel, and Pradeep K. Singh. Self-generated diversity produces "insurance effects" in biofilm communities. *PNAS*, 101(47):16630–16635, November 2004.

[71] Philip S. Stewart and Michael J. Franklin. Physiological heterogeneity in biofilms. *Nat Rev Micro*, 6(3):199–210, March 2008.

[72] P. Lebaron, P. Bauda, M. C. Lett, Y. Duval-Iflah, P. Simonet, E. Jacq, N. Frank, B. Roux, B. Baleux, G. Faurie, J. C. Hubert, P. Normand, D. Prieur, S. Schmitt, and J. C. Block. Recombinant plasmid mobilization between E. coli strains in seven sterile microcosms. *Can. J. Microbiol.*, 43(6):534–540, June 1997.

[73] B. B. Christensen, C. Sternberg, J. B. Andersen, L. Eberl, S. Moller, M. Givskov, and S. Molin. Establishment of new genetic traits in a microbial biofilm community. *Appl. Environ. Microbiol.*, 64(6):2247–2255, June 1998.

[74] A. P. Roberts, J. Pratten, M. Wilson, and P. Mullany. Transfer of a conjugative transposon, Tn5397 in a model oral biofilm. *FEMS Microbiol. Lett.*, 177(1):63–66, August 1999.

[75] P. Stoodley, K. Sauer, D. G. Davies, and J. W. Costerton. Biofilms as Complex Differentiated Communities. *Annual Review of Microbiology*, 56(1):187–209, 2002.

[76] Chris W. Michiels Rob Van Houdt. Role of bacterial cell surface structures in Escherichia coli biofilm formation. *Research in microbiology*, 156(5-6):626–33, 2005.

[77] Don Monroe. Looking for chinks in the armor of bacterial biofilms. *PLoS Biol.*, 5(11):e307, November 2007.

[78] Russell D. Monds and George A. O'Toole. The developmental model of microbial biofilms: ten years of a paradigm up for review. *Trends in Microbiology*, 17(2):73–87, 2009.

[79] Matthew T. Cabeen and Christine Jacobs-Wagner. Bacterial cell shape. *Nat Rev Micro*, 3(8):601–610, 2005.

[80] L. G. Burman, J. Raichler, and J. T. Park. Evidence for diffuse growth of the cylindrical portion of the Escherichia coli murein sacculus. *J. Bacteriol.*, 155(3):983–988, September 1983.

[81] Miguel A. De Pedro, Heinz Schwarz, and Arthur L. Koch. Patchiness of murein insertion into the sidewall of Escherichia coli. *Microbiology*, 149(7):1753–1761, July 2003.

[82] Miguel A. de Pedro, Christoph G. Grünfelder, and Heinz Schwarz. Restricted Mobility of Cell Surface Proteins in the Polar Regions of Escherichia coli. *J Bacteriol*, 186(9):2594–2602, May 2004.

[83] Richard A. Daniel and Jeff Errington. Control of Cell Morphogenesis in Bacteria: Two Distinct Ways to Make a Rod-Shaped Cell. *Cell*, 113(6):767–776, 2003.

[84] Michal Letek, María Fiuza, Efrén Ordóñez, Almudena F. Villadangos, Astrid Ramos, Luís M. Mateos, and José A. Gil. Cell growth and cell division in the rod-shaped actinomycete Corynebacterium glutamicum. *Antonie Van Leeuwenhoek*, 94(1):99–109, June 2008.

[85] Pamela J. B. Brown, Miguel A. de Pedro, David T. Kysela, Charles Van der Henst, Jinwoo Kim, Xavier De Bolle, Clay Fuqua, and Yves V. Brun. Polar growth in the Alphaproteobacterial order Rhizobiales. *Proc. Natl. Acad. Sci. U.S.A.*, 109(5):1697–1701, January 2012.

[86] David E. Nelson and Kevin D. Young. Contributions of PBP 5 anddd-Carboxypeptidase Penicillin Binding Proteins to Maintenance of Cell Shape in Escherichia coli. *J. Bacteriol.*, 183(10):3055–3064, May 2001.

[87] Laura J. F. Jones, Rut Carballido-López, and Jeffery Errington. Control of Cell Shape in Bacteria: Helical, Actin-like Filaments in Bacillus subtilis. *Cell*, 104(6):913–922, March 2001.

[88] Rainer M. Figge, Arun V. Divakaruni, and James W. Gober. MreB, the cell shape-determining bacterial actin homologue, co-ordinates cell wall morphogenesis in Caulobacter crescentus. *Molecular Microbiology*, 51(5):1321–1332, March 2004.

[89] Trine Nilsen, Arthur W. Yan, Gregory Gale, and Marcia B. Goldberg. Presence of Multiple Sites Containing Polar Material in Spherical Escherichia coli Cells That Lack MreB. *J. Bacteriol.*, 187(17):6187–6196, September 2005.

[90] Siyuan Wang, Hugo Arellano-Santoyo, Peter A. Combs, and Joshua W. Shaevitz. Actin-like cytoskeleton filaments contribute to cell mechanics in bacteria. *PNAS*, 107(20):9182–9185, May 2010.

[91] Kevin D. Young. The Selective Value of Bacterial Shape. *Microbiol. Mol. Biol. Rev.*, 70(3):660–703, September 2006.

[92] X. Yao, M. Jericho, D. Pink, and T. Beveridge. Thickness and Elasticity of Gram-Negative Murein Sacculi Measured by Atomic Force Microscopy. *J. Bacteriol.*, 181(22):6865–6875, November 1999.

[93] K. Bush. Antimicrobial agents targeting bacterial cell walls and cell membranes. *Rev. - Off. Int. Epizoot.*, 31(1):43–56, April 2012.

[94] H. Labischinski, E. W. Goodell, A. Goodell, and M. L. Hochberg. Direct proof of a "more-than-single-layered" peptidoglycan architecture of Escherichia coli W7: a neutron small-angle scattering study. *J. Bacteriol.*, 173(2):751–756, January 1991.

[95] Lu Gan, Songye Chen, and Grant J. Jensen. Molecular organization of Gram-negative peptidoglycan. *Proc Natl Acad Sci U S A*, 105(48):18953–18957, December 2008.

[96] J. V. Höltje. Growth of the stress-bearing and shape-maintaining murein sacculus of Escherichia coli. *Microbiol. Mol. Biol. Rev.*, 62(1):181–203, March 1998.

[97] Dirk-Jan Scheffers and Mariana G. Pinho. Bacterial cell wall synthesis: new insights from localization studies. *Microbiol. Mol. Biol. Rev.*, 69(4):585–607, December 2005.

[98] Athanasios Typas, Manuel Banzhaf, Carol A. Gross, and Waldemar Vollmer. From the regulation of peptidoglycan synthesis to bacterial growth and morphology. *Nat. Rev. Microbiol.*, 10(2):123–136, February 2012.

[99] E W Goodell. Recycling of murein by Escherichia coli. *J Bacteriol*, 163(1):305–310, July 1985.

[100] Matthew T. Swulius, Songye Chen, H. Jane Ding, Zhuo Li, Ariane Briegel, Martin Pilhofer, Elitza I. Tocheva, Suzanne R. Lybarger, Tanya L. Johnson, Maria Sandkvist, and Grant J. Jensen. Long helical filaments are not seen encircling cells in electron cryotomograms of rod-shaped bacteria. *Biochem. Biophys. Res. Commun.*, 407(4):650–655, April 2011.

[101] Matthew T. Swulius and Grant J. Jensen. The Helical MreB Cytoskeleton in Escherichia coli MC1000/pLE7 Is an Artifact of the N-Terminal Yellow Fluorescent Protein Tag. *J. Bacteriol.*, 194(23):6382–6386, December 2012.

[102] William Margolin. The price of tags in protein localization studies. *J. Bacteriol.*, 194(23):6369–6371, December 2012.

[103] Courtney L. White, Aleksandar Kitich, and James W. Gober. Positioning cell wall synthetic complexes by the bacterial morphogenetic proteins MreB and MreD. *Mol. Microbiol.*, 76(3):616–633, May 2010.

[104] Tamimount Mohammadi, Aneta Karczmarek, Muriel Crouvoisier, Ahmed Bouhss, Dominique Mengin-Lecreulx, and Tanneke Den Blaauwen. The essential peptidoglycan glycosyltransferase MurG forms a complex with proteins involved in lateral envelope growth as well as with proteins involved in cell division in Escherichia coli. *Molecular Microbiology*, 65(4):1106–1121, 2007.

[105] Julia Domínguez-Escobar, Arnaud Chastanet, Alvaro H. Crevenna, Vincent Fromion, Roland Wedlich-Söldner, and Rut Carballido-López. Processive movement of MreB-associated cell wall biosynthetic complexes in bacteria. *Science*, 333(6039):225–228, July 2011.

[106] Ethan C. Garner, Remi Bernard, Wenqin Wang, Xiaowei Zhuang, David Z. Rudner, and Tim Mitchison. Coupled, Circumferential Motions of the Cell Wall Synthesis Machinery and MreB Filaments in B. subtilis. *Science*, 333(6039):222–225, July 2011.

[107] Courtney L. White and James W. Gober. MreB: pilot or passenger of cell wall synthesis? *Trends in Microbiology*, 20(2):74–79, 2012.

[108] J. Löwe and L. A. Amos. Crystal structure of the bacterial cell-division protein FtsZ. *Nature*, 391(6663):203–206, January 1998.

[109] Harold P. Erickson, Dianne W. Taylor, Kenneth A. Taylor, and David Bramhill. Bacterial Cell Division Protein FtsZ Assembles into Protofilament Sheets and Minirings, Structural Homologs of Tubulin Polymers. *Proceedings of the National Academy of Sciences of the United States of America*, 93(1):519, 1996.

[110] David E. Anderson, Frederico J. Gueiros-Filho, and Harold P. Erickson. Assembly dynamics of FtsZ rings in Bacillus subtilis and Escherichia coli and effects of FtsZ-regulating proteins. *J. Bacteriol.*, 186(17):5775–5781, September 2004.

[111] Sebastien Pichoff and Joe Lutkenhaus. Tethering the Z ring to the membrane through a conserved membrane targeting sequence in FtsA. *Mol. Microbiol.*, 55(6):1722–1734, March 2005.

[112] Harold P Erickson. The FtsZ protofilament and attachment of ZipA—structural constraints on the FtsZ power stroke. *Current Opinion in Cell Biology*, 13(1):55–60, 2001.

[113] D. M. Raskin and P. A. de Boer. Rapid pole-to-pole oscillation of a protein required for directing division to the middle of Escherichia coli. *Proc. Natl. Acad. Sci. U.S.A.*, 96(9):4971–4976, April 1999.

[114] Jacob Halatek and Erwin Frey. Highly Canalized MinD Transfer and MinE Sequestration Explain the Origin of Robust MinCDE-Protein Dynamics. *Cell Reports*, 1(6):741–752, June 2012.

[115] Zhuo Li, Michael J. Trimble, Yves V. Brun, and Grant J. Jensen. The structure of FtsZ filaments in vivo suggests a force-generating role in cell division. *EMBO J.*, 26(22):4694–4708, November 2007.

[116] C. Lu, M. Reedy, and H. P. Erickson. Straight and curved conformations of FtsZ are regulated by GTP hydrolysis. *J. Bacteriol.*, 182(1):164–170, January 2000.

[117] Masaki Osawa, David E. Anderson, and Harold P. Erickson. Reconstitution of contractile FtsZ rings in liposomes. *Science*, 320(5877):792–794, May 2008.

[118] David W. Adams and Jeff Errington. Bacterial cell division: assembly, maintenance and disassembly of the Z ring. *Nat. Rev. Microbiol.*, 7(9):642–653, September 2009.

[119] Michelle Aaron, Godefroid Charbon, Hubert Lam, Heinz Schwarz, Waldemar Vollmer, and Christine Jacobs-Wagner. The tubulin homologue FtsZ contributes to cell elongation by guiding cell wall precursor synthesis in Caulobacter crescentus. *Mol. Microbiol.*, 64(4):938–952, May 2007.

[120] Henrik Hasman, Mark A. Schembri, and Per Klemm. Antigen 43 and type 1 fimbriae determine colony morphology of Escherichia coli K-12. *Journal of bacteriology*, 182(4):1089–1095, 2000.

[121] L A Pratt and R Kolter. Genetic analysis of Escherichia coli biofilm formation: roles of flagella, motility, chemotaxis and type I pili. *Molecular Microbiology*, 30(2):285–293, October 1998.

[122] I. Vallet, J. W. Olson, S. Lory, A. Lazdunski, and A. Filloux. The chaperone/usher pathways of Pseudomonas aeruginosa: identification of fimbrial gene clusters (cup) and their involvement in biofilm formation. *Proc. Natl. Acad. Sci. U.S.A.*, 98(12):6911–6916, June 2001.

[123] Christophe Beloin, Ali Houry, Manuel Froment, Jean-Marc Ghigo, and Nelly Henry. A short-time scale colloidal system reveals early bacterial adhesion dynamics. *PLoS Biol.*, 6(7):e167, July 2008.

[124] F. Paola Corona-Izquierdo and Jorge Membrillo-Hernández. Biofilm formation in Escherichia coli is affected by 3-(N-morpholino)propane sulfonate (MOPS). *Research in Microbiology*, 153(3):181–185, 2002.

[125] O. Vidal, R. Longin, C. Prigent-Combaret, C. Dorel, M. Hooreman, and P. Lejeune. Isolation of an Escherichia coli K-12 mutant strain

able to form biofilms on inert surfaces: involvement of a new ompR allele that increases curli expression. *J. Bacteriol.*, 180(9):2442–2449, May 1998.

[126] D. Cunliffe, C. A. Smart, C. Alexander, and E. N. Vulfson. Bacterial adhesion at synthetic surfaces. *Applied and environmental microbiology*, 65(11):4995–5002, 1999.

[127] P. Rutter and R. Leech. The deposition of Streptococcus sanguis NCTC 7868 from a flowing suspension. *J. Gen. Microbiol.*, 120(2):301–307, October 1980.

[128] D. R. Absolom, F. V. Lamberti, Z. Policova, W. Zingg, C. J. van Oss, and A. W. Neumann. Surface thermodynamics of bacterial adhesion. *Appl. Environ. Microbiol.*, 46(1):90–97, July 1983.

[129] M. C. van Loosdrecht, J. Lyklema, W. Norde, G. Schraa, and A. J. Zehnder. The role of bacterial cell wall hydrophobicity in adhesion. *Appl. Environ. Microbiol.*, 53(8):1893–1897, August 1987.

[130] A. Razatos, Y. L. Ong, M. M. Sharma, and G. Georgiou. Molecular determinants of bacterial adhesion monitored by atomic force microscopy. *Proc. Natl. Acad. Sci. U.S.A.*, 95(19):11059–11064, September 1998.

[131] K. Agladze, X. Wang, and T. Romeo. Spatial Periodicity of Escherichia coli K-12 Biofilm Microstructure Initiates during a Reversible, Polar Attachment Phase of Development and Requires the Polysaccharide Adhesin PGA. *Journal of Bacteriology*, 187(24):8237–8246, December 2005.

[132] L. M. Nilsson, W. E. Thomas, E. Trintchina, V. Vogel, and E. V. Sokurenko. Catch Bond-mediated Adhesion without a Shear Threshold: trimannose versus monomannose interactions with the FimH adhesin of Escherichia coli. *Journal of Biological Chemistry*, 281(24):16656–16663, June 2006.

[133] Sigolene Lecuyer, Roberto Rusconi, Yi Shen, Alison Forsyth, Hera Vlamakis, Roberto Kolter, and Howard A. Stone. Shear Stress Increases the Residence Time of Adhesion of Pseudomonas aeruginosa. *Biophysical Journal*, 100(2):341–350, January 2011.

[134] Wendy E. Thomas, Lina M. Nilsson, Manu Forero, Evgeni V. Sokurenko, and Viola Vogel. Shear-dependent 'stick-and-roll' adhesion of type 1 fimbriated Escherichia coli. *Mol. Microbiol.*, 53(5):1545–1557, September 2004.

[135] L. De La Fuente, E. Montanes, Y. Meng, Y. Li, T. J. Burr, H. C. Hoch, and M. Wu. Assessing Adhesion Forces of Type I and Type IV Pili of

Xylella fastidiosa Bacteria by Use of a Microfluidic Flow Chamber. *Applied and Environmental Microbiology*, 73(8):2690–2696, April 2007.

[136] Alexandre Persat, Carey D. Nadell, Minyoung Kevin Kim, Francois Ingremeau, Albert Siryaporn, Knut Drescher, Ned S. Wingreen, Bonnie L. Bassler, Zemer Gitai, and Howard A. Stone. The Mechanical World of Bacteria. *Cell*, 161(5):988–997, 2015.

[137] Ina H. Pratt-Terpstra, Anton H. Weerkamp, and Henk J. Busscher. Adhesion of oral streptococci from a flowing suspension to uncoated and albumin-coated surfaces. *Journal of general microbiology*, 133(11):3199–3206, 1987.

[138] Annie Sénéchal, Shawn D. Carrigan, and Maryam Tabrizian. Probing surface adhesion forces of Enterococcus faecalis to medical-grade polymers using atomic force microscopy. *Langmuir*, 20(10):4172–4177, May 2004.

[139] Wen Zhang, Andrew G. Stack, and Yongsheng Chen. Interaction force measurement between E. coli cells and nanoparticles immobilized surfaces by using AFM. *Colloids and Surfaces B: Biointerfaces*, 82(2):316–324, 2011.

[140] He Xu, Anne E. Murdaugh, Wei Chen, Katherine E. Aidala, Megan A. Ferguson, Eileen M. Spain, and Megan E. Núñez. Characterizing pilus-mediated adhesion of biofilm-forming E. coli to chemically diverse surfaces using atomic force microscopy. *Langmuir*, 29(9):3000–3011, March 2013.

[141] Tong Zhang, Yuanqing Chao, Kaimin Shih, Xiao-Yan Li, and Herbert H. P. Fang. Quantification of the lateral detachment force for bacterial cells using atomic force microscope and centrifugation. *Ultramicroscopy*, 111(2):131–139, January 2011.

[142] Susan M. Deupree and Mark H. Schoenfisch. Quantitative method for determining the lateral strength of bacterial adhesion and application for characterizing adhesion kinetics. *Langmuir*, 24(9):4700–4707, May 2008.

[143] Manu Forero, Olga Yakovenko, Evgeni V Sokurenko, Wendy E Thomas, and Viola Vogel. Uncoiling Mechanics of Escherichia coli Type I Fimbriae Are Optimized for Catch Bonds. *PLoS Biol*, 4(9):e298, 2006.

[144] Erik Fällman, Staffan Schedin, Jana Jass, Magnus Andersson, Bernt Eric Uhlin, and Ove Axner. Optical tweezers based force measurement system for quantitating binding interactions: system design and application for the study of bacterial adhesion. *Biosensors and Bioelectronics*, 19(11):1429–1437, 2004.

[145] Vincent Dupres, Franco D. Menozzi, Camille Locht, Brian H. Clare, Nicholas L. Abbott, Stéphane Cuenot, Coralie Bompard, Dominique Raze, and Yves F. Dufrêne. Nanoscale mapping and functional analysis of individual adhesins on living bacteria. *Nat. Methods*, 2(7):515–520, July 2005.

[146] Michael N. Liang, Stephen P. Smith, Steven J. Metallo, Insung S. Choi, Mara Prentiss, and George M. Whitesides. Measuring the forces involved in polyvalent adhesion of uropathogenic Escherichia coli to mannose-presenting surfaces. *Proceedings of the National Academy of Sciences*, 97(24):13092–13096, 2000.

[147] Kathryn H. Simpson, Gabriela Bowden, Magnus Höök, and Bahman Anvari. Measurement of Adhesive Forces between Individual Staphylococcus aureus MSCRAMMs and Protein-Coated Surfaces by Use of Optical Tweezers. *J Bacteriol*, 185(6):2031–2035, March 2003.

[148] N. P. Boks, W. Norde, H. C. van der Mei, and H. J. Busscher. Forces involved in bacterial adhesion to hydrophilic and hydrophobic surfaces. *Microbiology*, 154(10):3122–3133, October 2008.

[149] Isolde Le Trong, Pavel Aprikian, Brian A. Kidd, Manu Forero-Shelton, Veronika Tchesnokova, Ponni Rajagopal, Victoria Rodriguez, Gianluca Interlandi, Rachel Klevit, Viola Vogel, Ronald E. Stenkamp, Evgeni V. Sokurenko, and Wendy E. Thomas. Structural Basis for Mechanical Force Regulation of the Adhesin FimH via Finger Trap-like Sheet Twisting. *Cell*, 141(4):645–655, May 2010.

[150] D. I. Kisiela, J. J. Kramer, V. Tchesnokova, P. Aprikian, V. Yarov-Yarovoy, S. Clegg, and E. V. Sokurenko. Allosteric Catch Bond Properties of the FimH Adhesin from Salmonella enterica Serovar Typhimurium. *Journal of Biological Chemistry*, 286(44):38136–38147, November 2011.

[151] Fangchao Song and Dacheng Ren. Stiffness of Cross-Linked Poly(Dimethylsiloxane) Affects Bacterial Adhesion and Antibiotic Susceptibility of Attached Cells. *Langmuir*, 30(34):10354–10362, September 2014.

[152] Jenny A. Lichter, M. Todd Thompson, Maricela Delgadillo, Takehiro Nishikawa, Michael F. Rubner, and Krystyn J. Van Vliet. Substrata Mechanical Stiffness Can Regulate Adhesion of Viable Bacteria. *Biomacromolecules*, 9(6):1571–1578, 2008.

[153] Charalampia-Georgia Korea, Jean-Marc Ghigo, and Christophe Beloin. The sweet connection: Solving the riddle of multiple sugar-binding fimbrial adhesins in Escherichia coli: Multiple E. coli fimbriae form a

versatile arsenal of sugar-binding lectins potentially involved in surface-colonisation and tissue tropism. *Bioessays*, 33(4):300–311, April 2011.

[154] Paolo Natale, Thomas Brüser, and Arnold J. M. Driessen. Sec- and Tat-mediated protein secretion across the bacterial cytoplasmic membrane—Distinct translocases and mechanisms. *Biochimica et Biophysica Acta (BBA) - Biomembranes*, 1778(9):1735–1756, September 2008.

[155] Michael Vetsch, Chasper Puorger, Thomas Spirig, Ulla Grauschopf, Eilika U. Weber-Ban, and Rudi Glockshuber. Pilus chaperones represent a new type of protein-folding catalyst. *Nature*, 431(7006):329–333, September 2004.

[156] Sebastian Geibel, Erik Procko, Scott J. Hultgren, David Baker, and Gabriel Waksman. Structural and energetic basis of folded-protein transport by the FimD usher. *Nature*, 496(7444):243–246, April 2013.

[157] Gabriel Waksman and Scott J. Hultgren. Structural biology of the chaperone–usher pathway of pilus biogenesis. *Nature Reviews Microbiology*, 7, 2009.

[158] Andreas Busch and Gabriel Waksman. Chaperone–usher pathways: diversity and pilus assembly mechanism. *Philosophical Transactions of the Royal Society of London B: Biological Sciences*, 367(1592):1112–1122, April 2012.

[159] Sebastian Geibel and Gabriel Waksman. The molecular dissection of the chaperone–usher pathway. *Biochimica et Biophysica Acta (BBA) - Molecular Cell Research*, 1843(8):1559–1567, 2014.

[160] Tiago R. D. Costa, Catarina Felisberto-Rodrigues, Amit Meir, Marie S. Prevost, Adam Redzej, Martina Trokter, and Gabriel Waksman. Secretion systems in Gram-negative bacteria: structural and mechanistic insights. *Nat. Rev. Microbiol.*, 13(6):343–359, May 2015.

[161] Barry I. Eisenstein. Phase Variation of Type 1 Fimbriae in Escherichia coli is under Transcriptional Control. *Science*, 214(4518):337, 1981.

[162] Erik Hahn, Peter Wild, Uta Hermanns, Peter Sebbel, Rudi Glockshuber, Marcus Häner, Nicole Taschner, Peter Burkhard, Ueli Aebi, and Shirley A. Müller. Exploring the 3d Molecular Architecture of Escherichia coli Type 1 Pili. *Journal of Molecular Biology*, 323(5):845–857, November 2002.

[163] Andreas Reisner, Mario Maierl, Michael Jörger, Robert Krause, Daniela Berger, Andrea Haid, Dijana Tesic, and Ellen L. Zechner.

Type 1 fimbriae contribute to catheter-associated urinary tract infections caused by Escherichia coli. *J. Bacteriol.*, 196(5):931–939, March 2014.

[164] K A Krogfelt, H Bergmans, and P Klemm. Direct evidence that the FimH protein is the mannose-specific adhesin of Escherichia coli type 1 fimbriae. *Infect Immun*, 58(6):1995–1998, June 1990.

[165] Wendy E. Thomas, Elena Trintchina, Manu Forero, Viola Vogel, and Evgeni V. Sokurenko. Bacterial Adhesion to Target Cells Enhanced by Shear Force. *Cell*, 109(7):913–923, 2002.

[166] Wendy Thomas, Manu Forero, Olga Yakovenko, Lina Nilsson, Paolo Vicini, Evgeni Sokurenko, and Viola Vogel. Catch-Bond Model Derived from Allostery Explains Force-Activated Bacterial Adhesion. *Biophysical Journal*, 90(3):753–764, 2006.

[167] Sean-Paul Nuccio and Andreas J. Bäumler. Evolution of the Chaperone/Usher Assembly Pathway: Fimbrial Classification Goes Greek. *Microbiol. Mol. Biol. Rev.*, 71(4):551–575, December 2007.

[168] Caroline Giraud, Christophe Bernard, Ségolène Ruer, and Sophie De Bentzmann. Biological 'glue' and 'Velcro': molecular tools for adhesion and biofilm formation in the hairy and gluey bug Pseudomonas aeruginosa. *Environmental Microbiology Reports*, 2(3):343–358, 2010.

[169] Ian R Henderson, Fernando Navarro-Garcia, and James P Nataro. The great escape: structure and function of the autotransporter proteins. *Trends in Microbiology*, 6(9):370–378, September 1998.

[170] David C. Oliver, George Huang, and Rachel C. Fernandez. Identification of Secretion Determinants of the Bordetella pertussis BrkA Autotransporter. *J. Bacteriol.*, 185(2):489–495, January 2003.

[171] Mickaël Desvaux, Nicholas J. Parham, and Ian R. Henderson. The autotransporter secretion system. *Research in Microbiology*, 155(2):53–60, March 2004.

[172] Ian R. Henderson, Fernando Navarro-Garcia, Mickaël Desvaux, Rachel C. Fernandez, and Dlawer Ala'Aldeen. Type V Protein Secretion Pathway: the Autotransporter Story. *Microbiol. Mol. Biol. Rev.*, 68(4):692–744, December 2004.

[173] I. R. Henderson, M. Meehan, and P. Owen. Antigen 43, a phase-variable bipartite outer membrane protein, determines colony morphology and autoaggregation in Escherichia coli K-12. *FEMS Microbiol. Lett.*, 149(1):115–120, April 1997.

[174] Glen C. Ulett, Richard I. Webb, and Mark A. Schembri. Antigen-43-mediated autoaggregation impairs motility in Escherichia coli. *Microbiology (Reading, Engl.)*, 152(Pt 7):2101–2110, July 2006.

[175] Peter Owen, Mary Meehan, Helen de Loughry-Doherty, and Ian Henderson. Phase-variable outer membrane proteins in Escherichia coli. *FEMS Immunology & Medical Microbiology*, 16(2):63–76, December 1996.

[176] Ashwini Chauhan, Chizuko Sakamoto, Jean-Marc Ghigo, and Christophe Beloin. Did I Pick the Right Colony? Pitfalls in the Study of Regulation of the Phase Variable Antigen 43 Adhesin. *PLoS ONE*, 8(9), September 2013.

[177] Agnès Roux, Christophe Beloin, and Jean-Marc Ghigo. Combined Inactivation and Expression Strategy To Study Gene Function under Physiological Conditions: Application to Identification of New Escherichia coli Adhesins. *J. Bacteriol.*, 187(3):1001–1013, February 2005.

[178] Yvonne Gar-Yun Chan, Sean Phillip Riley, and Juan Jose Martinez. Adherence to and invasion of host cells by spotted fever group Rickettsia species. *Rickettsia*, 1:139, 2010.

[179] Margery L. Evans and Matthew R. Chapman. Curli biogenesis: Order out of disorder. *Biochimica et Biophysica Acta (BBA) - Molecular Cell Research*, 1843(8):1551–1558, 2014.

[180] Lewis D. B. Evans, Colin Hughes, and Gillian M. Fraser. Building a flagellum outside the bacterial cell. *Trends in Microbiology*, 22(10):566–572, October 2014.

[181] Linda Turner, William S. Ryu, and Howard C. Berg. Real-Time Imaging of Fluorescent Flagellar Filaments. *J. Bacteriol.*, 182(10):2793–2801, May 2000.

[182] Ashley A. Nenninger, Lloyd S. Robinson, Neal D. Hammer, Elisabeth Ashman Epstein, Matthew P. Badtke, Scott J. Hultgren, and Matthew R. Chapman. CsgE is a curli secretion specificity factor that prevents amyloid fibre aggregation. *Mol. Microbiol.*, 81(2):486–499, July 2011.

[183] Neal D. Hammer, Jens C. Schmidt, and Matthew R. Chapman. The curli nucleator protein, CsgB, contains an amyloidogenic domain that directs CsgA polymerization. *Proc. Natl. Acad. Sci. U.S.A.*, 104(30):12494–12499, July 2007.

[184] A. Olsén, A. Jonsson, and S. Normark. Fibronectin binding mediated by a novel class of surface organelles on Escherichia coli. *Nature*, 338(6217):652–655, April 1989.

[185] A. Olsén, A. Arnqvist, M. Hammar, and S. Normark. Environmental regulation of curli production in Escherichia coli. *Infect Agents Dis*, 2(4):272–274, August 1993.

[186] U. Römling, Z. Bian, M. Hammar, W. D. Sierralta, and S. Normark. Curli fibers are highly conserved between Salmonella typhimurium and Escherichia coli with respect to operon structure and regulation. *J. Bacteriol.*, 180(3):722–731, February 1998.

[187] C. Prigent-Combaret, G. Prensier, T. T. Le Thi, O. Vidal, P. Lejeune, and C. Dorel. Developmental pathway for biofilm formation in curli-producing Escherichia coli strains: role of flagella, curli and colanic acid. *Environ. Microbiol.*, 2(4):450–464, August 2000.

[188] Eva Brombacher, Corinne Dorel, Alexander J. B. Zehnder, and Paolo Landini. The curli biosynthesis regulator CsgD co-ordinates the expression of both positive and negative determinants for biofilm formation in Escherichia coli. *Microbiology (Reading, Engl.)*, 149(Pt 10):2847–2857, October 2003.

[189] Fadel A. Samatey, Hideyuki Matsunami, Katsumi Imada, Shigehiro Nagashima, Tanvir R. Shaikh, Dennis R. Thomas, James Z. Chen, David J. Derosier, Akio Kitao, and Keiichi Namba. Structure of the bacterial flagellar hook and implication for the molecular universal joint mechanism. *Nature*, 431(7012):1062–1068, October 2004.

[190] Fabienne F. V. Chevance and Kelly T. Hughes. Coordinating assembly of a bacterial macromolecular machine. *Nature Reviews Microbiology*, 6, 2008.

[191] Robert Belas. Biofilms, flagella, and mechanosensing of surfaces by bacteria. *Trends in Microbiology*, 22(9):517–527, September 2014.

[192] Liyan Ping, Beth Weiner, and Nancy Kleckner. Tsr-GFP accumulates linearly with time at cell poles, and can be used to differentiate 'old' versus 'new' poles, in Escherichia coli. *Mol. Microbiol.*, 69(6):1427–1438, September 2008.

[193] Liyan Ping. The Asymmetric Flagellar Distribution and Motility of Escherichia coli. *Journal of Molecular Biology*, 397(4):906–916, 2010.

[194] Sarah B. Guttenplan and Daniel B. Kearns. Regulation of flagellar motility during biofilm formation. *FEMS Microbiology Reviews*, 37(6):849–871, November 2013.

[195] Pushkar P. Lele, Basarab G. Hosu, and Howard C. Berg. Dynamics of mechanosensing in the bacterial flagellar motor. *PNAS*, 110(29):11839–11844, July 2013.

[196] John S. Mattick. Type IV pili and twitching motility. *Annu. Rev. Microbiol.*, 56:289–314, 2002.

[197] Nicolas Biais, Benoît Ladoux, Dustin Higashi, Magdalene So, and Michael Sheetz. Cooperative Retraction of Bundled Type IV Pili Enables Nanonewton Force Generation. *PLoS Biology*, 6(4):e87, 2008.

[198] Nathalie Sauvonnet, Pierre Gounon, and Anthony P. Pugsley. PpdD Type IV Pilin of Escherichia coliK-12 Can Be Assembled into Pili in Pseudomonas aeruginosa. *J. Bacteriol.*, 182(3):848–854, February 2000.

[199] James A. Shapiro and C. Hsu. Escherichia coli K-12 cell-cell interactions seen by time-lapse video. *Journal of bacteriology*, 171(11):5963, 1989.

[200] Maria Dienerowitz, Laura V. Cowan, Graham M. Gibson, Rebecca Hay, Miles J. Padgett, and Vernon R. Phoenix. Optically Trapped Bacteria Pairs Reveal Discrete Motile Response to Control Aggregation upon Cell–Cell Approach. *Current Microbiology*, 69(5):669–674, November 2014.

[201] HoJung Cho, Henrik Jönsson, Kyle Campbell, Pontus Melke, Joshua W. Williams, Bruno Jedynak, Ann M. Stevens, Alex Groisman, and Andre Levchenko. Self-Organization in High-Density Bacterial Colonies: Efficient Crowd Control. *PLoS Biology*, 5(11):e302, 2007.

[202] Dmitri Volfson, Scott Cookson, Jeff Hasty, and Lev S. Tsimring. Biomechanical ordering of dense cell populations. *Proceedings of the National Academy of Sciences*, 105(40):15346–15351, 2008.

[203] Denis Boyer, William Mather, Octavio Mondragón-Palomino, Sirio Orozco-Fuentes, Tal Danino, Jeff Hasty, and Lev S Tsimring. Buckling instability in ordered bacterial colonies. *Physical Biology*, 8(2):026008, April 2011.

[204] Matthew A. A. Grant, Bartłomiej Wacław, Rosalind J. Allen, and Pietro Cicuta. The role of mechanical forces in the planar-to-bulk transition in growing Escherichia coli microcolonies. *J. R. Soc. Interface*, 11(97):20140400, August 2014.

[205] Munehiro Asally, Mark Kittisopikul, Pau Rué, Yingjie Du, Zhenxing Hu, Tolga Çağatay, Andra B. Robinson, Hongbing Lu, Jordi Garcia-Ojalvo, and Gürol M. Süel. Localized cell death focuses mechanical forces during 3d patterning in a biofilm. *PNAS*, 109(46):18891–18896, November 2012.

[206] Olivier Galy, Patricia Latour-Lambert, Kais Zrelli, Jean-Marc Ghigo, Christophe Beloin, and Nelly Henry. Mapping of bacterial biofilm local mechanics by magnetic microparticle actuation. *Biophys. J.*, 103(6):1400–1408, September 2012.

[207] Thomas Julou, Thierry Mora, Laurent Guillon, Vincent Croquette, Isabelle J. Schalk, David Bensimon, and Nicolas Desprat. Cell–cell contacts confine public goods diffusion inside Pseudomonas aeruginosa clonal microcolonies. *PNAS*, 110(31):12577–12582, July 2013.

[208] Nobuyuki Otsu. A Threshold Selection Method from Gray-Level Histograms. *IEEE Transactions on Systems, Man and Cybernetics*, 9(1):62–66, January 1979.

[209] Daniel J. Kiviet, Philippe Nghe, Noreen Walker, Sarah Boulineau, Vanda Sunderlikova, and Sander J. Tans. Stochasticity of metabolism and growth at the single-cell level. *Nature*, 514(7522):376–379, October 2014.

[210] Jonathan W. Young, James C. W. Locke, Alphan Altinok, Nitzan Rosenfeld, Tigran Bacarian, Peter S. Swain, Eric Mjolsness, and Michael B. Elowitz. Measuring single-cell gene expression dynamics in bacteria using fluorescence time-lapse microscopy. *Nat. Protocols*, 7(1):80–88, January 2012.

[211] Eric J Stewart, Richard Madden, Gregory Paul, and François Taddei. Aging and Death in an Organism That Reproduces by Morphologically Symmetric Division. *PLoS Biol*, 3(2), 2005.

[212] M Dembo and Y L Wang. Stresses at the cell-to-substrate interface during locomotion of fibroblasts. *Biophys J*, 76(4):2307–2316, April 1999.

[213] S Munevar, Y Wang, and M Dembo. Traction force microscopy of migrating normal and H-ras transformed 3t3 fibroblasts. *Biophys J*, 80(4):1744–1757, April 2001.

[214] Justin R. Tse and Adam J. Engler. Preparation of hydrogel substrates with tunable mechanical properties. *Curr Protoc Cell Biol*, Chapter 10:Unit 10.16, June 2010.

[215] Mark Ahearne, Ying Yang, Alicia J El Haj, Kong Y Then, and Kuo-Kang Liu. Characterizing the viscoelastic properties of thin hydrogel-based constructs for tissue engineering applications. *J R Soc Interface*, 2(5):455–463, December 2005.

[216] Mark Ahearne, Eleftherios Siamantouras, Ying Yang, and Kuo-Kang Liu. Mechanical characterization of biomimetic membranes by micro-shaft poking. *J R Soc Interface*, 6(34):471–478, May 2009.

[217] James P. Butler, Iva Marija Tolić-Nørrelykke, Ben Fabry, and Jeffrey J. Fredberg. Traction fields, moments, and strain energy that cells exert on their surroundings. *Am. J. Physiol., Cell Physiol.*, 282(3):C595–605, March 2002.

[218] I. Sonntag, H. Schwarz, Y. Hirota, and U. Henning. Cell envelope and shape of Escherichia coli: multiple mutants missing the outer membrane lipoprotein and other major outer membrane proteins. *J. Bacteriol.*, 136(1):280–285, October 1978.

[219] Pin-Tzu Su, Pei-Wen Yen, Shao-Hung Wang, Chi-Hung Lin, Arthur Chiou, and Wan-Jr Syu. Factors Affecting Daughter Cells' Arrangement during the Early Bacterial Divisions. *PLoS ONE*, 5(2), February 2010.

[220] Sahand Hormoz, Nicolas Desprat, and Boris I. Shraiman. Inferring epigenetic dynamics from kin correlations. *Proceedings of the National Academy of Sciences*, 112(18), May 2015.

[221] A. S. G. Curtis. The mechanism of adhesion of cells to glass. *J Cell Biol*, 20(2):199–215, February 1964.